Technische Universität München

Fakultät für Physik

Lehrstuhl für Experimentalphysik, Oberflächen - und Grenzflächenphysik(E20)

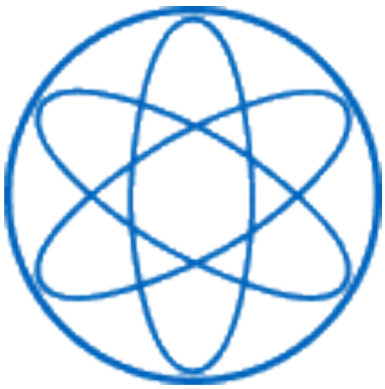

Single layer films of functional molecules on noble metal surfaces visited by scanning tunneling microscopy and X-ray spectroscopy

Dissertation

Seung Cheol Oh

TECHNISCHE UNIVERSITÄT MÜNCHEN

Fakultät für Physik

Lehrstuhl für Experimentalphysik, Oberflächen - und Grenzflächenphysik(E20)

Single layer films of functional molecules on noble metal surfaces visited by scanning tunneling microscopy and X-ray spectroscopy

Seung Cheol Oh

Vollstädiger Abdruck der von der Fakultät für Physik der Technischen Universität München zur Erlangung des akademischen Grades eines Doktors der Naturwissenschaften (Dr. rer. nat.) genehmigten Dissertation.

Vorsitzender:	Univ.-Prof. Dr. Ulrich Gerland
Prüfer der Dissertation:	1. Univ.-Prof. Dr. Johannes Barth
	2. Priv.-Doz. Dr. Markus Lackinger, Ludwig-Maximilians-Universität München

Die Promotion wurde am 23.07.2014 bei der Technischen Universität München eingereicht und durch die Fakultät für Physik am 23.10.2014 angenommen.

Abstract

Molecules with functional groups play an important role in applications of nanoscience, in technology for human life as well as in nanodevices, biomaterials, and synthesis of new medical compounds. The functional groups can react either with other molecules and or a substrate for the bottom up fabrication of new nanoarchitectures. In this thesis, three different self-assembled systems, (diethylstilbestrol (DES), 2H-tetraphenylporphyrin (2H-TPP), tetraketone (**PT**) and tetramine (**PPD**)) were investigated as a function of temperature and surface coverage on close-packed, single crystal metal surfaces. The investigations were performed under ultra-high vacuum conditions by means of variable-temperature scanning tunneling microscopy, X-ray photoelectron spectroscopy and near edge X-ray absorption fine structure spectroscopy. The DES molecules show diverse molecular motives expressing organisational chirality influenced by their interactions and deprotonation of the functional group. 2H-TPP molecules subject to annealing undergo chemical transformations into four distinct cyclodehydrogenation products before polymerising with the formation of new intermolecular C-C bonds. This molecule could be efficiently metalated by Ru from a metal precursor on the silver substrate. Exploring new pathways for stable nanoarchitectures, we used two molecules which have functional groups of ketones and amines. The two molecules can form covalent bonds by dehydration after heat treatment on a metal surface.

Contents

1 Introduction **1**

2 Experimental Methods: Theory and Setup **5**

2.1 Scanning tunneling microscopy 6

2.1.1 Tunneling Effect 6

2.1.2 Operation principle 9

2.1.3 Experimental set up 10

2.1.4 Sample preparation 13

2.2 X-ray spectroscopy 15

2.2.1 X-ray phtoelectron spectroscopy 16

2.2.2 Near edge X-ray absorption fine structure spectroscopy 17

2.2.3 Experimental set up 17

3 Results **21**

3.1 Steering the conformation of diethylstilbestrol by the metal surface 22

3.1.1 DES on Ag(111) 24

3.1.2 DES on Cu(111) 31

3.1.3 Conclusion 37

3.2 *meso*-tetraphenylporphyrin on Ag(111) 38

3.2.1 Flat conformation 41

3.2.2 Ru metalated 2H-TPP 45

3.2.3 Homo coupling of 2H-TPP 48

3.2.4 Conclusion 50

3.3 Towards covalently bonded molecular networks by an amine - ketone reaction on Ag(111) 51

3.3.1 PT on Ag(111) 54

3.3.2 PPD on Ag(111) 57

3.3.3 Intermixed layers on Ag(111) 60

3.3.4 Conclusion 63

4 Summary and Conclusions **65**

5 Acknowledgments **69**

6 List of Publications **71**

Bibliography **72**

List of Figures

1.1 DNA biological applications in nanotechnology. 2
1.2 Low dimensional nanostructures formed by covalent bonding. 2
1.3 Chemical structures of molecules. 3

2.1 Wave function of quantum tunneling through a barrier 7
2.2 One-dimensional sample-vacuum-tip tunneling junction 8
2.3 STM operation modes: constant height mode and constant current mode. 10
2.4 Set up of the UHV chambers 11
2.5 Cross-section of the Aarhus STM 12
2.6 Schematic of $Ru_3(CO)_{12}$ dosing set up 13
2.7 Synchrotron radiation system consisting of a microtron injector 15
2.8 Schematic XPS process, showing photo electron emission of an 1s electron. . . . 16
2.9 Principle of NEXAFS spectroscopy: potential and K-shell spectrum of a diatomic molecular (sub)group 18
2.10 Schematic of X-ray absorption of an benzene ring. 19
2.11 The end-station of the HE-SGM beamline at BESSY II 19

3.1 Estrogen receptor structure and ligand sets with DES ligand-binding domain . . . 22
3.2 Diethylstilbestrol (DES): chemical structure in *cis*- and *trans*-isomer conformation 23
3.3 XP-spectra of O 1s and C 1s core level energies of DES adsorbed on the Ag(111) surface. 24
3.4 NEXAFS spectra of DES normalized C K-edge spectra after annealing the sample to 290 K, 310 K and 370 K. 26
3.5 Ball and stick model of DES on the Ag(111) surface with side views of the molecule 27
3.6 STM results of the molecules superimposed with molecular models. 27
3.7 Shingle structure of DES on Ag(111) at room temperature. 28
3.8 Molecular assembly on the surface with few molecules remaining. 29
3.9 The O 1s and C 1s XP spectra of DES on Cu(111) 31
3.10 Stripe motif on Cu(111) recorded at 170 K after annealing to 350 K. 33
3.11 STM images of stars motif with a step edge. 34
3.12 STM images of star pattern and the changed star pattern 35

3.13 Chainlike motif after annealing to 450 K 36
3.14 Molecular model of DES in *cis-trans* isomerization on the Cu(111) surface. . . . 36
3.15 Chemical structure of porphine and porphyrin derivatives with STM images. . . . 39
3.16 Molecular models: metal precursor $Ru_3(CO)_{12}$ and the 2H-tetraphenylporphyrin (2H-TPP) 40
3.17 Non-flat and flat 2H-TPP conformation on Ag(111). 41
3.18 Two rows assembly and diffusing single molecules in the between network. . . . 42
3.19 NEXAFS results of cyclodehydrogenated 2H-TTP 43
3.20 Metalation of flattened 2H-TPP 45
3.21 Cyclodehydrogenation of 2H-TPP molecules leads to different molecular conformations 46
3.22 XPS results: N1s, Ru $3d_{5/3}$, and O1s spectra 46
3.23 Reaction scheme of homo-coupling of 2H-TPP moieties. 48
3.24 Homo coupling of flat 2H-TPP molecules. 49
3.25 Oligomer and polymer homo-coupling products. 50
3.26 Reaction mechanism of a ketone with a primary amine 52
3.27 Chemical structure of triphenylene hexamine (TPHA) and butylpyrene tetraone (PT). 52
3.28 Molecular models of **PT** and **PPD** 54
3.29 **PT** on Ag(111) 54
3.30 Expanding low dimensional nanostructure of **PT** on Ag(111). 55
3.31 Aggregated and disordered patches of molecules. 56
3.32 **PPD** on Ag(111). 57
3.33 Predominant motifs of **PPD** on Ag(111). 58
3.34 Highly regular structures after annealing to 537 K. 59
3.35 Mixture of **PPD** and **PT** molecules on Ag(111). 60
3.36 Coadsorption of **PT** and **PPD** on Ag(111) 61
3.37 Small islands of **PPD** and linear structures close to a step edge 61
3.38 Dehydration of molecules after annealing to 523 K. 62

4.1 Graphical summary of the self-assembled structures formed by DES molecules on Ag(111) and on Cu(111). 66
4.2 Graphical summary of the chemical transformations of the 2H-TPP molecules on Ag(111) as a function of temperature. 66
4.3 Summary of the tetraketone **PT** and the tetramine **PPD** molecules on Ag(111) . . 67

List of Tables

2.1.1 Sample preparation: molecules, crucibles temperature for dosing at OMBE, sample temperature at dosing, temperature of the measured surface on the STM stage. 14

3.1.1 XPS results after annealing at 300 K, 330 K and 350 K. 25
3.1.2 XPS results: Binding energy and FWHM 32
3.2.1 Peak assignment for the C K-Edge NEXAFS peaks of the cyclodehydrogenated porphyrin 44

1 Introduction

In the recent years, we can see the word 'nano' with increasing frequency in our environment and advertisements such as, nano robot, nano coating, nano medicine, nano printing, washing detergents including silver nano particles and so on. These applications are called nanotechnology, a concept that was introduced in the lecture "There's Plenty of Room at the Bottom" in 1959 by Richard Feynman [1]. Nanotechnology experienced in a rapid development over the last two decades. Nanotechnology is closely associated with life and natural science and plays an important role in biology, chemistry, and physical science in our era. There are two major techniques to produce nano architectures and miniaturization of components. One is the top down approach which is normally using lithographic techniques to build a miniature structure by decreasing the size of the material. But this technique reaches certain physical limitations in size of $\sim$ 10 - 20 nm and is difficult to advance [2]. The other one is the bottom up approach which is based on the assembly of building blocks such as atoms and molecules to fabricate larger structures. Notably molecular building-blocks can self assemble to a nanostructure according to the functionalities provided by the constituents [2].

In the field of biology, nanotechnology provides solutions to biological problems and applications in nanodevices fabrication (see Figure 1.1) [3]. Biomolecules can be used for diagnosis and monitoring of factors such as alterations in DNA sequence and other environmentally caused alterations in human cells [4–7].

Bottom up nanoarchitectures at surfaces technique a balance of by molecule-molecule and molecule-substrate interactions. The molecules employed include not only small biomolecules but also supra(macro)molecules with specific functionalities. Supramolecular chemistry exploits non-covalent interactions such as hydrogen bonding, coulombic interactions and metal-ligand bonds to form large molecular assemblies and was founded by Jean-Marie Jehn [8]. Supramolecular chemistry has a variety of applications and plays a crucial role in nano science. Especially for thermally to bust surface nano architectures, one often uses metal ligand interactions. For even more stable nanostructure, covalent bonds by chemical reactions are used. Covalent organic network are even more stable than supramolecular networks. But it needs new strategies and reaction types.

In this thesis, the self-assembly of four organic molecules adsorbed on well defined metal surfaces was studied by using a scanning tunneling microscope (STM) and X-ray spectroscopy. STM provides information regarding the molecular surface footprint and their organisation on the single molecule level. X-ray photoelectron spectroscopy (XPS) complements our studies with in-

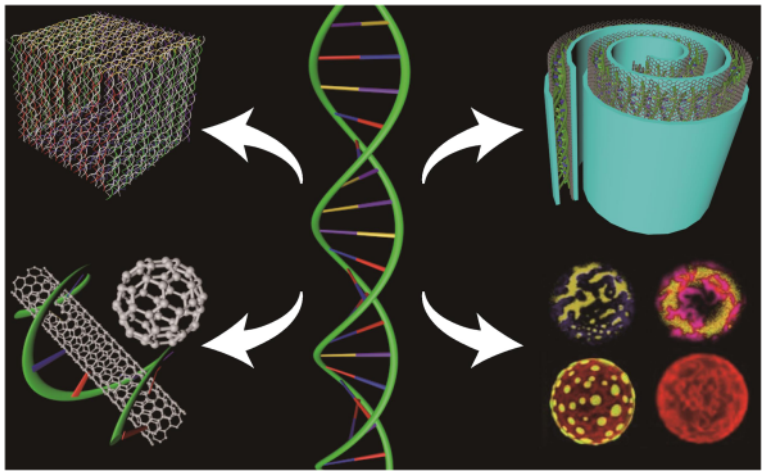

Figure 1.1: DNA biological applications in nanotechnology. Image adapted [3].

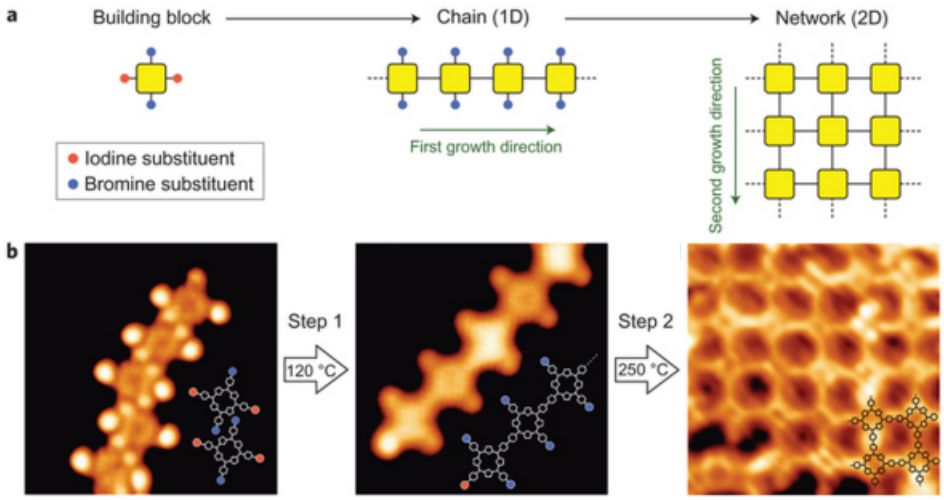

Figure 1.2: Low dimensional nanostructures formed by covalent bonding. Image taken from [9].

formation regarding the chemical state of the functional moieties of the molecular ensemble. Finally, near edge X-ray absorption fine structure (NEXAFS) probes the average orientation of the molecule with respect to the surface. The molecules employed are shown in Figure 1.3.

All molecules were studied by means of an STM, and especially, 2H-TPP and DES molecules were additionally investigated by XPS and NEXAFS. Chapter 2 will give a short description and explain in detail the experimental setup. Chapter 3 consists of three sections of results and discussion. The first section concern a small biologically relevant molecule, diethylstilbestrol. The molecule was found to adopt a *cis* or *trans* conformation guided by the substrate. It is well known for its adverse health effects : it is both a cancerogen and affects the DNA methylation processes,

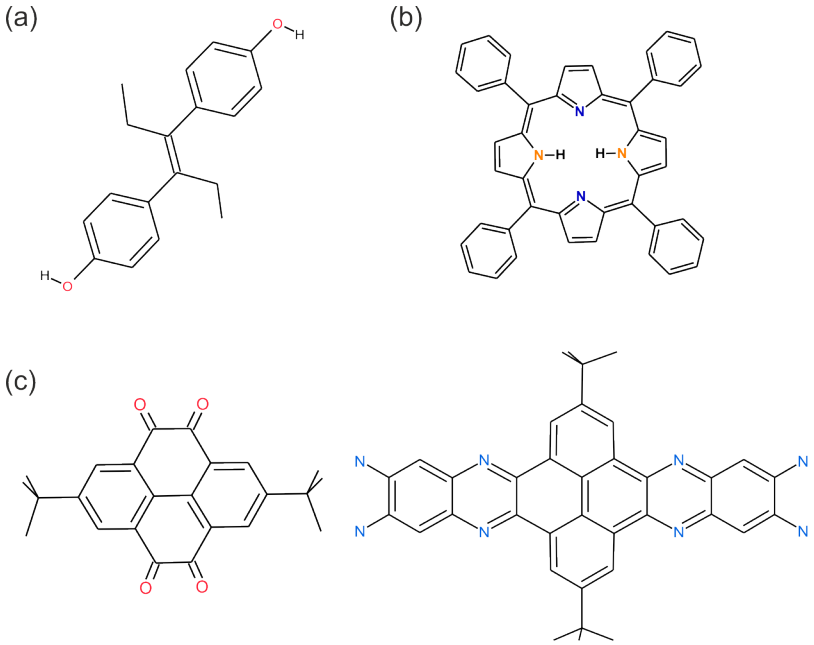

Figure 1.3: Chemical structures of (a) diethylstilbestrol, (b) 2H-tetraphenylporphyrin, (c) tetraketone **PT** (left) and tetramine **PPD** (right).

thus altering the epigenetic code of the DNA. We studied this species adsorbed on Ag(111) and Cu(111) as a function of temperature. The weak substrate interactions on Ag(111) results a *trans*-conformation but the stronger substrate interaction on Cu(111) substrate results in most of the molecules having a *cis*-conformation mediated by deprotonation to phenolate. The second section describes the thermal chemistry of a *meso*-tetraphenylporphyrin (2H-TPP) on the Ag(111) and its metalation with a Ru metal precursor. The 2H-TPP molecule has been reported to adopt a saddle-shape conformation on the Ag(111) surface. The macrocycle phorphyrin can capture metal atoms originating from a metal precursor. With annealing on Ag(111) the 2H-TPP first undergoes an intramolecular cyclodehydrogenation. At higher annealing temperatures homo-coupling by the formation of new intermolecular C-C bonds occurs. The third section discusses a covalent coupling by a ketone - amine reaction. We studied two molecules supported on the Ag(111) metal surface; one is a ketone and other one an amine. Both molecules can react on the metal surface at high temperatures. Chapter 4 gives a summary, the conclusions and an outlook regarding future perspectives.

2 Experimental Methods: Theory and Setup

The following chapter describes the techniques and instrumentation employed for the experiments performed in the context of the presented thesis. The first section gives a brief overview on the physical principles of the tunneling effect, followed by a general description of STM, the details of the variable-temperature STM and the ultrahigh vacuum chamber setup as well as the distinct preparation procedures. Two of the presented STM experiments were supported by additional X-ray spectroscopy measurements, which were performed at the *HE-SGM* beamline at *BESSY II* and in ELETTRA. Therefore, a brief description of the theoretical background of XPS and NEXAFS is presented together with the succinct description of the local setup.

2.1 Scanning tunneling microscopy

The STM was introduced by G.Binnig and W. Rohrer at the IBM research laboratory in 1981 [10]. They were awarded the Nobel prize in physics five years later [11]. STM has been widely used as an important tool for real space analysis in surface science and is a powerful instrument with atomic resolution to study surface properties. STM can be used in various environments not only in ultra-high vacuum but also in atmosphere, in liquids and at temperatures ranging from low K to a few hundred K. STM uses a sharp tip which is normally made by an electrochemical etched tungsten wire, mechanical sheared platinum-iridium alloy or gold and carbon based tips [12–19]. The tip can be approached to the surface by a piezoelectric tube which can position the tip in all three dimensions, until a tunneling current can be measured at approximately ~ 10Å by applying a bias of about 1 V between the sample and the tip. The tunneling current exhibits an exponential dependence to the distance from the surface, which permits atomic resolution.

2.1.1 Tunneling Effect

The basic concept of the tunneling effect arises from quantum mechanics. In classical mechanics, an object can not penetrate a potential barrier. In quantum mechanics, particles have also wave like charateristics and can pass through a wall, referred to as tunneling (see Figure 2.1). The time independent Schrödinger equation describes the one dimensional wave function of an electron :

$$\left(-\frac{\hbar^2}{2m}\frac{\partial^2}{\partial x^2}+V(x)\right)\psi(x)=E\psi(x) \tag{2.1}$$

Here m is the electron mass, $\hbar$ is $h/2\pi$ where h is the Plank's constant, ψ is the wave function, E the electron energy and V(x) the external potential acting on the electron at point x.

The wave function solutions can be written for the regions I, II and III (see figure 2.1) for the energy of the electron E lower than the barrier potential V_0 is given by

$$\psi_I = Ae^{ikx}+Be^{-ikx}, k=\sqrt{\frac{2mE}{\hbar^2}} \tag{2.2}$$

$$\psi_{II} = Ce^{-ikx}+De^{ikx}, k=\sqrt{\frac{2m(V_0-E)}{\hbar^2}} \tag{2.3}$$

$$\psi_{III} = Fe^{ikx}+Ge^{-ikx}, k=\sqrt{\frac{2m(E-V_0)}{\hbar^2}} \tag{2.4}$$

The coefficients A to G are determined from the boundary conditions and the requirements that the wave function and the derivatives should be continuous. In the region where I ($V < E$), the classical allowed regime (A = 1), the solution for the wave function is given by :

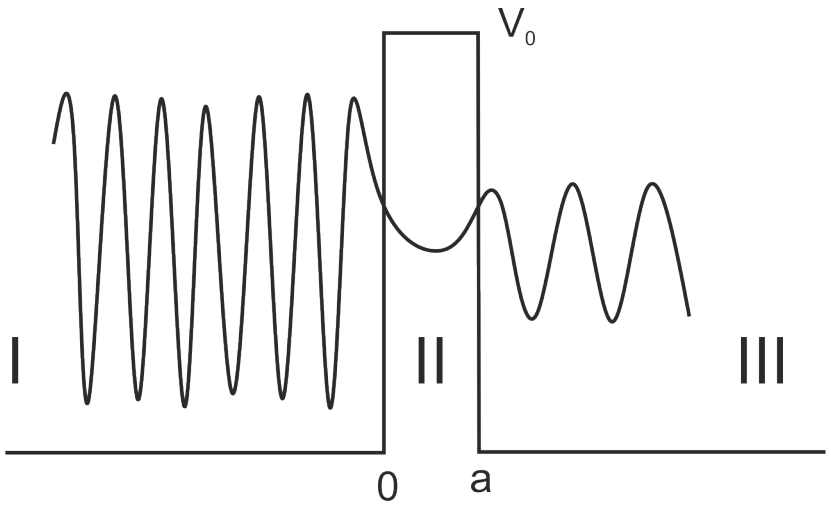

Figure 2.1: Wave function of quantum tunneling through a barrier. In classical dynamics, a particle can not penetrate the barrier. But in quantum mechanics, a particle can pass through the wall.

$$\psi(x) = \psi(0)e^{\pm i\sqrt{\frac{2m(E-V_0)}{\hbar^2}}x} = \psi(0)e^{\pm ikx} \tag{2.5}$$

That means the electron is moving in the positive or negative x direction with a constant momentum and velocity, similar to the classical case. If one takes a look at region where II ($V > E$), the electron can not propagate in classical mechanics (G = 0), but in quantum mechanics there is a solution for the Schrödinger equations.

$$\psi(x) = \psi(0)e^{-\sqrt{\frac{2m(V_0-E)}{\hbar^2}}x} = \psi(0)e^{-kx} \tag{2.6}$$

The electron can penetrate the barrier and one can describe the so called tunneling current in region III by its transmission coefficient:

$$I = |F|^2 = \frac{1}{1+\frac{V_0^2}{4E(V_0-E)sinh^2(2ka)}} \tag{2.7}$$

For $ka \gg 1$ it can be simplified to

$$I \propto e^{-2ka} \tag{2.8}$$

This means the tunneling current (I) is proportional to the distance between metals (a). Depending on the thickness and the height of the barrier there is a exponential decay in x direction inside the barrier. But this indicates, that behind a finite barrier there is still a probability of presence, i.e. the electron can tunnel through the barrier.

Based on this quantum mechanical phenomena STM can be explained as the tunneling of elec-

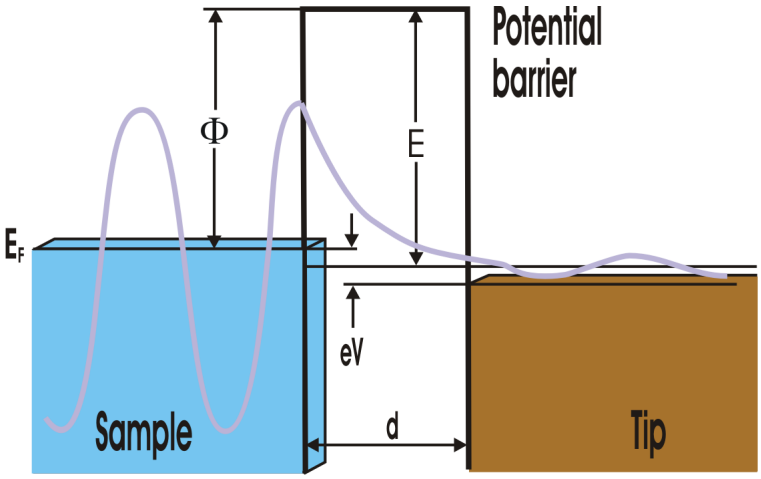

Figure 2.2: One-dimensional sample-vacuum-tip tunneling junction. Electrons can tunnel through vacuum between the sample and the tip with a decaying wavefunction. To the left, the sample is described as a box with a one-dimensional wavefunction penetrating into the potential barrier region between the sample and the tip to the right, leading to a non-zero probability for an electron to tunnel from the sample into the tip [20, 21].

trons between sample and tip when a bias voltage is applied. Figure 2.2 shows a simplified schematic energy diagram of a tip being in tunneling contact with a surface. As a bias voltage is applied between tip and sample, electrons from occupied states of the tip tunnel to unoccupied states in the sample. As electrons can only tunnel from occupied to unoccupied states, the density of states (DOS) level in the tip and the sample has to be accounted for in the calculation of the tunneling current. In perturbation theory, the tunneling current is :

$$I = \frac{2\pi e}{\hbar}\sum_{\mu,v} f_{\mu v}|M_{\mu v}|^2 \tag{2.9}$$

where $M_{\mu v}$ is the tunneling matrix element between the states ψ_μ and ψ_v tip and surface, respectively. The function of $f_{\mu v}$ implicitly depends on the voltage and represents Fermi distribution:

$$f_{\mu v} = \{f(E_\mu)[1-f(E_v)] - f(E_v)[1-f(E_\mu)]\}\delta(E_\mu + U_b V - E_v) \tag{2.10}$$

where E_μ is the energy of ψ_μ, relative to the Fermi level of the electrode, and U_b is the applied bias voltage in units of energy $e(U_b)$ [22]. In the sample $1-f(E_v)$ delivers the probability that the quantum state at the energy E_v is empty in the sample. f_v gives the probability that the quantum state at the energy E_v is occupied in the sample. In the case of the tip, $1-f(E_\mu)$ is the probability that the quantum state at the energy E_μ is empty. When the Fermi function is replaced by unit step functions (T=0), and for small voltage U_b, the tunneling current is given by

$$I = \frac{2\pi}{\hbar} e^2 V \sum_{\mu,v} |M_{\mu v}|^2 \delta(E_\mu - E_F)\delta(E_v - E_F) \tag{2.11}$$

If the tip wave functions are arbitarily localized, the matrix element is simply proportional to the amplitude of ψ_v at the position $\vec{r_0}$ of the probe [23]. For s-wave tip, equation (2.11) reduces to:

$$I \propto \sum_v |\psi_v(\vec{r_0})|^2 \delta(E_v - E_F) \tag{2.12}$$

At the position of the tip, the tunnel current is proportional to the surface local density of states (LDOS) at E_F. The predominant tip state involved in the tunneling process is an s-state and the wave function of tip and sample do not influence each other . For small bias voltage (U_b) the tunneling current is then proportional to the LDOS of the sample (Tersoff-Hamann model [23])

$$I \propto U_b e^{-2kR} \rho_\mu(E_F)\rho_v(E_F, r_0) \tag{2.13}$$

where R is the radius of the tip and $k = \sqrt{\frac{2m\Phi}{\hbar^2}}$ is the minimum inverse decay length for the wave functions in the vacuum gap with a local barrier height Φ. r_0 is the position of the center of the spherical tip-apex in respect to the surface. This shows that an STM image can not be seen as a topograph of the sample surface alone but as a convolution of topographic and electronic information.

2.1.2 Operation principle

The STM is based on the concept of quantum tunneling as described above. When a conducting tip is brought very close to the surface and a bias voltage is applied between the two, electrons can tunnel through the vacuum between them. The resulting tunneling current is a function of tip position, applied voltage, and the LDOS of the sample. STM can be a challenging technique, as it requires extremely clean and stable surfaces, sharp tips, excellent vibration control, and sophisticated electronics.

There are two operation modes illustrated in Figure 2.3. Constant height mode (CHM): the height of the tip is kept constant from the surface during scanning at a given bias voltage. Due to the fixed tip distance from the surface, this mode does not use any control of the feedback loop. The CHM is suitable for a flat surface and small areas to avoid a risk to crash the tip or break tunneling contact by steep step edges or contaminations on the surface. One advantage of this mode is a fast scanning speed. The other operation mode is the constant current mode (CCM): this mode is normally used to scan the surface and was exclusively utilised in this thesis. To keep the tunneling current constant, the distance between the tip and the sample is readjusted by a feedback loop system. This mode has the advantage to be less sensitive to rough surfaces and large scanning areas but is often slower, since the tunneling current has to be kept constant by the feedback loop

during scanning.

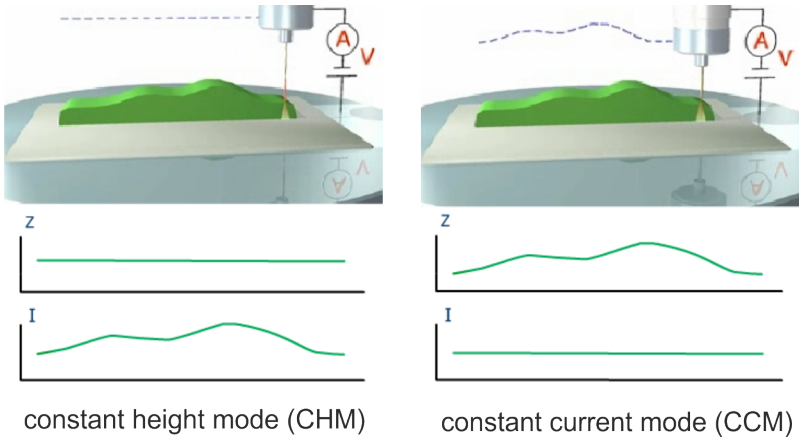

Figure 2.3: STM operation modes: constant height mode (left) and constant current mode (right) (Z: apparent distance between tip and sample, I: tunneling current, V: bias voltage in between tip and sample) [24].

2.1.3 Experimental set up

The instrument is a custom made two UHV chamber design as shown in Figure 2.4. In one chamber a variable temperature Aarahus STM (a,b) is placed at a base pressure of $\sim$3 x 10^{-10} mbar and the other one serves as a preparation chamber (c). The preparation chamber is equipped with organic molecular beam epitaxy (OMBE) (d) and a metal beam evaporator (g). A load lock (f) is connected to the STM chamber. A turbo molecular pump which is located at the preparation chamber (c) can reach a pressure of 2 x 10^{-10} mbar. The STM chamber can be separated by a vertical gate valve from the preparation chamber. In order to transfer the sample, we use manipulators with a magnetic coupling. There are four manipulators and the longest one can move the sample from the preparation chamber to the STM chamber. Two small manipulators are at the STM and preparation chamber which can put the sample into the STM stage and sample storage at the preparation chamber. Another manipulator is the located at the load lock to transfer the sample to the outside. This load lock can also be used to dose materials with a low vapor pressure. To clean tip and sample, we can use argon sputter guns (e) in both chambers. The OMBE can contain up to four different molecules at the same time which are in quartz crucibles with a diameter of 5 mm and sublimed into vacuum by resistive heating. The temperature is measured at the crucible holder. The distance between sample and OMBE is about 15 cm. In the sample parking stage (h), up to four samples and one shielding plate for the tip sputtering can be stacked. The sample on the stage is heated by electron beam heating with acceleration voltages of up to 800 V. With radiative heating, samples can be heated to temperatures up to 470 K, which is sufficient to anneal certain

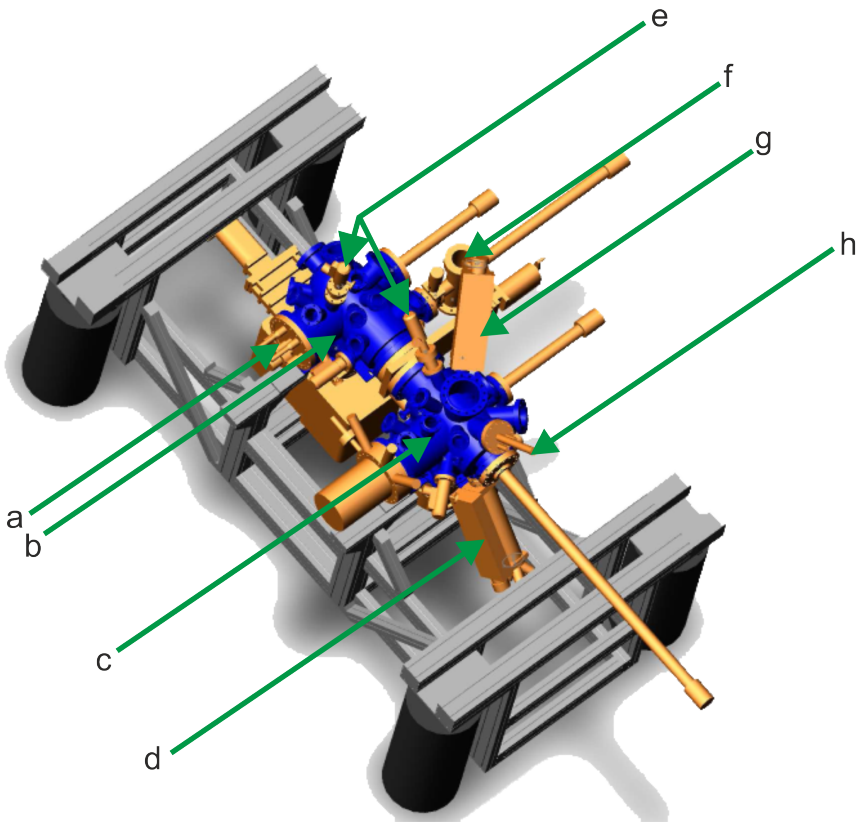

Figure 2.4: Set up of the UHV chambers (a) the variable temperature Aarhus STM, (b) STM chamber, (c) preparation chamber, (d) OMBE, (e) argon sputter gun, (f) load lock, (g) metal beam epitaxy, (h) sample parking stage [25].

surfaces. Tungsten tips were used for all experiments. The tips were premounted on a copper tip holder plate and sharpened by electrochemical etching.

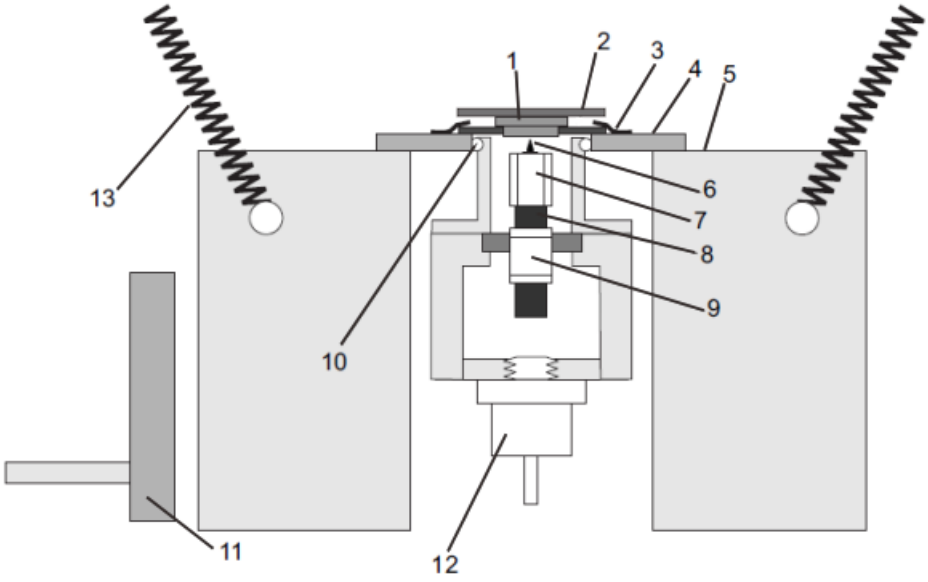

Figure 2.5: Cross-section of the Aarhus STM. (1) sample, (2) sample holder, (3) copper clamps, (4) top plate, (5) aluminium block, (6) tungsten tip, (7) piezoelectric tube scanner, (8)SiC rod, (9) inch worm piezo motor, (10) ceramic balls, (11) cold finger, (12) Zener diode, (13) suspending springs [26].

Figure 2.5 shows a cross-section of the Aarhus STM. The sample (1) is mounted on a sample holder (2) which is fixed by 4 screws. The sample holder is fixed with clamps (3) at the top plate (4). The top plate is in firm contact with an aluminium block (5), while the inner scanner thermally insulated from the aluminium block to stay at a fixed temperature when performing experiments at low or elevated temperatures. The tip (6) is mounted at the end of a piezo tube scanner (7). The piezo tube scanner is divided into four equal sections coated with conducting gold layers which are used for the x, y and movement by applying high voltages. The piezo tube scanner is glued to a SiC rod (8), which is moved by an inchworm motor (9), which is used for the coarse approach of the tip to the surface. The STM is attached to the outer aluminium block by three electrically insulating ceramic balls (10). The aluminium block can be cooled by the cold finger (11) with a liquid nitrogen flow cryostat. During cooling, a Zener diode (12) keeps the scanning part at room temperature. In order to prevent vibrational noise, the STM block hangs freely suspended on springs (13).

2.1.4 Sample preparation

A copper (111) and a silver (111) crystal were used in the STM and X-ray spectroscopy measurements. In order to investigate molecular deposition and self-assembly on the surface, the single crystal needs to be clean and atomically flat. Therefore the crystals were prepared by several cycles of sputtering and annealing steps. By sputtering, the surface is ablated by an argon ion beam. For the sputtering we used an argon pressure around 2 x 10^{-5} mbar. The sputter gun can ionize the argon and accelerate it towards to the sample with a acceleration voltage of 1 kV. We can measure the argon ion current at the sample holder to be typically 27 μA. After sputtering, to smoothen the surface again, we anneal the sample with electron beam heating. We measured the sample temperature at the sample side clamps. The annealing temperatures for Ag and Cu were 600 K and 700 K, respectively. If metal precursors were dosed on surface, the crystal surface needed more extensive cleaning cycles with a higher Ar+ emission current of about 30μA and longer sputtering durations (60 to 120 min vs. 20 to 30 min). After annealing the surface we wait for the sample to cool down to room temperature before dosing molecules. We studied four compounds: Diethylstilbestrol (DES), 2,7 - di- tert-butyl - 4,5,9,10 - di-pyrazine - o - phenylenediamine(**PPD**), 2,7-di-tert-butyl-pyrene-4,5,9,10-tetraone (**PT**) and *meso*-tetraphenylporphyrin (2H-TPP) were dosed onto the clean metal surface by using the OMBE. STM measurements were carried out from 100 K to 300 K. The STM was pre-cooled with liquid nitrogen to a minimal temperature of 90 K. For the analysis of the STM measurements, images were processed with the WSxM software [27]. For the preparation of the amine - ketone reaction, we used the two monomers are the tetramine (**PPD**) and the tetraketone (**PT**).

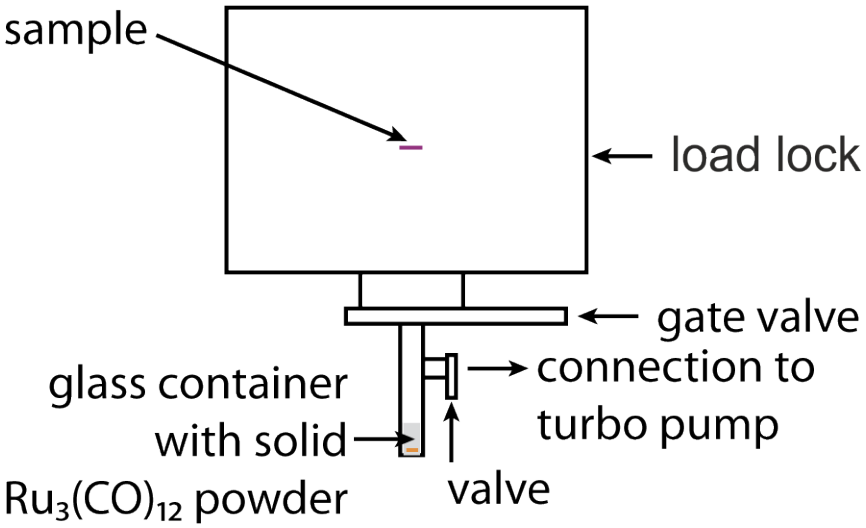

Figure 2.6: Schematic of $Ru_3(CO)_{12}$ dosing set up [28].

For preparation of 2H-TPP molecules with Ru-precursor, we used the meta-organic chemical

vapor deposition (MOCVD) approach for the metal-organic complexation and reactions at interfaces, which has the advantage of requiring minimal instrumentation and being applicable even outside vacuum [28]. After dosing the 2H-TPP molecule onto the Ag(111) surface, the sample was transferred to the load lock at the side of the STM chamber with a base pressure of about 1.5 x 10^{-8} mbar for dosing the metal precursor as shown in Figure 2.6. A glass container with solid precursor powder was placed with a line of sight to the sample.

Molecule	Manufacturer	Purity	Dosing T/K	Sample T/K	Measure T/K
2H-TPP	Sigma aldrich	$\geq 99\%$	598	300	90 - 300
DES	Sigma aldrich	99%	388	300	160 - 300
PT	Macromolecular		473	300	120 - 300
PPD	Design and Engineering		653	300	140 - 300

Table 2.1.1: Sample preparation: molecules, crucibles temperature for dosing at OMBE, sample temperature at dosing, temperature of the measured surface on the STM stage.

2.2 X-ray spectroscopy

X-ray spectroscopy techniques are widely used to understand the chemical state of molecular layers on surfaces, and probe the occupied and unoccupied electronic states. In this section, a short introduction of XPS and NEXAFS spectroscopy will be given. To do these experiments, the monochromatic light source at the HE-SGM beamline at BESSY II synchrotron in Berlin was used. The synchrotron radiation was discovered by researcher in the General Electric in 1947s [29]. The synchrotron radiation is electromagnetic radiation emitted by relativistic electrons moving on curved paths. The electrons accelerated in a storage ring and emit it to the beamlines. The X-ray radiation is being used for experiments in surface science such as surface physics, solid state, and many other areas. The measurement of the energy of photoelectrons produced by the photon beam at different angular incident to the surface is a very powerful technique for understanding the electronic structure and the chemical state such as deprotonation, oxidation, and corrosion. In order to understand the molecular structure on surface, the sample preparation was performed in the same way as in the STM experiments.

A synchrotron radiation facility consists of a storage ring and a booster, where the charged particles are accelerated close to the speed of light before being injected into the storage ring. A monochromator in the beamline helps to select a single wavelength thus providing a monochromatic X-ray source for the experimentalists. The degree of polarization is determined by the X-ray energy and the beamline opics [30].

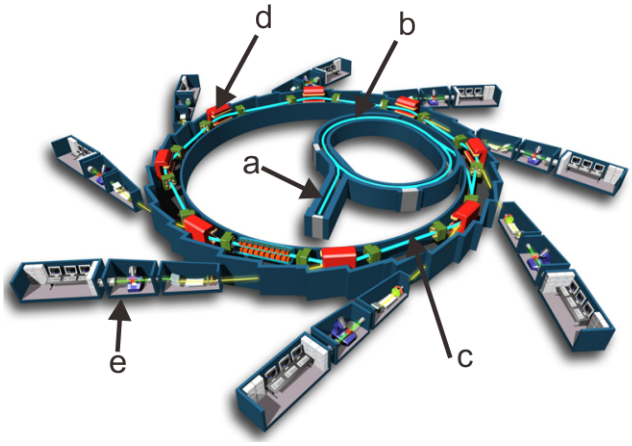

Figure 2.7: Synchrotron radiation system consisting of a microtron injector (a), accelerating electrons to $\sim$ 100 MeV, (b) a booster, which accelerates electrons to $\sim$ GeV and emits them to the storage ring (c) where electrons pass through the (d) undulator where the synchrotron radiation is generated and passed into (e) the several separated beamlines. Image adopted from [31].

2.2.1 X-ray phtoelectron spectroscopy

The basic principle of this technique relies on the photoelectric effect which is sketched in Figure 2.8. The energy spectrum of the photoelectrons will reproduce the electronic structure of an element. The characteristic binding energies of the elements can be identified in the in the spectrum. Often these binding energies exhibit chemical shifts, which vary from a fraction of an eV up to several eVs. The binding energy shifts observed in XPS origin in initial - and final state effects. The initial state effects, such as the charge on the atom prior to photoemission, plays the major role in the determination of the magnitude of the chemical shift.

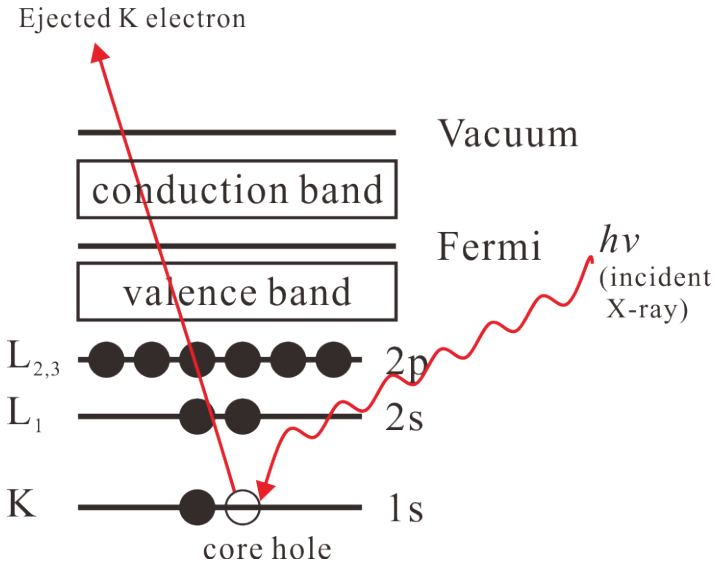

Figure 2.8: Schematic XPS process, showing photo electron emission of an 1s electron.

The kinetic energy of the emitted photoelectron is analyzed by an electron spectrometer and the photoelectron spectrum is presented with intensity versus electron energy. For XPS, the photon energy has to be high enough to ionize the core levels from the atoms of interest. The kinetic energy E_K of the electron is the experimental quantity measured by the spectrometer. It depends on the photon energy of the X-rays which is not an intrinsic material property and on the binding energy E_B of the electron. The equation between the parameters involved in the XPS measurement is

$$E_B = h\nu - E_K - W \tag{2.14}$$

where $h\nu$ is the photon energy, E_K is the kinetic energy of the electron, and W is the work function of the material. The binding energy of the core level electrons is characteristic for each element and the chemical shifts can be used to identify the chemical environment of the element.

2.2.2 Near edge X-ray absorption fine structure spectroscopy

In this work, the two molecules, DES and 2H-TPP, have been investigated with NEXAFS spectroscopy. This technique is more complex than XPS, but it has the advantage to give informations such as the molecular orientation with respect to the surface as well as intramolecular conformations. Here, a core level electron is excited by X-ray absorption into an unoccupied state. The core hole will be refilled by emission of an Auger electron or radiative decay of an upper shell electron. The measured quantity is the number of Auger electrons emitted from the surface, which is proportional to the absorbed X-rays and thus a measure for the absorption cross section of the excitation process. The unoccupied state resonances are labeled as π^* orbitals or σ^* orbitals along with their symmetry. The π^* orbitals are located below the ionization potential (IP) state which leads to sharp resonances and the σ^* orbitals are found at higher photon energies which leads to broad spectrum according to the life time of the excited state (see Figure 2.9).

The absorption coefficient is proportional to the cross section which can be described with initial, final state and electric field vector by Fermi's Golden Rule [32]. The absorption intensity depends on the symmetry of the final state orbitals relative to the electric field vector. For example, a benzene ring is lying flat on the surface so that the sigma bonds are parallel to the surface and the π orbitals perpendicular to the surface. If the E-field of the incident field is perpendicular to the surface, the absorption cross section of the π resonance is at an maximum, whereas the absorption cross section of the sigma resonance is minimal (see Figure 2.10).

2.2.3 Experimental set up

Figure 2.11 (a) shows the end-station of the HE-SGM beamline at BESSY II. It consists of three chambers which are the analysis chamber, distribution chamber (UFO) and preparation chamber. The preparation chamber is equipped with a sputter gun and an OMBE, which base pressure is 1.5 x 10^{-9} mbar. After cleaning the substrates and dosing the molecules in the preparation chamber, the sample is transferred by the manipulator in the UFO distribution chamber with a base pressure of 8.6 x 10^{-10} mbar (see Figure 2.11 (b)). The UFO distribution chamber is equipped with a magazine and a load lock for sample parking and transfer. The sample can be rotated and transferred to the analysis chamber. The analysis chamber is equipped with a Scienta R300 hemispherical electron energy analyser for analysis data which is connected in an angle of 45° with respect to the direction of the incoming photon beam from the beamline as shown in Figure 2.11 (c). The base pressure of the chamber is 8.9 x 10^{-10} mbar. A channeltron detector is used for the NEXAFS measurements. The manipulators in the analysis and preparation chambers are able to heat and cool the sample between 100 K and 870 K by means of the electron beam heating and the liquid nitrogen cooling. The XPS spectra are taken at normal emission and are calibrated are fitted a Gaussian to the $Ag3d_{5/2}$ and $Cu3p_{3/2}$ peak of the substrate reference. The C 1s region

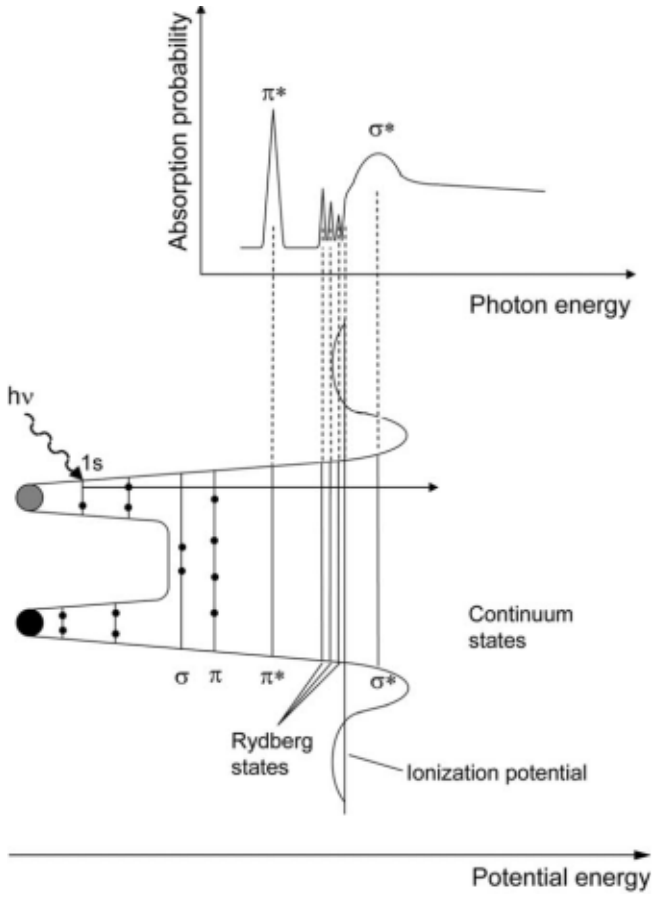

Figure 2.9: Principle of NEXAFS spectroscopy: potential (bottom) and K-shell spectrum (top) of a diatomic molecular (sub)group. In addition to Rydberg states and a continuum of empty states similar to those expected for atoms, unfilled molecular orbitals are present, which is reflected in the absorption spectrum. Image adopt from [30].

is treated with a Shirley background and the O 1s is treated with a linear background [33]. Both peaks were fitted with Voigt functions which by amplitude, binding energy, width and shape. The carbon K-edge spectra was recorded in partial electron yield (PEY) mode with a retarding voltage of -150 V to prevent slow electrons from reaching the detector. The incidence angle θ between linear polarized light and surface is controlled by rotating the sample with respect to the incoming beam. Three different angles of incidence, grazing(25°), magic angle(53°) and normal(90°), were recorded. The NEXAFS spectra are calibrated by the characteristic peak for carbon at 285.0 eV. Afterwards, the spectra of each incidence angle were averaged, smoothed and normalized to the pre-edge region to account for differences in the ring current. Then, the reference signal of the bare was subtracted from the spectrum.

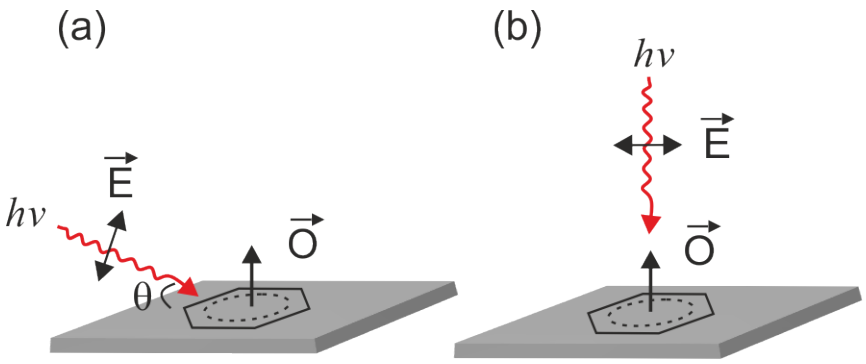

Figure 2.10: Schematic of X-ray absorption of an benzene ring. (a) Grazing incidence: $\vec{E}$ is approximately parallel to the orbital orientation $\vec{O}$ and the π^* resonances has maximal absorption intensity. (b) Normal incidence : $\vec{E}$ is perpendicular to $\vec{O}$ so that the σ^* resonance has maximum absorption intensity [32].

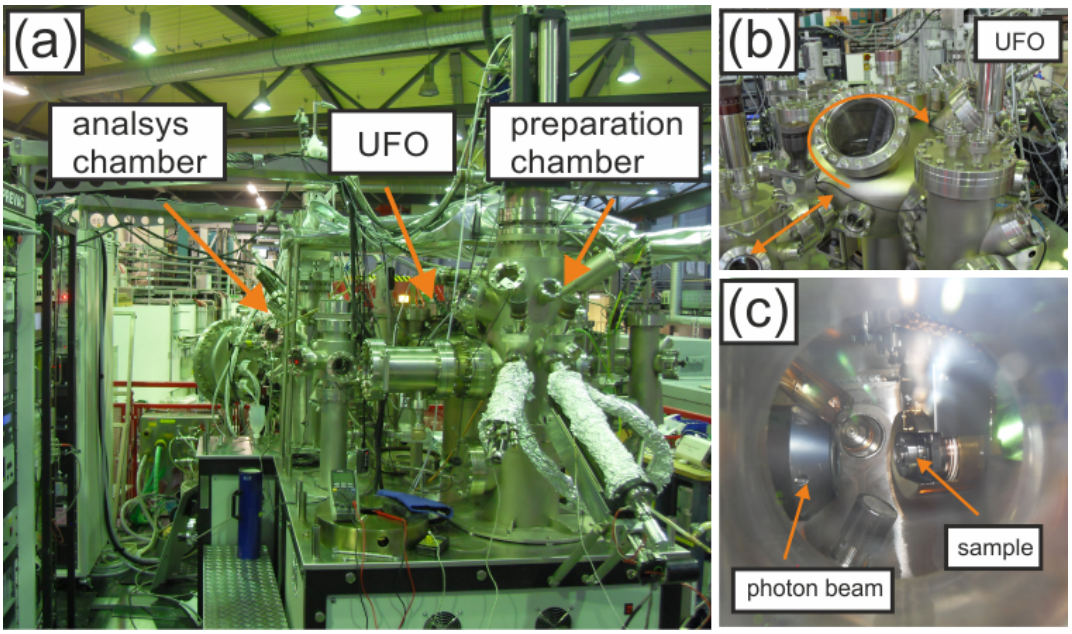

Figure 2.11: The end-station of the HE-SGM beamline at BESSY II consists of the analysis chamber (a and c) where the XPS and NEXAFS data are taken, the distribution chamber "UFO" (b) for the sample transfer to the different chambers, and the preparation chamber to clean the surface and dose the molecules.

3 Results

In this chapter, the results of the investigations carried out during this thesis examining four different molecules are presented. The different molecules diethylstilbestrol, 2H-tetraphenylporphryin, **PT** and **PPD** were examined by means of STM, XPS and NEXAFS. The molecules undergo varying chemical transitions driven by high temperature annealing such as deprotonation, dehydrogenation, and dehydration. Thus, the molecules reveal various molecular orientations and interactions according to the detached hydrogen atoms. Section 3.1 describes a deprotonation of diethylstilbestrol and isomerization as a function of the temperature on Ag(111) and Cu(111). Section 3.2 demonstrates metal and organic molecular interactions for a self-metalation reaction by exposure to ruthenium precursors. At high temperature, the molecules show a cyclodehydrogenation. Section 3.3 describes a ketone - amine reaction between **PT** and **PPD** molecules aiming to form covalent networks by dehydration on a Ag(111) surface.

3.1 Steering the conformation of diethylstilbestrol by the metal surface

Diethylstilbestrol (DES, IUPAC name: 4,4'-(3E)-hex-3-ene-3,4-diyldiphenol) is a nonsteroidal estrogen that was first synthesized by Charles and colleagues in 1938, two years after their creation of a similar chemical named bisphenol A (BPA). DES was widely administered to pregnant women to prevent miscarriage. These exposed women showed a higher risk to develop cancers such as breast cancer, prostate cancer, and ovarian cancer [34–36]. Already in the 70th it was found, the DES is teratogeneous that this symptoms can be inherited to the next generation [36, 37]. Therefore DES was banned by Food and Drug Administration (FDA) to be used by pregnant women. Additionally it is been suspected to interfere with DNA (de)methylation processes [38–41].

The reactivity and self-assembly of the very similar molecule BPA (Bisphenol A: 4,4′-(propane-2,2-diyl)diphenol) on Cu(111) was recently published [42]. BPA is used in plastics such as bottles and also known to have adverse health effect (for example epigenetic alternations) [43] by DNA methylation [43, 44] similar to DES. This molecule has been discussed in the master thesis of Julian Lloyd and the Ph.D. thesis of Sybille Fischer [42,45] and will not be described here in more detail.

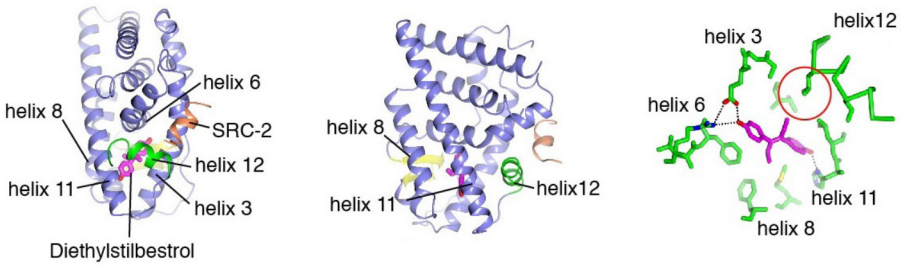

Figure 3.1: Estrogen receptor structure and ligand sets with DES ligand-binding domain is shown as ribbon (left and central), with helix 12 bound to diethylstilbestrol. The right panel shows details of the ligand-binding (dashed line), with the protein colored green and the ligand colored magenta [46].

In this study of DES, we focus on the characterization of the self-assembly of DES on both, Ag(111) and Cu(111) surfaces as a function of annealing steps by STM and correlated experimental methods as XPS and NEXAFS of the C K-edge as a function of the photon incidence angle. For a better understanding of the chemical state of the molecules after distinct annealing steps, the spectroscopy study is going to be addressed first, followed by the STM structural analysis.

DES contains a stillbene with two alcohol groups at the outer phenyl rings and two ethyl groups at the double bond. Due to central double bond, the molecule has two isomers : a *trans* and a *cis*

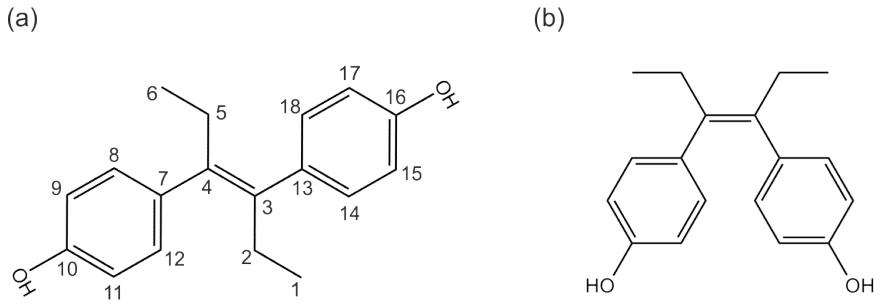

Figure 3.2: Diethylstilbestrol (DES): chemical structure in *cis*- and *trans*-isomer conformation, (a) *trans*-configuration with IUPAC numbering and (b) *cis*-configuration.

conformation [47]. Typically, the phenol groups can be used as an interacting groups to control the molecular self-assembly process [48]. Figure 3.2 shows the molecular structure with the two isomers (a) *trans*- and (b) *cis*-conformation that DES have sp^2 hybridized at central double bond and 1.2 nm between oxygen atoms [45,49]. The DES molecule is an achiral molecule in gas phase but we found DES to form chiral molecular superstructures at the surface.

3.1.1 DES on Ag(111)

XPS We measured the O 1s and C 1s core level binding energies of DES adsorbed on Ag(111) at room temperature in order to figure out its chemical state. Figure 3.3 shows the O 1s (a) and C 1s (b) spectra after annealing steps to the indicated temperatures. The O 1s spectra (Figure 3.3 (a)) at 300 K shows mainly one peak at 533.4 eV which is assigned to -OH bound to a phenyl ring. Annealing to 330 K does not lead to a significant change in the spectra aside from the appearance of a second peak ($-O^-$) at 531.3 eV. The second peak is an indication for deprotonated hydroxyl groups and the first peak is shifted to 533.0 eV. After annealing to 350 K, two peaks in the spectra can be clearly distinguished. One is assigned to (-OH) at 532.8 eV (shifted in binding energy by about -0.4 eV) and the other is assigned to ($-O^-$) at 531.0 eV (see Table 3.1.1). Higher annealing to 370 K leads to desorption of the molecules, according to the intensity of peaks but not shown in this figure.

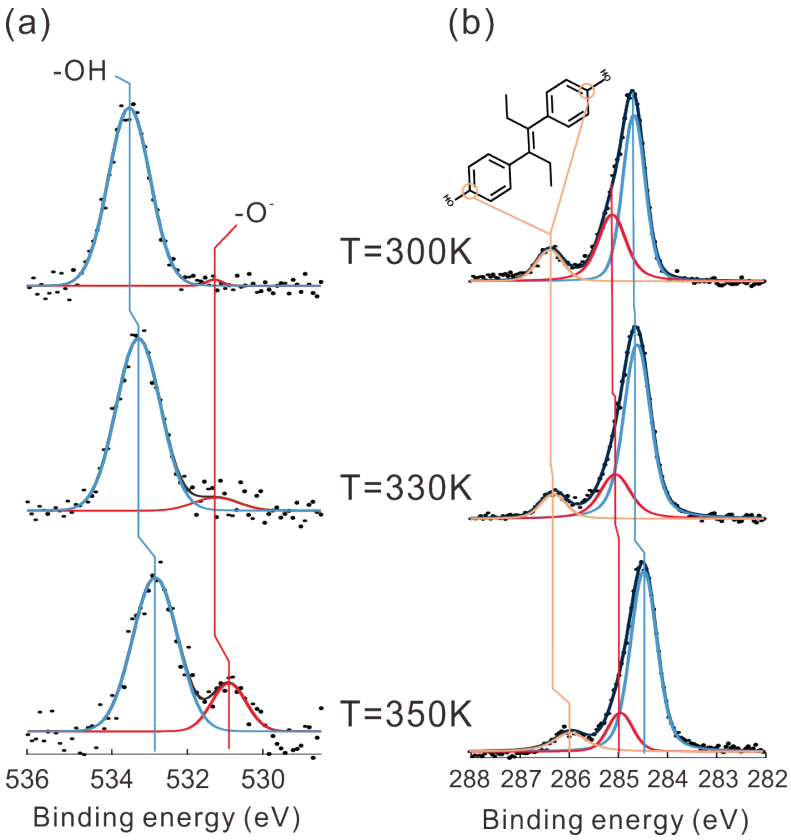

Figure 3.3: XP-spectra of O 1s (a) and C 1s (b) core level energies of DES adsorbed on the Ag(111) surface. The spectra were recorded at 200 K after annealing steps at temperature T.

In the C 1s spectra (Figure 3.3 (b)) are three peaks visible. The peak with the highest binding energy was assigned to the carbons C10 and C16 according to the scienta ESCA300 database [50].

The other peaks could not be assigned to specific carbon atoms. The intensity of the (C-OH) peak decreases during annealing but the other carbon peaks do not significantly change. All binding energies of the carbon peaks are gradually shifted by about -0.5 eV and fitted according to full width half maxima (FWHM).

T_{ann} (K)	Carbon		Oxygen	
	E_b (eV)	FWHM	E_b (eV)	FWHM
300	286.3	0.8	533.4	1.3
	285.2	0.6		
	284.7	0.6		
330	286.6	0.7	533.0	1.3
	285.0	0.8	531.3	1.2
	284.5	0.7		
350	286.0	0.8	532.8	1.3
	284.9	0.8	531.0	1.0
	284.5	0.6		

Table 3.1.1: XPS results after annealing at 300 K, 330 K and 350 K. The C 1s and O 1s spectra are fitted by binding energy and FWHM.

NEXAFS To get more informations of the molecular orientation, NEXAFS measurements were carried out after annealing steps at 290 K, 310 K, and 370 K at grazing incidence (25°), normal incidence (90°) angle, and an incidence angle of (53°) with respect to Ag(111) substrate plane. After deposition of the DES at room temperature, we found the molecular coverage is to be a multilayer of about 5 nm thickness so that NEXAFS can not give specific molecular informations at this preparation. Figure 3.4 (a) shows the normalized carbon K edge spectra with different angular incidence to the surface after annealing the sample to 310 K and 370 K. The highest intensity at 285.2 eV is assigned to the C 1s to π^* resonance. At a normal incidence angle of 90°, the intensity of the π^*resonances is not completely quenched, clearly marking that the layer contains phenol rings which are not oriented fully parallel to the surface.

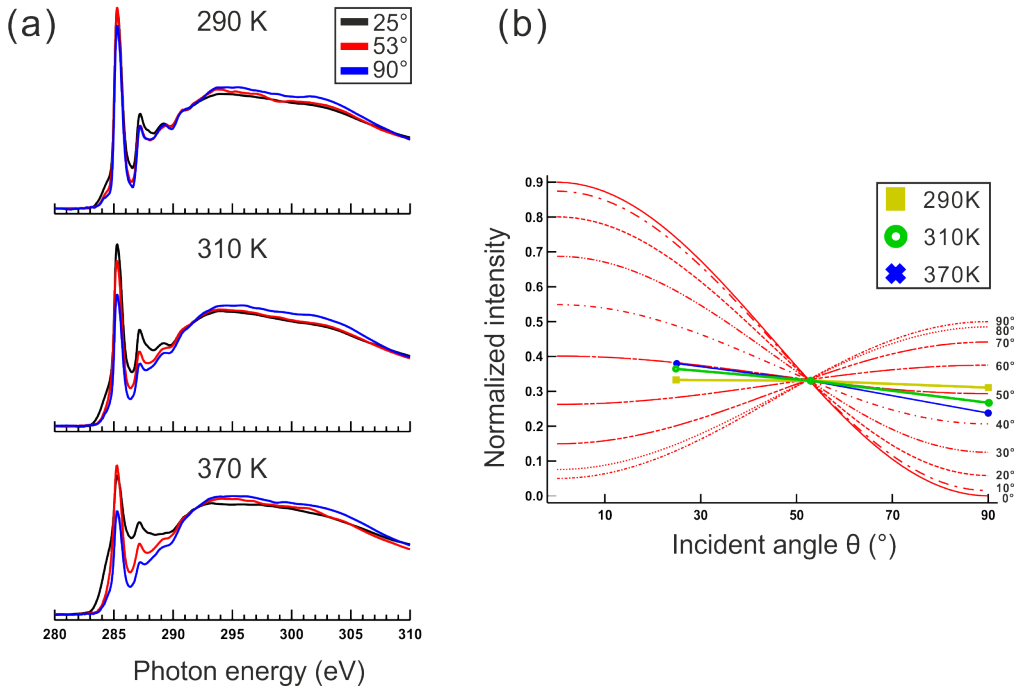

Figure 3.4: NEXAFS spectra of DES (a) normalized C K-edge spectra after annealing the sample to 290 K, 310 K and 370 K recorded at 150 K for three different photon incident angles. (b) The normalized intensity of the π^*resonance at 258.3 eV after annealing between 290 K and 370 K versus θ displayed together with the theoretical curves for different adsorption angles with respect to the surface suggests an average tilt angle of $\sim$50 $\pm$10° for the phenols.

The average tilt angle of the two phenol rings is estimated to be approximately between 45° and 55° with respect to the substrate plane (see figure 3.4b). Since the resonance energy of the two phenol is the same, we expect the angular dependence of the π^* resonance to contain contributions from both phenyl rings. The accuracy of NEXAFS analysis is $\pm$10° [42]. At all annealing temperatures, the curve fitting reveals a phenyl ring adsorption angle between 45-55°. Therefore we can present a tentative molecular model for the molecules adsorbed on a surface with the phenol groups tilted by $\sim$50° $\pm$10° with respect to the surface.

Molecular model on Ag(111) A model with the most reasonable molecular orientation is presented in figure 3.5. The molecule - surface interaction is driven mainly via the π-systems of the phenols and the affinity of the OH groups towards the silver surface. A possible adsorption model is that the both phenyl groups are tilted toward the substrate atoms according to the NEXAFS results so that molecules is slightly bent at the central double bond. As the ethyl groups sterically hinder a flat alignment of the phenols they are tilted in different directions with respect to the surface while the whole molecule remains in a *trans*-configuration.

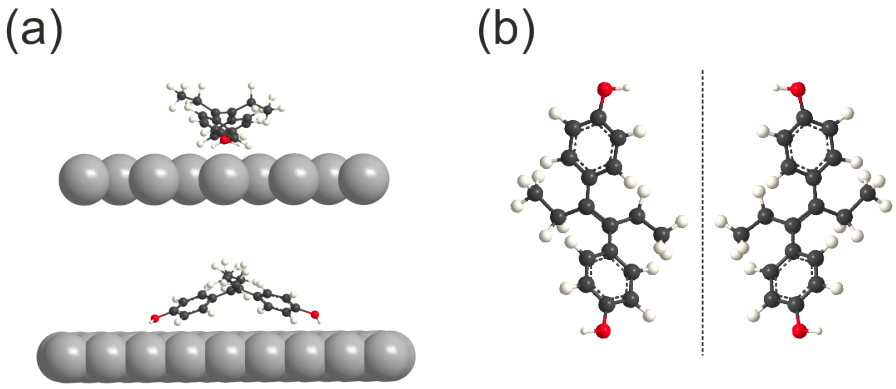

Figure 3.5: Ball and stick model of DES on the Ag(111) surface with side views of the molecule (a). The phenol rings are tilted with respect to the surface. (b) A top view with two possible surface enantiomers is displayed. Carbon, oxygen, hydrogen and silver atoms are indicated by small black, red, white and large gray spheres, respectively.

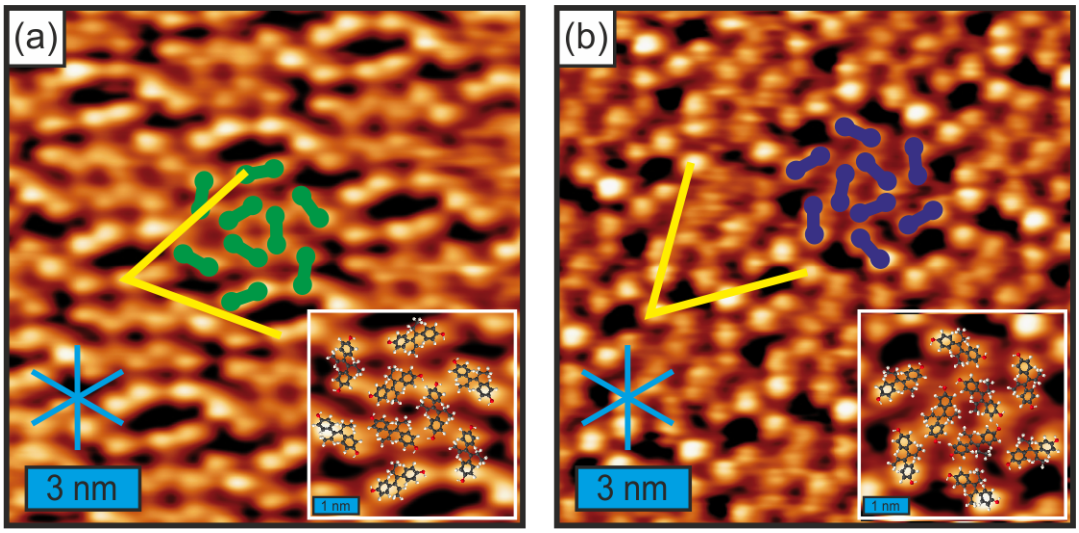

Figure 3.6: STM results of the molecules superimposed with molecular models. (a) Clock wise windmill motif with detail image (U_b = 1.49 V, I_t = 0.14 nA). (b) Counter clockwise windmill motif with detail image (U_b = 1.25 V, I_t = 0.14 nA). Both images recorded at room temperature. The yellow lines in the two images mark the hexagonal unit cell with side length of 4.0 nm.

The windmill motif To analyse the molecular structures and interactions on Ag(111), we performed an STM investigation at submonolayer coverage ($\sim$ 0.8 ML) after different annealing steps between room temperature and 400 K. After deposition of DES on Ag(111) surface at room temperature, we first observed a motif as shown in figure 3.6 which will be addressed in the following

as the 'windmill motif'. The same windmill motif can be identified in STM images recorded at temperatures between 140 K and 300 K. Figure 3.6 (a) shows a clockwise windmill motif. Detail images with superimposed molecular models are shown in the bottom right. The blue star shows the surface high symmetry axes. This molecular structure consists of nine paired protrusions with a hexagonal unit cell side length of 4.0 $\pm$ 0.1 nm, tilted by 12° $\pm$ 2° with respect to the high symmetry axes of the underlying Ag(111) substrate. The bright features can be associated with the phenol groups within the molecule. The green dumbbells represent single molecules in the clockwise rotating windmill motif. The rotation of the motif can be observed in both directions. Figure 3.6 (b) shows a counter clockwise windmill motif of the same molecular configuration as in (a) (blue dumbbell mark the molecules in the STM image). The lateral unit cell (4.0 $\pm$ 0.1 nm) is the same as in figure 3.6 (a), but it is a tilted by -15° $\pm$ 2° with respect to the high symmetry axes of the underlying substrate. Even though we can not distinguish molecular enantiomers in the windmill motif, this images show that the prochiral precursor builds assemblies exhibiting organizational chirality [51–54].

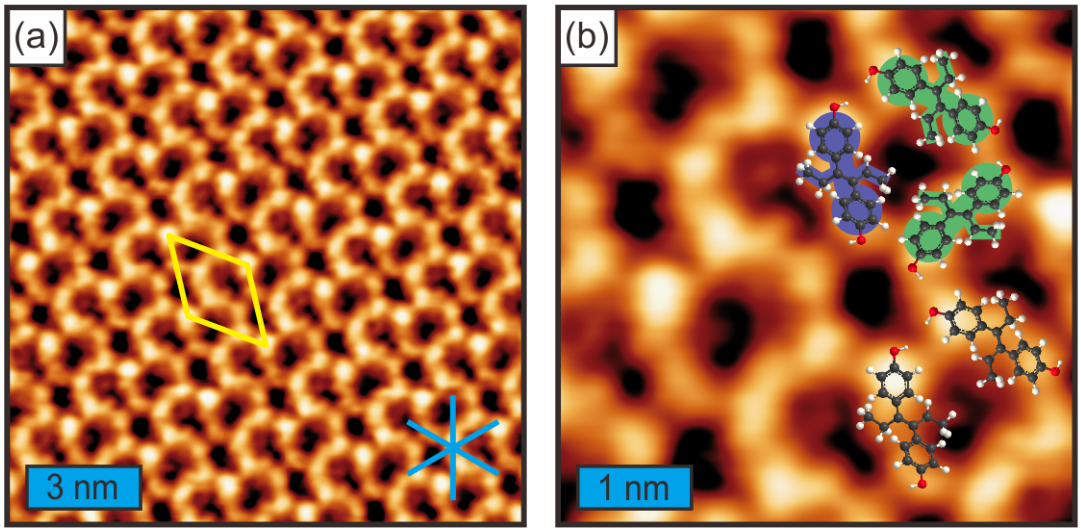

Figure 3.7: Shingle structure of DES on Ag(111) at room temperature. (a) High resolution STM image of shingle motif with unit cell. The high symmetric axes are marked in blue. (b) Detail image of shingle motif with superimposed molecules. The different surface enantiomers are marked with blue and green symbols (U_b = 1.49 V, I_t = 0.10 nA, image recorded at 290 K).

Shingle motif The second, predominant structure observed at RT, which is coexisting with the windmill structure on the surface, is addressed here as the 'shingle motif'. The shingle motif looks like a porous network with bright protrusions and two different types of pores (Figure 3.7 (a)). The unit cell side length was measures to be 2.0 $\pm$ 0.1 nm and the angle of 53°. The unit cell is tilted

by -13° ± 1° with respect to the Ag [01$\bar{1}$] surface direction. As this structure is coexistent with the windmill motif and the molecules appear as similar protrusions in the STM images, a similar molecular orientation is proposed. The repeating unit of the structure consists of three molecules which are stabilized by circular hydrogen bonding between the alcohol groups of the molecules. In the detail image (Figure 3.7 (b)) we can verify the ethyl groups within the pores. Therefore we can distinguish the different surface enantiomers of the molecules as marked in a blue and green on the superimposed molecular models. Binding to the surface can again occur via interaction of the π systems of the phenol groups and the OH groups. The phenol group interacts with the next molecule via H-bonds. The ratio between the two surface enantiomers in this structure seems to be 2:1.

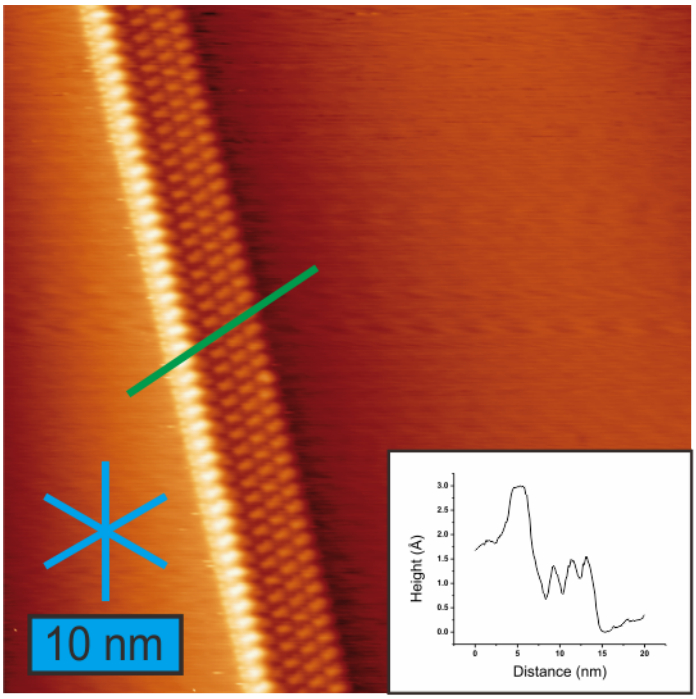

Figure 3.8: Molecular assembly on the surface with few molecules remaining at the step edges after annealing to 370 K. (U_b = 1.25 V, I_t = 0.14 nA, image recorded at 160 K). The blue star indicates the Ag(111) high symmetry axes. The line profile shows a step edge and the intermolecular distances.

High annealing temperature To understand how the structure depends on the annealing temperature, we annealed the adsorbed molecules at 330 K and recorded them afterwards at about 160 K. The STM results reveal the windmill structure but we can not observed the shingle motif after annealing. This can be an effect of the reduced coverage, since some of the molecules desorbed from the surface during annealing. The shingle structure has a higher molecular density

and might only occur at high coverages to accommodate more molecules on the surface. After annealing the sample to 370 K, we observed molecules only close to the step edges in ordered in rows. The structure may consist of three or four molecules aligned by H-bonds. According to the XPS results, the hydroxyl groups start to deprotonate at this temperature but are mainly intact. The line profile shows a distance between two protrusions with approximately 1.2 nm distance and we can identify a molecule onto of the step edge. Thus we assume one protrusion in the network to be one molecule in *trans*-conformation. Annealing the surface to 420 K leads to a complete loss of the molecules from the surface.

3.1.2 DES on Cu(111)

XPS In the following we measured DES absorbed on Cu(111) to evaluate the chemical state of the molecule after different annealing steps. The O 1s and C 1s spectra for the different temperatures are shown in figure 3.9 (a) and (b).

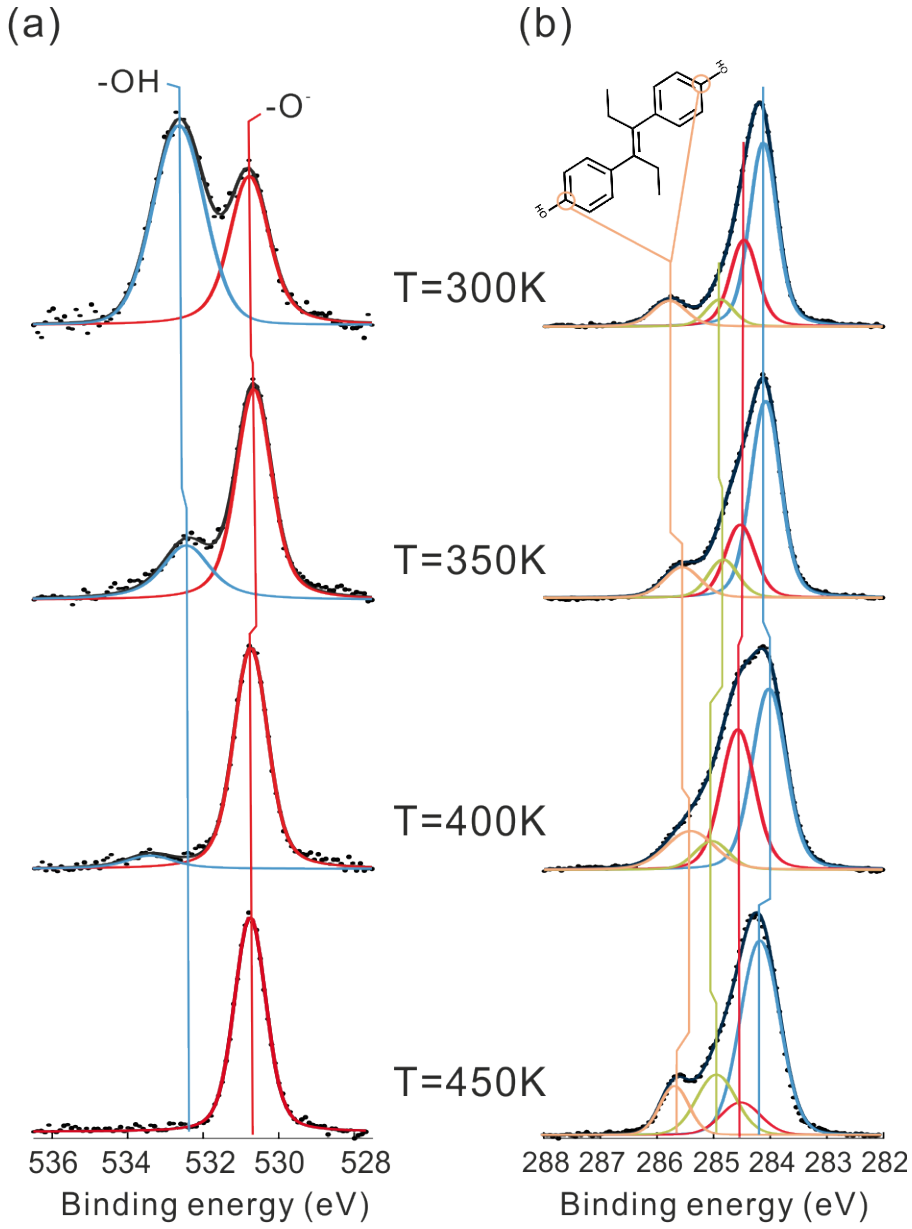

Figure 3.9: The O 1s and C 1s XP spectra of DES on Cu(111) after different annealing temperatures. (a) O1s spectra (b) high resolusion C1s spectra. This spectra were recorded at 200 K.

The XP spectroscopy reveals that the molecule's OH-groups get partially deprotonated directly

after dosing molecule on the surface at room temperature. The O 1s spectra Figure 3.9 (a) shows two peaks, which can be assigned -OH at 530.8 eV and -O^- at 532.7 eV. After annealing the sample to 350 K, the -OH peak intensity (530.7 eV) is definitely decreased whereas the -O^- peak (532.5 eV) is increased. Both peaks were shifted by approximately -0.15 eV. The ratio between protonated and deprotonated hydroxyl groups was increased after annealing to 350 K from 1.3:1 to 1:4. Further annealing to above 400 K leads to an almost complete loss of the hydroxyl groups protons. The ratio of the peaks is about 1:10. After warming up the sample to 450 K, the hydroxyl group is completly deprotonated. The C 1s spectra as shown in figure 3.9 (b) are fitted with four peaks. The peak at 285.8 eV can be assigned to C10 and C16 which represent their carbons connected to the alcohol groups. However, the rest of the features of the C 1s spectra can not be assigned unambiguously and perhaps XPS simulations could clarify this point. Nevertheless, the spectra shows a distinct sensitivity to the thermally induced molecular changes (see Table 3.1.2).

T_{ann} (K)	Carbon		Oxygen	
	E_b (eV)	FWHM	E_b (eV)	FWHM
300	285.8	0.6	532.8	1.3
	284.9	0.5	530.9	1.0
	284.5	0.5		
	284.2	0.5		
350	286.6	0.7	532.7	1.5
	284.8	0.6	530.7	1.1
	284.6	0.6		
	284.1	0.6		
400	285.4	1.0	533.4	1.5
	285.1	0.7	530.8	1.0
	284.6	0.7		
	286.0	0.7		
450	286.0	0.8	530.8	1.0
	284.9	0.8		
	284.9	0.5		
	284.5	0.6		

Table 3.1.2: XPS results: Binding energy and FWHM after annealing steps from 300 K to 450 K for the C 1s and O 1s spectra.

Stripe motif On metal surfaces as Ag(111) and Cu(111), the DES molecules have only weak molecule - molecule and molecule - substrate interactions. Therefore the DES molecules are very

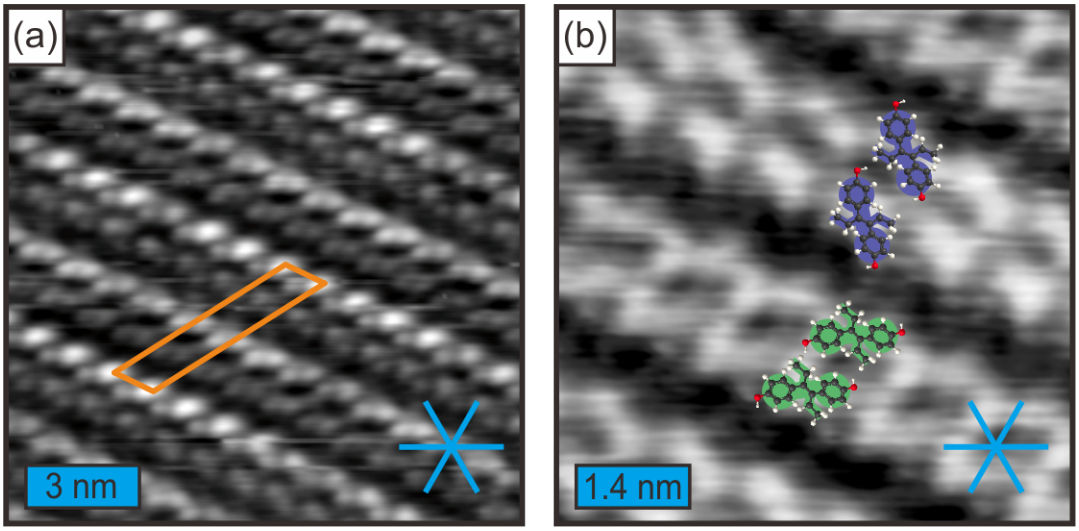

Figure 3.10: Stripe motif on Cu(111) recorded at 170 K after annealing to 350 K. (a) The alternating apparent height of the rows is clearly visible (U_b = 2.66 V, I_t = 0.16 nA). (b) The enantiomers buildung the stripe structure superimposed on the image are marked in green and blue (U_b = 1.48 V, I_t = 0.11 nA).

mobile on the surface at RT. Thus, we performed STM studies at low temperatures to reduce the mobility of the molecules during the experiments.

After depositing the molecules at room temperature, we observed a molecular network which will be addressed as 'stripe motif' shown in figure 3.10. The motif is built of paired protrusions that are arranged in parallel rows which are tilted by 30° against the high symmetry axes of the substrate. As the distance between each two connected protrusions is about 4 ± 1 Å, they are supposed to represent one molecule. These molecules are aligned along the symmetry axes of the surface. Two rows with different apparent height are always closer together. This leads to an alternating pattern of high and low apparent height rows. The single molecules in the lower apparent height row seem also to change their orientation by 60°. This leads to a unit cell of 4.2 ± 0.1 nm by 1.0 ± 0.1 nm with an angle of 120°. The alternating apparent heights could have different origins: It could be induced by different adsorption sites of the molecules on the Cu(111) surface but also by a different molecular orientation or isomerisation with respect to the surface. However the molecular conformation can not be clearly distinguished. It might be *cis*- or *trans* configuration. A structural model including both enatiomers is superimposed on Figure 3.10 (b) (green and blue). Basically the molecular conformation is the same as on the silver surface (see figure 3.7). The structure shows two different adsorption geometries tilted by 60° between the stripes. We assume that the central lobe in the STM images is the molecular backbone and small protrusions at the sides are the ethyl groups of the molecule.

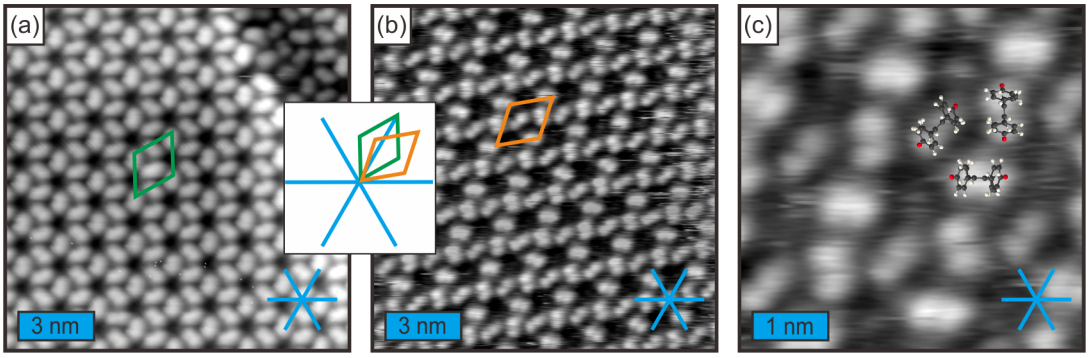

Figure 3.11: STM images of stars motif (a) large island of the star motif with a step edge after annealing to 400 K. The unit cell axis is rotated by 30° ± 2° with respect to the surface high symmetry orientation (U_b = 1.44 V, I_t = 0.14 nA, image recorded at 185 K). (b) Star motif recorded at room temperature with a unit cell rotated by 8 ± 2° with respect to the surface axes (U_b = 0.59 V, I_t = 0.12 nA, image recorded at 290 K). (c) Detail image of star motif with a superimposed molecular model of molecules in *cis*-conformation.

Star motifs The predominant two dimensional nanostructure we observed, coexisting with the stripe motif from room temperature to 400 K, is shown in figure 3.11. The structure is addressed as 'star motif' and covers very well ordered large areas of the surface. Analysing the unit cell of this pattern, one realizes that there are two different star patterns. Where the side length for both hexagonal unit cells is always about 1.6 ± 0.1 nm, their tilt angle against the high symmetry axes differs significantly: In one case (a) it is 30 ± 2° in the other (b) it measured to be angle about 8 ± 2°.

Although the measured unit cells of (a) and (b) seem to be incommensurate to the surface, we did not observe a moiré pattern. Figure 3.11 (c) shows a detail image with superimposed molecular models. One protrusion represents a single molecule, thus the star motif consists of three molecules. The molecule is assumed to be in *cis*-configuration on the surface with the deprotonated hydroxyl groups interacting with the substrate atoms. This can be supported by images where the stars motif fades into a disordered arrangement of these elongated protrusions, which would be unlikely if the substructure accounted for more than one molecule. The structure is not affected by the temperature or scanning conditions. However after annealing to 400 K, the molecular structure was changed to the dense packed one shown in figure 3.12.

Changed star motif Figure 3.12 (a) shows two different molecular patterns marked with orange and yellow arrows emerging after annealing to 400 K. The orange arrow marks the star motif as observed before but the yellow arrow points to a different molecular pattern which is addressed as changed star pattern. The changed star pattern was observed very rarely in separated island on the surface already after annealing to 350 K. The detail image Figure 3.12 (b) shows the two

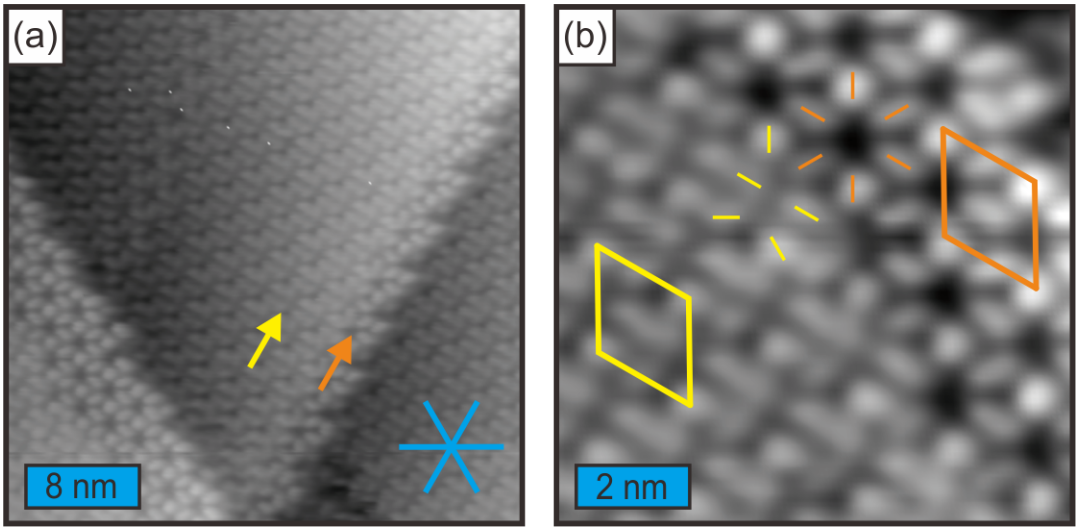

Figure 3.12: STM images of (a) star pattern (marked by orange arrow) and the changed star pattern (marked by yellow arrow) after annealing to 400 K at recorded ∼188 K. (b) Detail image of phase boundary from star to changed star pattern with the same unit cell. Single molecules are marked with a yellow and an orange bar. The high symmetry axes of the substrate are indicated in blue (U_b = 1.4 V, I_t = 0.14 nA).

star patterns. Both unit cells are about 1.6 ± 0.1 nm. The small lines in the image mark single molecules within the star and the changed star pattern. The changed star pattern is similar to the star motif with the difference that there seems to be an additional central molecule in the unit cell which contains now four molecules.

Chains While the before described motifs are visible for a wide range of annealing temperatures up to 400 K, annealing at higher temperatures leads to a loss of the molecules (see figure 3.13a). At the same time we observe the formation of molecular chainlike threads on the surface. XPS data show that at this temperature all hydroxyl groups loose their protons and high resolution images show that single protrusions are still distinguishable (figure 3.13 (b)). The fact that the chains extend also over step edges, makes a polymerization reaction scenario reasonable. A possible polymerization reaction is the loss of one oxygen per molecule and the formation of a new bond. The high temperature stability of this phase is also a hint to a more robust molecular binding, such as covalent bonds.

Molecular model on Cu(111) On the basis of the results we can propose a molecular model for DES on the Cu(111) surface. The DES molecules in *cis*-conformation with the oxygen atoms pointing towards the surface fit quite well to the STM data. This suggests an increased affinity of the oxygen atoms towards the copper. As the XPS data suggest a high degree of deprotonation of

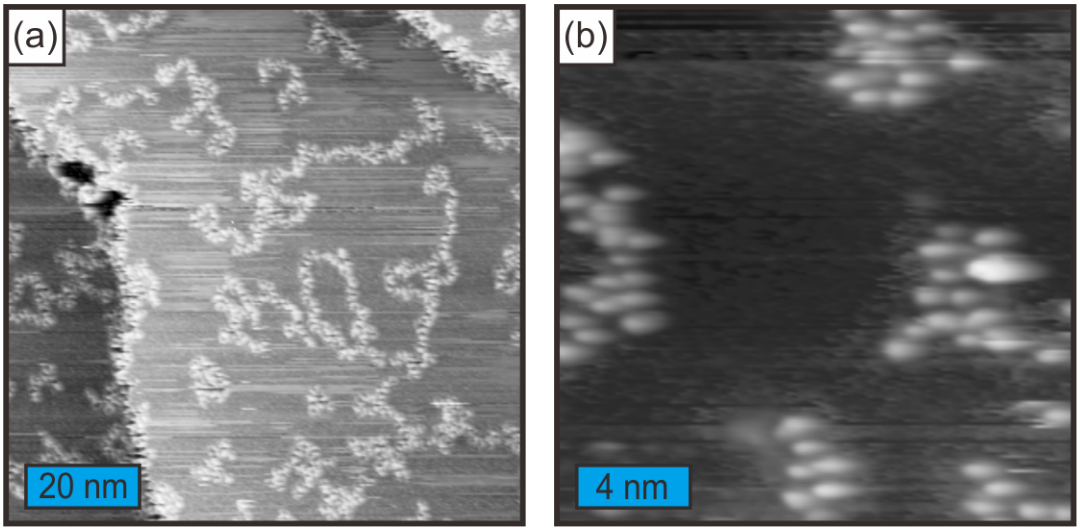

Figure 3.13: Chainlike motif after annealing to 450 K (a) overview of the chain structures recorded at 290 K (U_b = 1.25 V, I_t = 0.17 nA). (b) Detail image of chain motif reveals bright protrusions recorded ∼185 K (U_b = 1.25 V, I_t = 0.19 nA).

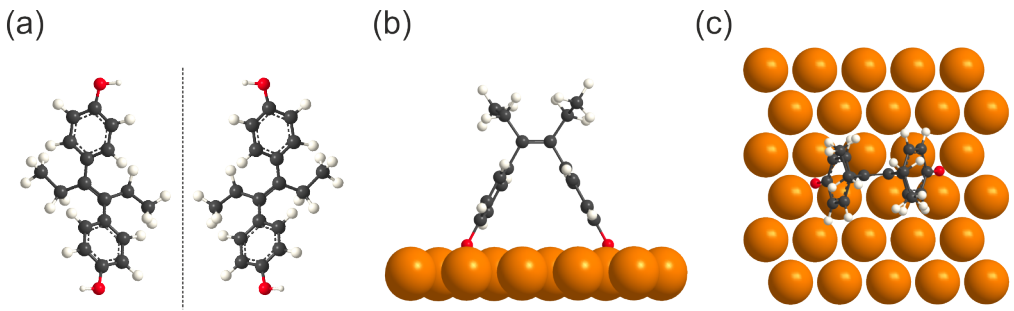

Figure 3.14: Molecular model of DES in *cis-trans* isomerization on the Cu(111) surface. (a) *trans*-isomer (b),(c) *cis*-configuration obtained by DFT geometry optimization [45].

the hydroxyl groups, a model with both hydroxyls deprotonated is proposed. The DFT-calculations with a single DES molecule on a single Cu(111) layer confirmed that the adsorption geometry shown in figure 3.14 is indeed a local energetic minimum [45]. The calculated bond distance of 1.9 Å between copper and oxygen is in accordance with the literature [55, 56]. These considerations lead to the tentative molecular model presented in figure 3.11 (c). The lowest energy adsorption sites of the oxygen atoms in the DFT simulation are the hollow positions of the Cu(111) surface. As the stripes motif is coexistent with the stars motif and the distances between two protrusions are similar to the ones in the star motif, the same molecular orientation is proposed.

3.1.3 Conclusion

On the Ag(111) surface, the X-ray spectroscopy results show that the hydroxyl groups are partially deprotonated. NEXAFS indicates an average tilt angle of the phenyl rings of $\sim 50^{\circ}$ with respect to the surface. The STM results show enantiopure windmill structures and a shingle motif, which is build by both *trans* enatiomeres. After annealing the sample to 420 K, the molecules desorb from the surface. At the Ag(111) surface, the DES molecules seem to be present only in the *trans*-configuration.

On the Cu(111) surface, according to the X-ray spectroscopy, the DES deprotonates directly after deposition at room temperature. STM analysis suggests both *cis*- and *trans*-configuration to be present in the found molecular assemblies. The predominant molecular configuration is the *cis*-configuration with deprotonated alcohol groups interacting strongly with the surface atoms.

3.2 *meso*-tetraphenylporphyrin on Ag(111)

Porphyrin derivatives are widely used in low dimensional nanostructures because of their unique biological functionalities [57–66]. Porphyrin molecules can produce a variety of molecular assemblies on metal surfaces steered by the substituent groups such as 2H-porphins (2H-P), *meso*-tetraphenylporphryins (2H-TPP), tetrapyridyl-porphyrins (TPyP), and metalloporphyrins. There are mainly three strategies to produce a wide variety of metalloporphyrins in situ: (1) direct deposition of metal adatoms on preassembled porphyrin layer. [61, 63, 67–74]. (2) Coordination to pre-deposited adatoms [72, 75–77]. (3) Self-metalation with strongly interacting substrate atoms [78–82]. Three such examples are shown in Figure 3.15. The macrocycle of the 2H-porphyrin shown in Figure 3.15 (a) contains two hydrogen atoms bonded to the central nitrogens. The bright protrusions after annealing the molecule on a Cu surface to 423 K are caused by an electronic effect and reveal a self-metalation with a substrate atom [81, 83]. Figure 3.15 (b) shows a 2H-tetraphenylporphyrin which adopts a saddle-shape on metal surfaces. The STM image shows four protrusions which are the phenyl substituents of the 2H-TPP (Figures 3.15b, 3.17c). Figure 3.15 (b) (right) shows metalation after coevaporation of Fe. The Co-tetraphenylporphyrin in Figure 3.15 (c) shows three bright lobes in the center. After exposing the layer to CO molecules from gas phase, the center appearence changes because the CO molecules bind as axial ligands.

Here we study metal-organic coordination and coupling of organic molecules on a Ag(111) surface with a combination of STM and X-ray spectroscopy. The employed molecules are *meso*-tetraphenylporphyrin and the metalation precursor $Ru_3(CO)_{12}$. The 2H-TPP molecules on the Ag(111) surface undergo an intramolecular cyclodehydrogenations when heated to 550 K [85]. At this high temperature, two hydrogens in the structure can form a H_2 molecule and leave a newly formed C-C bond between a substituent phenyl ring and the porphyrin macrocycle. Four cyclodehydrogenation products (**3** to **6** in figure 3.16) can be expected after annealing.

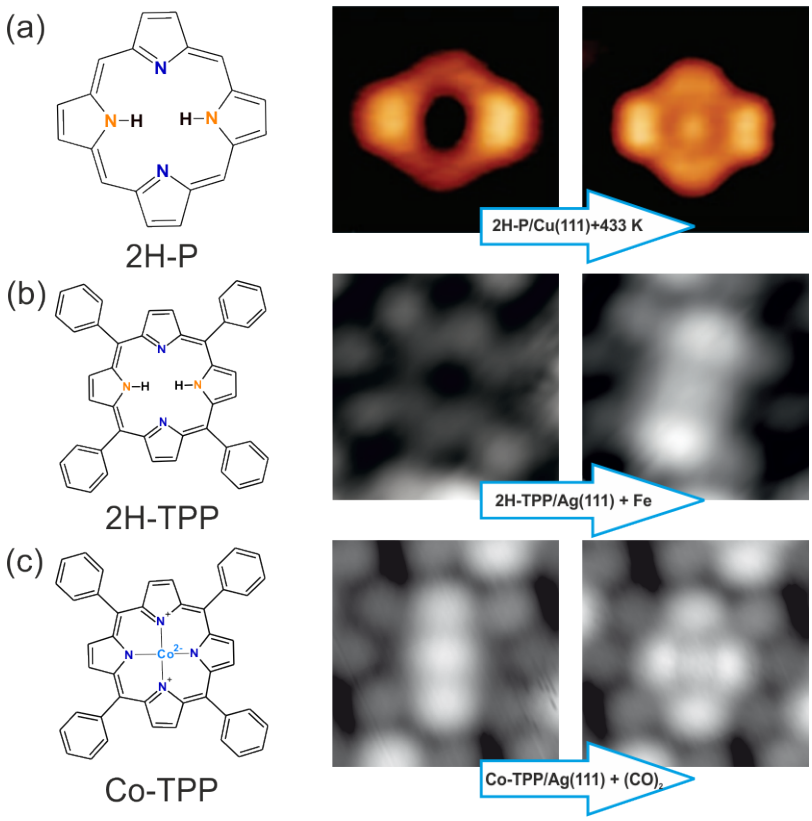

Figure 3.15: Chemical structure of porphine and porphyrin derivatives with STM images. (a) 2H-Porphine structure and according STM images before and after self-metalation with a substrate Cu atom. (b) 2H-tetraphenylporphyrin (center: U_b = -0.2 V, I_t = 0.08 nA) before and after Fe metalation by direct deposition. (right: U_b = -0.2 V, I_t = 8.3 nA) [61] (c) Co-tetraphenylporphyrin (center: U_b = -0.24 V, I_t = -0.35 nA) before and after addition of two axial CO ligands. (right: U_b = -0.6 V, I_t = 0.1 nA) [84].

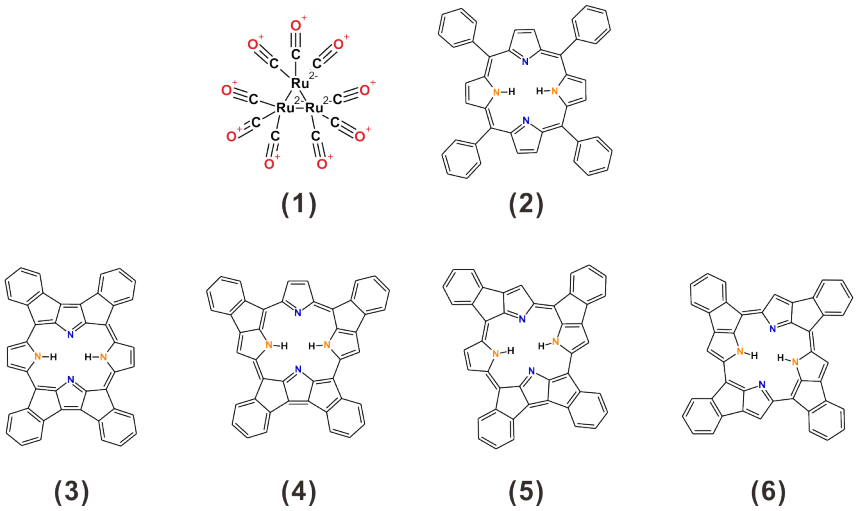

Figure 3.16: Molecular models: (1) metal precursor $Ru_3(CO)_{12}$. (2) The 2H-tetraphenylporphyrin (2H-TPP). The (3)-(6) flat 2H-TPP molecules formed by cyclodehydrogenation on Ag(111) at high annealing temperatures. Aminic and iminic sites of the porphyrin macrocycle are indicated in blue and orange, respectively.

3.2.1 Flat conformation

After dosing a multilayer of 2H-TPP molecules at room temperature, we annealed the sample above 540 K in order to desorb the second layer and to produce a closed packed structure as shown in Figure 3.17a. Due to π interaction of the phenyl rings, the molecules order well along the surface high symmetrie orientations. This interaction was reported as "T type" interaction [86]. There are four protrusions in a single molecule clearly discernible, which correspond to the phenyl rings. Due to a rotation of the phenyl rings, the 2H-TPP molecules adopt a saddle shape on the metal surface [86–88]. In order to promote dehydrogenation, we annealed the sample to 570 K. Figure 3.17 (b) shows a flat phenyl conformation of 2H-TPP molecules formed by cyclodehydrogenation superimposed with models of the molecules. The molecules seem to be oriented along the surface high symmetry axes. Due to the annealing, the molecular coverage is decreased from multilayer to a submonolayer coverage [28]. The molecular density of the non-flat porphyrin in saddle conformation molecule is about 0.37 nm^{-2}. The density of the flat phenyl porphyrins is about 0.30 nm^{-2}. This means that the molecular density is decreased by 19% by the annealing step.

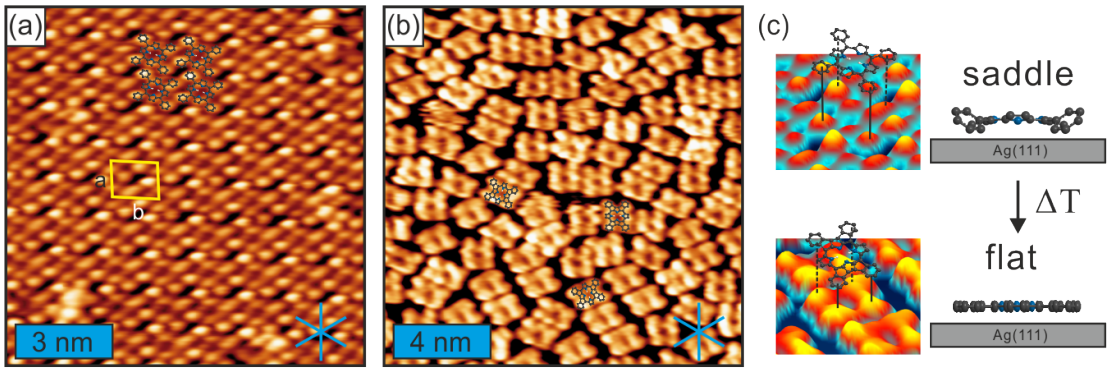

Figure 3.17: Non-flat and flat 2H-TPP conformation on Ag(111). (a) Non-flat 2H-TPP in saddle conformation with attractive intermolecular interaction on the surface. The bright lobes are the four phenyl rings. Molecular models are superimposed on the STM image. The square unit cell marked yellow is approximately a = b = 1.4 mm. Image recorded at 123 K after annealing to 540 K (U_b = -0.61 V, I_t = 0.08 nA). (b) Flat 2H-TPP molecules formed by cyclodehydrogenation with superimposed molecules which are aligned with respect to the surface high symmetry axes. Image recorded at 93 K after annealing to 570 K (U_b = 1.25 V, I_t = 0.12 nA). (c) Ball and stick structure with side view: the top shows a saddle shape which reveals a tilted phenyl ring, bottom shows a flat conformation. The saddle shape can be changed to a flat conformation by annealing to 550 K [89].

The 2H-TPP orientation depends on the molecule - molecule and molecule - substrate interactions. The random distribution of the flat molecules on the surface does not indicate any attractive interaction between the molecules [83]. Figure 3.17 (c) shows 3D models and side views of the

molecular structures on the surface (see Figure 3.19). The STM images (a) and (b) in figure 3.17 show both structures which are formed by the saddle and flat conformation. Figure 3.17 (c) shows the structure the porphyrin in saddle confomation expected to be present in figure 3.17 (a). After annealing the sample to 550 K (Figure 3.17 (c) at the bottom) the molecules adopt a flat conformation.

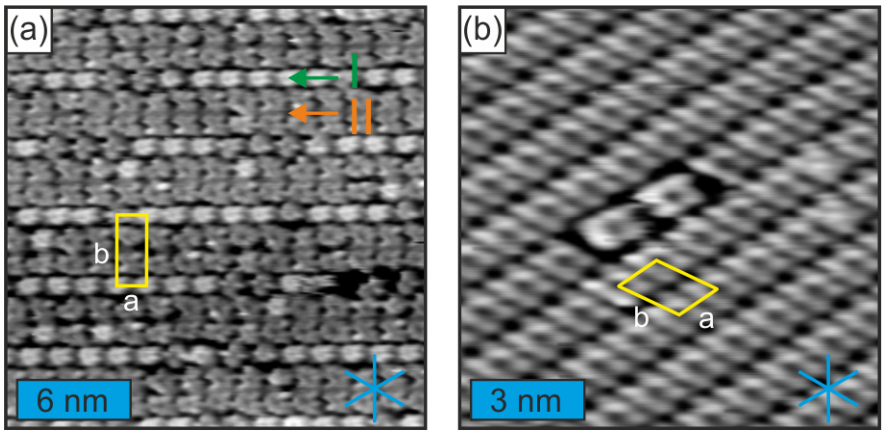

Figure 3.18: Two rows assembly and diffusing single molecules in the between network. (a) Two row pattern where (I) is a single row structure and (II) is a double row structure. The two row pattern reveals a different interaction between the molecules. The rectangular unit cell is approximately a = 1.5 nm, b = 3.6 nm. Image recorded at 123 K after annealing to 540 K (U_b = 1.25 V, I_t = 0.12 nA). (b) Close packed assembly with two single molecules diffusing in a triple vacancy. The rhombic unit cell is approximately a = 1.2 nm, b = 1.8 nm with an angle of 120°. Image recorded at 133 K after annealing to 560 K (U_b = -1.05 V, I_t = -0.05 nA).

The assembly of porphryin molecules can be influenced by the annealing temperature [86, 89–91]. Despite the random ordered assembly shown in figure 3.17 (b) we observed additional two close packed arrangements at different annealing temperatures. There are two patterns of the molecules observed in the assembly shown in Figure 3.18 (a). One is a row of molecules in saddle shape (I) and (II) which are flattened molecules in a double row measured after annealing the sample to 540 K. This characteristic pattern evolves in the range of 540 - 570 K and shows a mix of flattened and non-flattened molecules. After annealing sample to 570 K, we observed mainly mobile molecules due to the weak interaction between 2H-TPP and the substrate. To immobilize the molecules, we tried to increase the coverage by subsequently depositing and annealing. Figure 3.18 (b) shows a dense packed molecular structure of flattened porphyrins with a rhombic unit cell with approximately a = 1.5 nm b = 3.6 nm. However we found mobile molecules in the molecular networks. The two molecules in figure 3.18 (b) are rotated 60° with respect to the molecular network. We can confirm that the close packed molecules are compound **3**. But the rotated ones look different and there might be the other compounds **4, 5** or **6** which therefore do not fit into the

close packed structure.

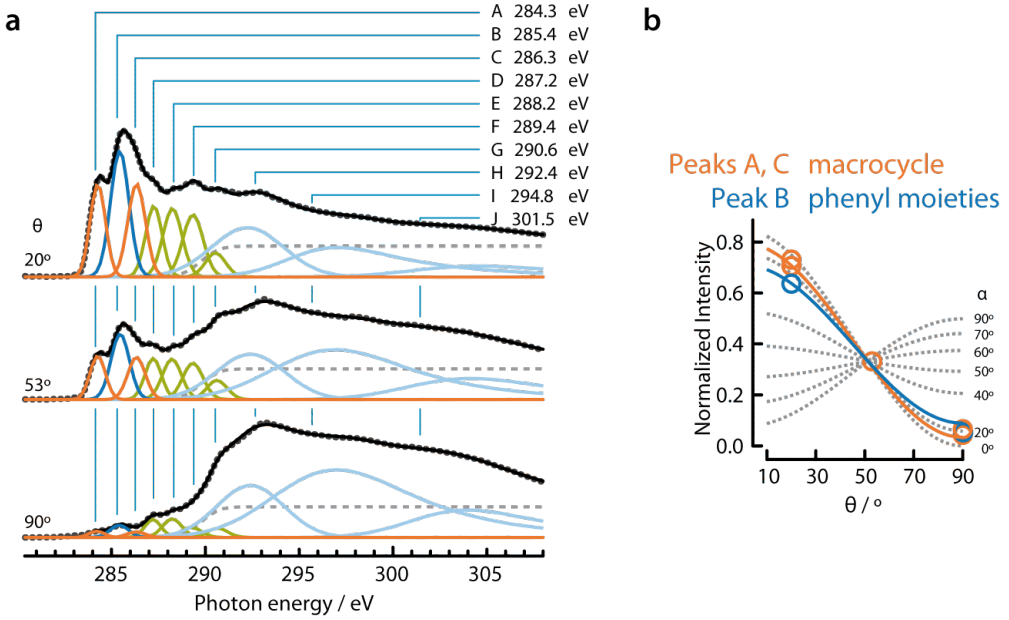

Figure 3.19: NEXAFS results of cyclodehydrogenated 2H-TTP. (a) Normalized C K-edge at three different photon incident angles θ fitted with gaussians according to the binding energies. (b) Curve-fitting analysis of π^* resonances A, C, and B to estimate the tilt angles of the macrocycle and the phenyl moieties of the molecule, respectively [28]

The NEXAFS results are shown in Figure 3.19 (a) along with the curve-fitting analysis according to the photon energy as shown in table 3.2.1. The angular dependence of normal, magic, and grazing incidence of the phenyl moieties of the molecule indicate a significantly reduced angle with respect to the surface plane. Therefore, we conclude that the 2H-TPP exhibits a flat conformation on the metal surface as introduced by Di Santo [85]. The photon energy of 284.3 eV and 286.3 eV are assigned to macrocycle porphyrin and the peak at 285.4 eV is assigned to the phenyl ring. The π^* resonances are named from A to G and the σ^* resonances from H to J. Figure 3.19b shows the analysis of the angular dependence. We fitted only the macrocycle porphyrin and phenyl moieties which suggest an angle of about 20 ± 10 ° by comparison with theoretical angle dependencies. Thus, according to the STM and NEXAFS results, the molecules formed a flat conformation after annealing at around 550 K.

Peak	Photon energy/eV	Assignment	
A	284.3	C 1s $\rightarrow \pi^*$	macrocycle
B	285.4	C 1s $\rightarrow \pi^*$	phenyl
C	286.3	C 1s $\rightarrow \pi^*$	macrocycle
D	287.3	C 1s $\rightarrow \pi^*$	
E	288.3	C 1s $\rightarrow \pi^*$	
F	289.4	C 1s $\rightarrow \pi^*$	
G	290.5	C 1s $\rightarrow \pi^*$	
H	292.1	C 1s $\rightarrow \sigma^*$	
I	294.8	C 1s $\rightarrow \sigma^*$	
J	301.5	C 1s $\rightarrow \sigma^*$	

Table 3.2.1: Peak assignment for the C K-Edge NEXAFS peaks of the cyclodehydrogenated porphyrin monolayer on Ag(111) [28].

3.2.2 Ru metalated 2H-TPP

After establishing a recipe to flatten the porphyrins, we dosed the metal precursor $Ru_3(CO)_{12}$ at room temperature on top of the assemblies. We found metalated molecules after annealing the sample to 550 K as shown in Figure 3.20a. The central bright protrusion on the single molecules represent metal atoms incorporated into the flattened porphyrin. The percentage of metalation after the first exposure at 1.5 x 10^{-8} mbar for 34 min is about 38 %. At the given voltage, the STM was probing the occupied states of the porphyrin layer. Subsequently the preparation was again exposed to the metal precurser at 8.0 x 10^{-9} mbar for 45 min and annealed to 550 K. The percentage of metalated molecules increased significantly from 38% to 68%. The 3D images in Figure 3.20c clearly show a molecule with a cavity and a metalated porphyrin. In the line profile of the apparent height both molecules are easily distinguishable. The apparent height of the center of the metalated molecule is approximately 1.6 Å.

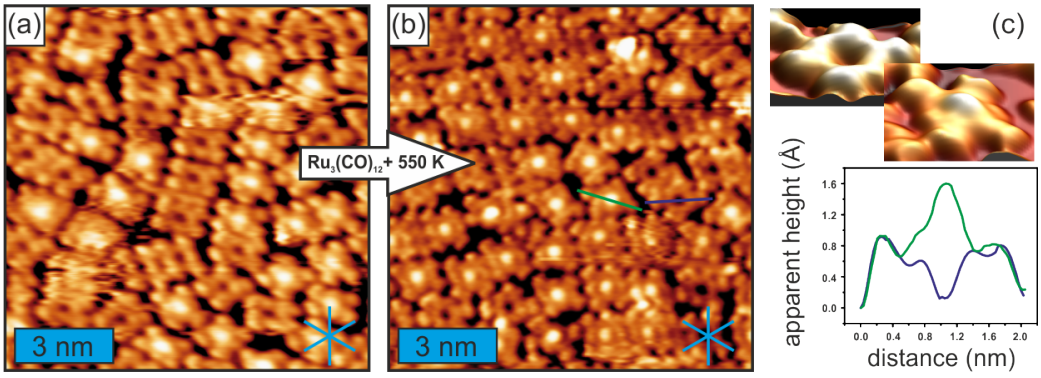

Figure 3.20: Metalation of flattened 2H-TPP: (a) STM image of the 2H-TPP after exposing to the metal precursor and annealing to 550 K. The percentage of metalated molecules is about 38%. The image was recorded at 103 K (U_b = -1.13 V, I_t = -0.38 nA). (b) After a second exposure to the precursor and annealing to 550 K, almost 68% of the molecules are metalated. The image recorded at 163 K (U_b = -0.99 V, I_t = -0.027 nA). (c) Line profile of the flat 2H-TPP and the metalated one with a 3D model.

Figure 3.21 shows four single metalated flattened porphyrin molecules numbered according to their specified the species in figure 3.16. Before the metal precursor was dosed, we observed a predominant structure formed by molecule **3** on the surface. However, we observed sometimes the three other molecular conformations (**4** to **6**) of the metalates molecules.

To understand the chemical state of the molecules, we measured the C 1s, N 1s, Ru $3d_{5/3}$, and O 1s binding energy regions with XPS. The C 1s is not shown since it did not reveal any relevant information. After annealing the sample to 550 K to obtain a flat conformation, we measured two equal Nitrogen peaks (N1, N2 (see figure 3.22 (a)). This did not change after exposure to the metal precursor, $Ru_3(CO)_{12}$, at room temperature (see figure 3.22 (b)) which means that there is

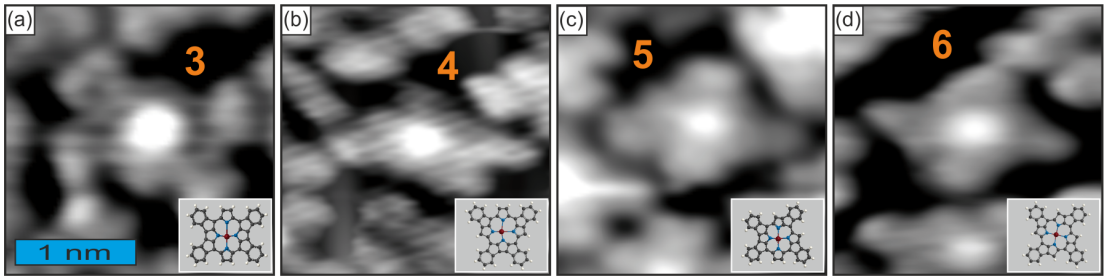

Figure 3.21: Cyclodehydrogenation of 2H-TPP molecules leads to different molecular conformations as shown in figure 3.16 numbered **3, 4, 5, 6** respectively. However the predominant metalated molecule is **3**. (a) U_b = -0.99 V, I_t = -0.25 nA, image recorded at 163 K after annealing to 550 K. (b) Two divergent position of phenyl rings after annealing to 550 K. U_b = -1.13 V, I_t = -0.09 nA. (c) Three of the phenyls are at the same side and the other one is on a different side after annealing to 550 K. U_b = -0.99 V, I_t = -0.23 nA. (d) Chiral conformation of the molecule after annealing to 500 K. U_b = -0.92 V, I_t = -0.09 nA. Images (b-d) recorded at 103 K.

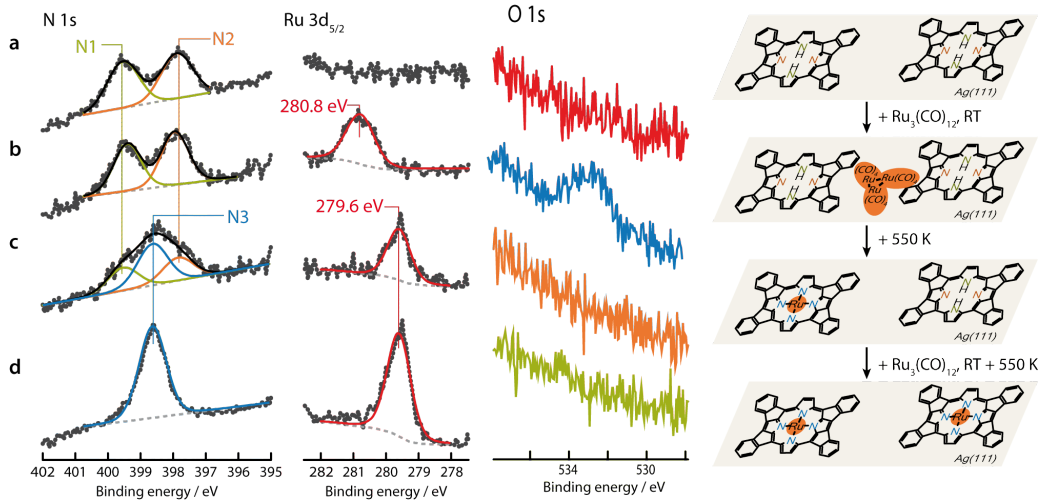

Figure 3.22: XPS results: N1s, Ru $3d_{5/3}$, and O1s spectra as well as metalation procedure with annealing temperature. After dosing and annealing the two nitrogen peaks are replaced by one. The Ru peak is gradually increasing its binding energy and intensity. The oxygen of the CO in the precursor is vanishing after annealing to 550 K.

no interaction with the metal precursors. The Ruthenium and Oxygen core levels were assigned to 280.8 eV and 533.5 eV, respectively. Both peaks, Ruthenium and oxygen, indicate that the metal precursors is present in the molecular film. After annealing the sample to 550 K (see figure 3.22 (c)), the N 1s signal is reduced to one broad peak which could be fitted with three nitrogen atoms (N1, N2, and N3). The Ruthenium component shifted its binding energy about 1.2 eV and the oxygen was gone. This is indicative of a partial metalation. In order to metalate each molecule,

we additionally exposed $Ru_3(CO)_{12}$ to the sample with subsequent annealing to 550 K (see figure 3.22 d). The N 1s signal now consists only of the N3 component with a similar increase as in the Ru $3d_{5/2}$ intensity. Thus, there is a major and relatively unexpected advantage of using the trimetal dodecacarbonyl precursor for the metalation of the porphyrin layer, as the exposure did not need to be carefully controlled in an effort to avoid the formation of additional metal species on the surface. This is in contrast to the metalation strategy which is based on the direct deposition of metals in vacuo, which requires very precise control of the metal coverage in order to provide exactly a single metal atom for each molecule present on the surface. On the basis of the XPS data of the limited ruthenium surface accumulation, we therefore tentatively propose that the Ru precursor does not directly interact with the flat porphyrin at room temperature. Instead, it adsorbs at pristine metal patches, and the heat treatment is needed to activate its decomposition and entails the subsequent porphyrin complexation.

3.2.3 Homo coupling of 2H-TPP

At high temperatures, the 2H-TPP molecule can react with its phenyl rings to form bounds with neighboring molecules similar as to the dehydrogenation observed before. For example, in the Glaser-Hay type coupling, above 330 K carbon bound hydrogens can dissociate and C-C bonds can form [92]. This reaction plays an important role in potential applications of molecular building blocks for covalently bonded nanoarchitectures [9, 93, 94]. Here we describe the homo-coupling of 2H-TPP molecules by dehydrogenation to form dimers, trimers, oligomers, and polymers.

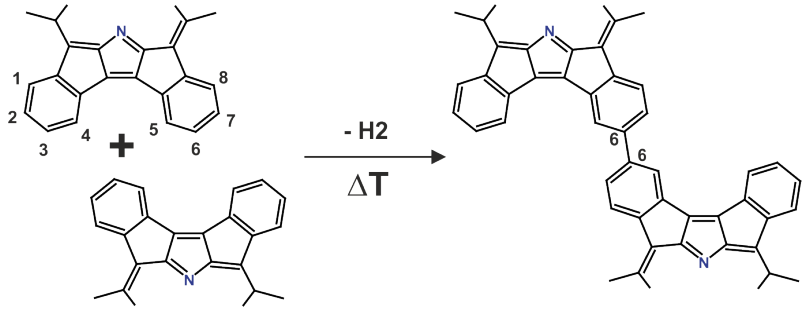

Figure 3.23: Reaction scheme of homo-coupling of 2H-TPP moieties. The coupling reaction is starting after annealing the sample to 673 K. The phenyl rings of molecules interact with other phenyl rings by forming a carbon-carbon bond.

The coupling reaction is taking place between the phenyl rings of flattened molecular moieties by dissociation of H2 molecules at high temperature (see Figure 3.23). Figure 3.23 shows the reaction with a numbering of the carbon atoms of the phenyl rings.

After annealing the sample to 673 K, we observed dimers and trimers as marked with orange circles (see figure 3.24). Figure 3.24 (a) shows flattened 2H-TPP and metalated molecules with dimer coupling motifs. The coupling motif represents a covalent molecular linkage with a neighbouring molecule. The molecular coverage is about 81%. At the bottom is a model of the dimer configuration motif which consists of two molecules rotated by an angle of about 140°. The left one is molecular conformation **4** as shown in figure 3.16 which is covalent bonded with the next molecule of conformation **3**. The binding carbons are **C3**-**C6** according to the numbering in Figure 3.23. Figure 3.24 (b) shows a trimer motif marked with an orange circle. The topographic image shows three molecules which are connected by covalent bonds. The model of the motif at the bottom indicates more complex binding configurations between neighboring molecules with two carbon atoms covalent bound. The position of two covalent bond is a dehydrogenation including carbon atoms number **4** to **6**. The angle of between the molecules is about 41°. At this temperature, most of the molecules have formed dimers and trimers but a few single molecules can still be found on surface. Figure 3.24 (c) shows a oligomer homo-coupling product after annealing the sample to 693 K. We observed that 90% molecules have interacted with neighbouring molecules

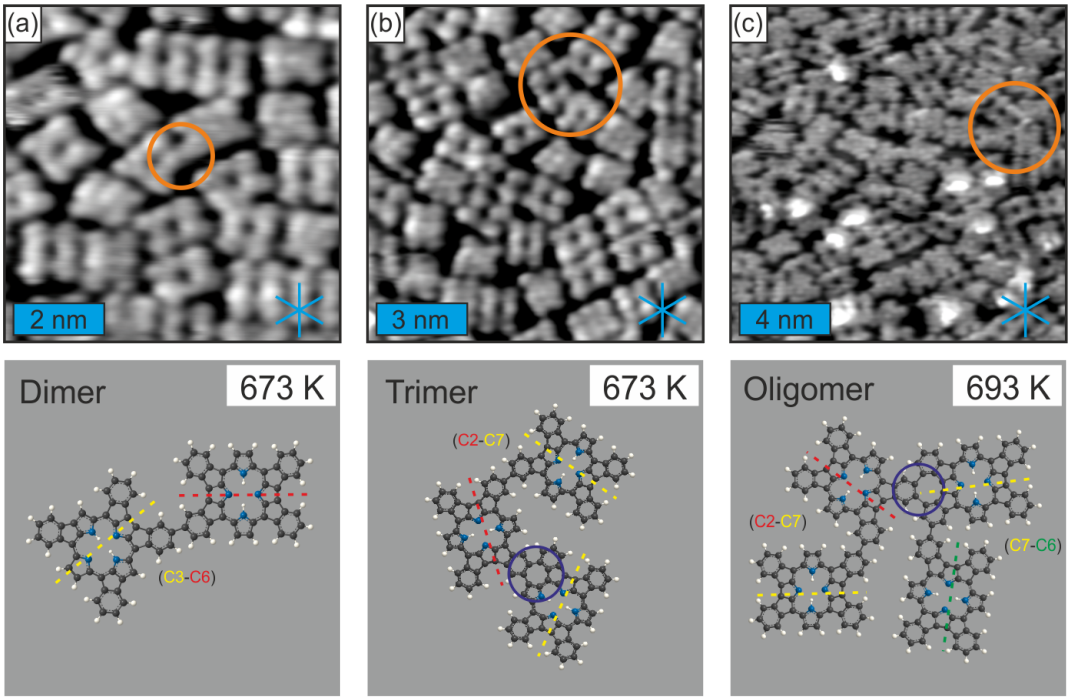

Figure 3.24: Homo coupling of flat 2H-TPP molecules. (a) At top: dimer coupling marked with a orange circle after annealing to 673 K with some metalated molecules. At bottom: model of the coupling motif of the dimer. Image obtained at 143 K (U_b = -1.63 V, I_t = -0.09 nA). (b) At top: trimer coupling marked with an orange circle. At bottom: trimer model. The blue circle marks a complex binding configuration. Image recorded at 143 K (U_b = -1.63 V, I_t = -0.07 nA). (c) At top: oligomer coupling marked with an orange circle after annealing to 693 K. Image recorded at 183 K (U_b = 1.25 V, I_t = 0.13 nA). At bottom oligomer model.

by forming covalent bonds. Some metalated molecules are still present on the surface. The metal centers are most likely Ru atoms which were left on the surface from previous experiments. The presence of the metalated molecules as well as the residual metal adatoms might influence the observed homo-coupling behaviour. The molecular coverage was about 82% which has not changed during annealing. At the bottom of the image a molecular model of the oligomer homo-coupling motif is shown as marked with a orange circle in the STM image (c).

To trigger polymerization between the 2H-TPP molecules, we annealed the sample again to 673 K (see figure 3.25a). We observed homo-coupling products, dimers and oligomers, as marked with orange and green circles, respectively. The coverage was $\sim$ 87%. The orange circle indicates a dimer homo-coupling product which was found for $\sim$ 2%. The majority of species are oligomers. After annealing the sample to 723 K, the molecular coverage was reduced to approximately 47% and we observed polymerization products (see figure 3.25b, c). Figure 3.25 (b) shows that the molecules are binding like chains together. We did not observe separated single molecules as

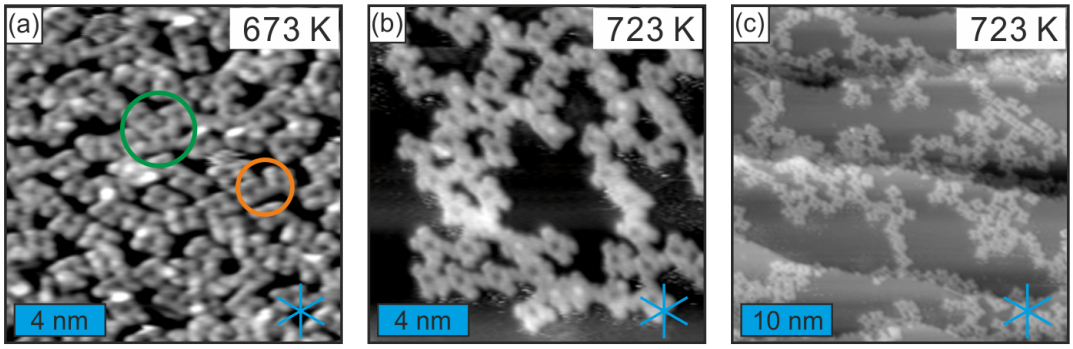

Figure 3.25: Oligomer and polymer homo-coupling products. (a) After annealing to 673 K, the molecules have formed dimers and oligomers as marked with an orange and green circle, respectively (U_b = -0.88 V, I_t = -0.11 nA). (b) After annealing to 723 K, the molecule form polymers (U_b = -1.05 V, I_t = -0.90 nA). (c) STM overview image of flat 2H-TPP layer which has undergone intermolecular coupling after annealing to 723 K (U_b = -1.05 V, I_t = -0.13 nA). All images recorded at 113 K.

well as dimer and trimer species. The figure 3.25c shows an overview image of structure. The polymerization product is widely distributed on the surface and covers the step edges.

3.2.4 Conclusion

After heat treatment, tetraphenyl-porphyrin forms a flat conformation by means of cyclodehydrogenation and consisting of four different species as shown in Figure 3.16. This products were found on the metal surface after different annealing steps from 487 K to 673 K. The predominant product is **3**, which is observed in all preparations. After exposure to a Ru-carbonyl precursor and annealing to 550 K, the molecules get metalated. The flat porphyrin on the Ag(111) surface incoorporates the Ru metal of the precursor which was monitored by X-ray spectroscopy and STM. The first evidence of metalation in the X-ray photoelectron spectroscopy was the reduction of the N1s peaks from two binding energies to one binding energy. The intensity of the Ru signal is increasing after dosing the metal precursors with subsequent annealing. The second evidence of metalation is found in the STM topographic images. Brighter lobes in the center of molecules indicate a metalation which is observed for all products **3** to **6**. By gradually annealing the sample from 673 K to 723 K, intermolecular covalent bonds evolve and we observe dimers, trimers, oligomers, and polymers, depending on the temperature.

3.3 Towards covalently bonded molecular networks by an amine - ketone reaction on Ag(111)

Regular low-dimensional molecular nanostructures on metal surfaces are often realised *via* non-covalent interactions such as H-bond, π - π stacking, van der Waals interactions, metal-ligand or dipole-dipole interactions [2, 95–103]. However these interactions generally do not meet the criteria for thermal stability required for practical applications [104, 105]. In contrast, covalently bonded networks would exhibit a high stability. However at the present stage the regularity of such polymeric nanostructures poses a great challenge to the field of molecular architectonics. Typically, there are many strategies to realize covalent architectures such as thermal dissociation of reactive side group as halogen [106–109], dehydration of borate functionalised porphyrins [110–112], imide formation mechanism by polycondensation reactions [113, 114], azide-alkyne cycloaddition [115, 116], cyclodehydrogenation [117], homo-coupling of terminal alkynes [118] and so on. The linking of functional molecules by the formation of new covalent bonds increases substantially their thermal stability and these bonds could additionally facilitate efficient electron charge transport [119]. In this sense, graphene is such a prototypical two dimensional covalent network and its physicochemical properties place it among the more interesting materials of our era, as evidenced by the 2010 physics Nobel prize award [120, 121]. This kind of molecular structures have potential applications in nanotechnology [122, 123].

Here we explore the possibility of covalently bonding molecules by an amine - ketone reaction. Basically this reaction follows the nucleophilic addition then elimination type. The nucleophilic addition of a primary amine is attacked by the partial-positive carbon of the ketone group. Then a proton is transferred from the nitrogen to the oxygen anion. An unshared pair of electrons on nitrogen migrates toward the positive oxygen, creating a water molecule. Finally a proton from the positively charged nitrogen is transferred to water, leading to the imine's formation. However, when the ketone is treated with a secondary amine, the product is an enamine as shown in scheme 3.26.

Recently, Treier and co-workers showed the polyimide formation with covalently linked structures by a condensation reaction between diamines and dianhydrides at annealing steps from 470 K to 600 K on Au(111) using LT-STM [114]. They carried out the thermally induced imidisation reactions between aromatic anhydrides and aromatic amines for the polyimide formation at monolayer coverages. However they observed two products formed by a dehydration reaction which are imide and iso-imide [113]. This reaction depends on the thermal activation of the dehydration reaction to a covalently bonded linker structure and thus would be related to this project.

Therefore we selected two compounds: 2,7 - di- tert-butyl - 4,5,9,10 - di-pyrazine - o - phenylenediamine (**PPD**) and 2,7-di-tert-butyl-pyrene-4,5,9,10-tetraone (**PT**). The **PPD** consists of a central pyrene group with two tert-butyl group at each phenyl ring and pyrazine with *o*-phenylenediamine

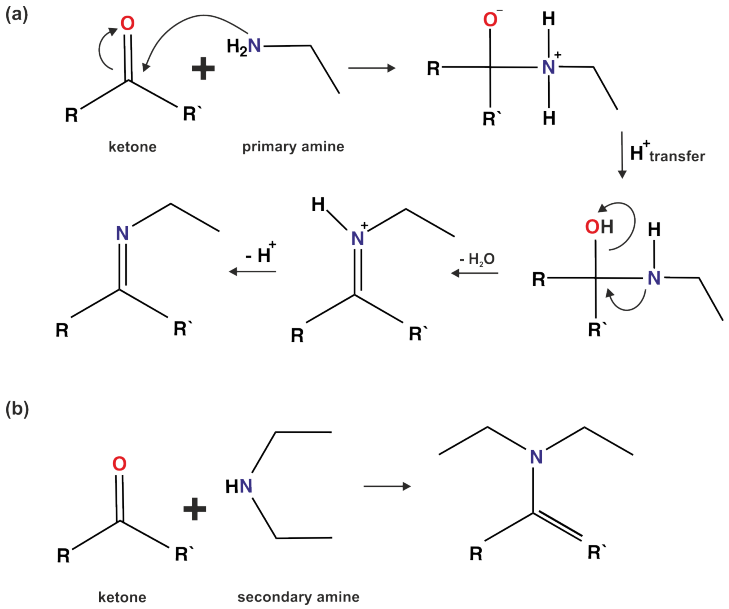

Scheme 3.26: Reaction mechanism of a ketone with a primary amine (a), secondary amine (b) forming an imine and enamine.

which is functionalised by a pair of amine groups at each side. The **PT** consists of pyrene with diketone functional group and tert-butyl groups at each side of the molecular structure. The dehydrated polycondensation is a mix of the two molecules **PT** and **PPD** formed by a ketone - amine reaction.

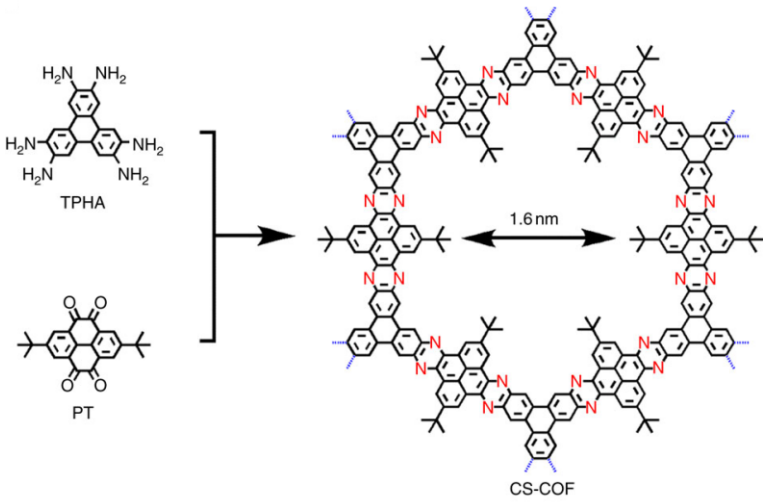

Scheme 3.27: Chemical structure of triphenylene hexamine (TPHA) and butylpyrene tetraone (PT). The two molecules build up the crystalline phenazine-linked CS-COF structure by a ketone - amine reaction. Image adopted from [124].

The monomers employed are shown in Figure 3.28. They were designed and provided by Prof. Aurelio Mateo-Alonso at the Basque Center for MACROMOLECULAR DESIGN & ENGINEERING in order to form one dimensional N-doped conducting ribbons [125, 126]. Similar monomers have been successfully polymerised to yield conjugated organic frameworks as shown in Scheme 3.27.

3.3.1 PT on Ag(111)

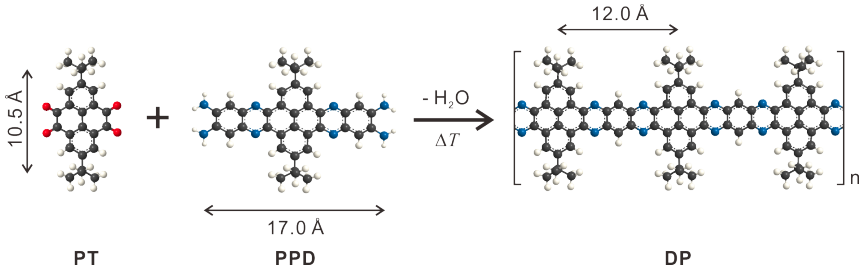

Figure 3.28: Molecular models of **PT** and **PPD**. The lengths of **PT** and **PPD** are 10.5Å and 17.0Å. The distance of the dehydrated monomers in a polymer structure of **DP** is approximately 12.0 Å between the tert-butyl groups.

PT was deposited at an atomically flat and clean Ag(111) surface kept at room temperature. Figure 3.29b shows a representative STM image of a molecular island at submonolayer coverage. The **PT** molecular structure optimized (figure 3.28) by Hyperchem [127] shows that the quaternary carbons of the molecule are separated by 10.5 Å, in good agreement with the separation of the bright protrusions in the STM image.

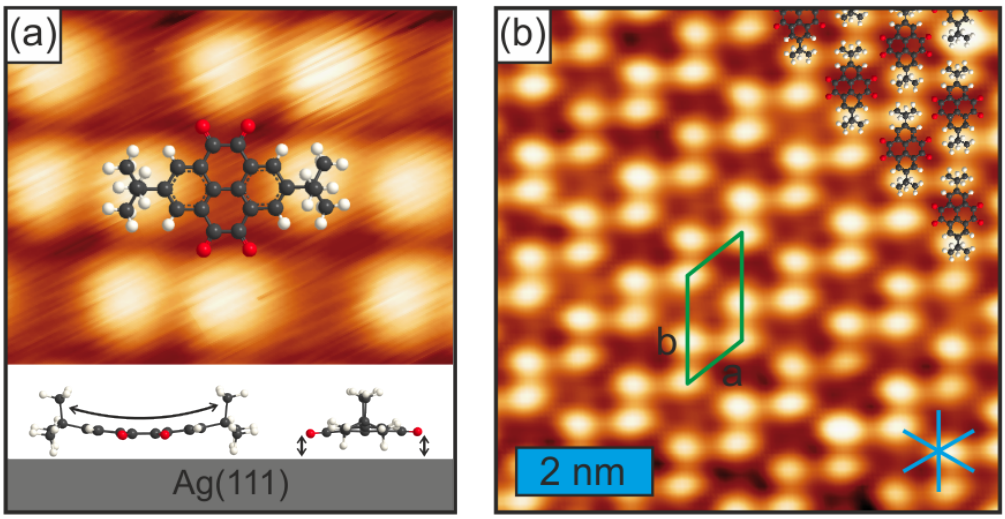

Figure 3.29: **PT** on Ag(111): (a) Top: Zoom in of STM micrograph with a single **PT** molecule in ball-and-stick representation superposed. The physically protruding tert-butyl groups are imaged as bright protrusions whereas the molecular backbone can be resolved more faintly. Bottom: Side view of proposed adsorption geometry on the Ag(111) surface. (b) STM image showing the long range two dimensional ordering (unit cell indicated in green a = 1.60 nm, b = 0.98 nm, an angle of 50°) of **PT** on Ag(111) after room temperature deposition. The Ag(111) high symmetry axes are indicated in blue. Image recorded at 123 K (U_b = 1.25 V, I_t = 0.13 nA, T = RT).

The molecular backbone of the π conjugated system is imaged more faintly in between the tert-butyl's bright protrusions. With this interpretation of the intramolecular STM resolution we can identify the molecular orientation with respect to the surface. We conclude that the π conjugated system is lying almost parallel with respect to the Ag(111) plane, as no asymmetry is evidenced in its apparent height along the Ag [$1\bar{2}1$] direction. By superposing molecular models on the STM images (Figure 3.29), we observe that neighbouring molecules have their -C=O and H-C- moieties in close proximity and therefore presume that the network is stabilised by -C=O$\cdots$H-C- attractive interactions. Additionally, we propose that the oxygen atoms are interacting more strongly with the Ag surface than the rest of the conjugated backbone and therefore might slightly bending towards the surface as shown in Figure 3.29 (a) bottom. PTCDA on Ag(111), a similar molecule, has a carboxyl group which is distorted when adsorbed on the Ag(111) surface [128, 129]. The oxygen groups are bending to the substrate atoms whereas the other atoms as anhydride and carbons were a bit raised from the surface. The molecular overlayer shows no moiré pattern, indicating that it is commensurate to the underlying Ag substrate. With this assumption and given the lateral dimensions measured by STM (the unit cell is a = 1.60 nm , b = 0.98 nm $\pm$ 0.1 nm, the angle of about 50°). We note that the π conjugated molecular backbone of the molecule is oriented along the high symmetry directions of the Ag(111). The symmetry of the surface dictates that the superstructure exists in three different orientations, as indeed observed by STM.

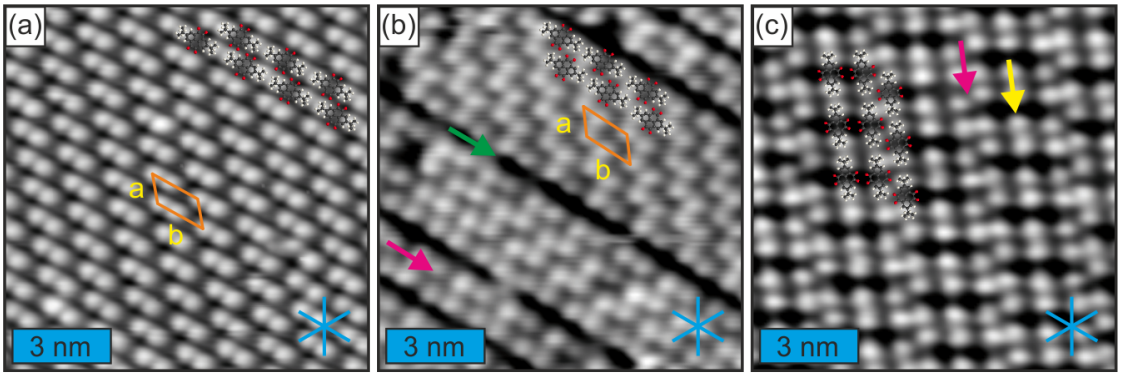

Figure 3.30: Expanding low dimensional nanostructure of **PT** on Ag(111). (a) The dense packed two dimensional structure was obtained after annealing to 370 K. (U_b = 1.25 V, I_t = 0.16 nA) Image recorded at 133 K. (b) Extended domains after annealing to 480 K. (U_b = 1.92 V, I_t = 0.23 nA, image recorded at 278 K). The unit cell of image (a) and (b) is the same (a = 1.60 nm, b = 0.98 nm $\pm$ 0.1 nm). The green arrow indicate a boundary and the pink arrow a row motif. (c) Domains consisting of one or two rows were found after annealing to 527 K. (U_b = 1.25 V, I_t = 0.11 nA, image obtained at 280 K). The pink points to a similar motif as in image (b). The yellow arrow indicates a 1D row.

After annealing to 370 K (figure 3.30 (a)), we observed a dense packed two dimensional nanostructure which is similar to the networks shown in figure 3.29 (b). The unit cell is approximately

a = 1.6 nm, b = 0.98 nm ± 0.1 nm, an angle of 50 ± 2° and the molecular coverage is about 0.90 ML. After annealing the sample to 480 K (figure 3.30 (b)), we found expanding domains which consist of molecular islands and blank boundaries between the islands. We assume that the domains have a relatively weak van der Waals type interaction between the **PT** molecules, resulting in the formation of an ordered islands phase. Thus, the blank boundaries found after annealing might be just caused by the decreased density due to a partial loss of molecules during heat treatment. The pink arrow indicates a dimeric rows motif. The molecular coverage was about 0.85 ML. The unit cell as marked with an orange is the same as in image (a). Figure 3.30 (c) shows domains with single and dimer row structures after annealing to 527 K. The molecular coverage is slightly decreased to about 0.80 ML. The single row motif, marked by a pink arrow, shows the same unit cell which is rotated by 8° with respect to the substrate plane. The other row motif, marked by the yellow arrow, looks like an one dimensional nanowire structure. The formation of a row motif would involve a weak coordination of the tert-butyl groups. That implies that separated 2D molecular domains form into 1D ordered row motifs.

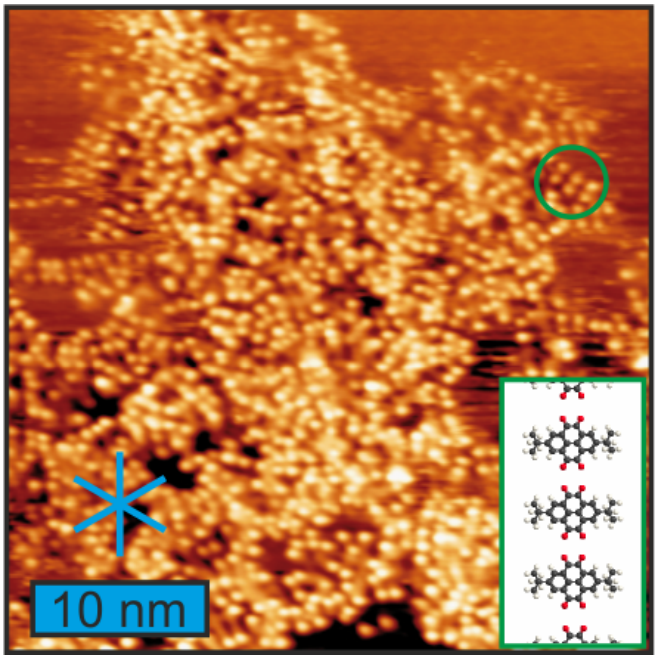

Figure 3.31: Aggregated and disordered patches of molecules after annealing to 573 K. (U_b = 1.58 V, I_t = 0.11 nA). Image recorded at room temperature.

The molecules were significantly aggregated after annealing to 573 K. Figure 3.31 shows a large scanning area STM image recorded at room temperature. At this temperature, molecules interact with neighbouring molecules randomly. However one can still identify some ordered chain like molecular structures as shown in green box at the right bottom.

3.3.2 PPD on Ag(111)

In the following the second molecule **PPD** was dosed at room temperature on the Ag(111) surface. The molecule has a functional amine group at each side of the structure. This molecular imaging on the surface is similar to the **PT** molecule where the central π conjugated system is imaged as an oval shape faintly in between the tert-butyl's bright protrusions (shown in Figure 3.32a).

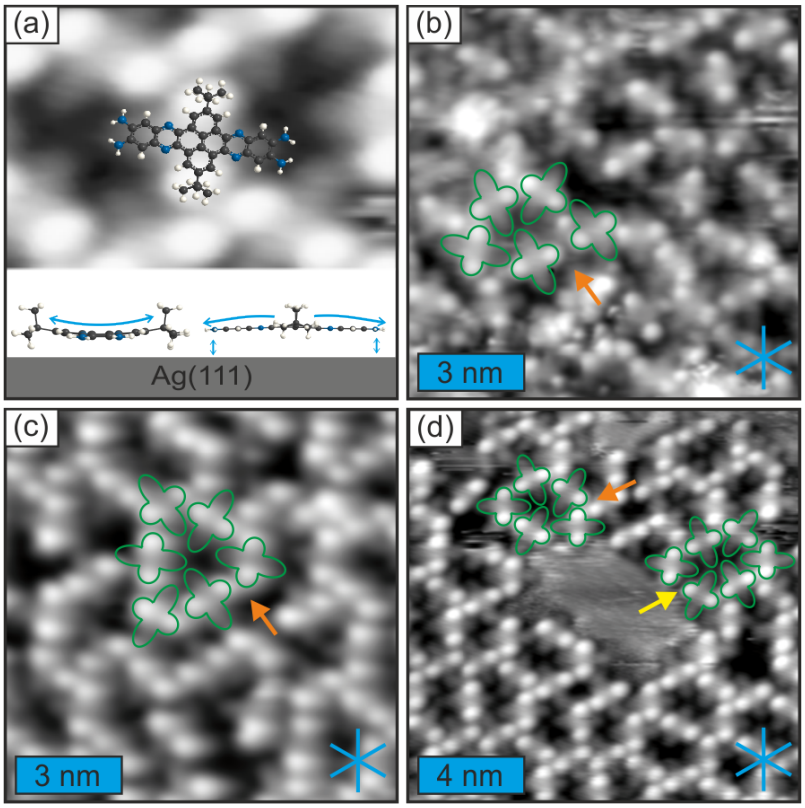

Figure 3.32: **PPD** on Ag(111). (a) Top: High resolution tophographic image with single **PPD** molecule in ball-and-stick representation superposed. Like for the **PT** molecule, the tert-butyl groups are imaged as bright protrusions whereas the molecular backbone is images an oval shape which is resolved more faintly. Bottom: side view of the tentative adsorption geometry on the Ag(111) surface. (b) Disordered molecules with a common motif found as indicated to an orange arrow after room temperature deposition. The green symbol marks the **PPD** molecules (U_b = 1.73 V, I_t = 0.20 nA, image recorded at 170 K). (c) Triangle motif and ordered molecules after annealing to 423 K (U_b = 3.11 V, I_t = 0.10 nA). (d) STM image showing the two dimensional molecular networks of **PPD** on Ag(111) after annealing 483 K. The orange and yellow arrows indicate common motifs. The Ag(111) high symmetry axes are indicated in blue (U_b = 1.90 V, I_t = 0.10 nA). Images(c-d) recorded at room temperature.

Figure 3.32 (b) shows adsorbed molecules on the surface after room temperature deposition. The individual molecules show an unordered formation. In general, physisorbed molecules have

a weak interaction with the substrate. Thus, the **PPD** molecules were highly mobile. The orange arrow indicates a structure formed by intermolecular interaction. After annealing to 423 K, we observed better ordered structures with a triangle motif as shown in Figure 3.32 (c). Figure 3.32 (d) shows a two-dimensional networks of the arranged **PPD** on Ag(111) surface after annealing to 483 K. The molecules show varying interaction motifs as indicated with an orange and yellow arrows (Figure 3.33a-c). This type of motifs appeared up to annealing temperatures between 423 K and 530 K. There are two dominant interactions in the network. One is between adjacent amine groups and other one is between amine and hydrogen atoms. At this temperature, the molecule is lying parallel to the Ag(111) plane.

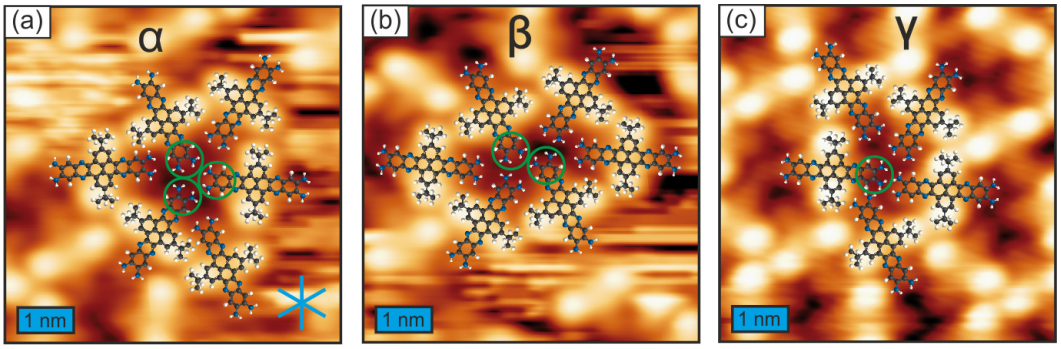

Figure 3.33: Predominant motifs of **PPD** on Ag(111). (a) Triangle motif with three amine - amine interactions (U_b = 3.11 V, I_t = 0.10 nA). (b) Parallelogram motif with two amine - amine and one amine - phenyl interactions (U_b = 3.11 V, I_t = 0.10 nA). (c) A trapezoid motif with one amine - amine and several amine - hydrogen interactions (U_b = 1.90 V, I_t = 0.10 nA). All images recorded at room temperature.

Figure 3.33 shows three dominant motifs that compose the network, which are stabilised by five or six intermolecular interactions between amine - amine and amine - hydrogen atoms. The three predominant structures in network are address as triangle (α), parallelogram (β), and trapezoid motif (γ). All results were found at submonolayer coverage. The green circles in Figure 3.33 (a) highlight the intermolecular amine-amine interactions of the triangular motif. Additionally the structure seems to be stabilized by interactions between amine and tert-butyl groups and amine - phenyl groups. The parallelogram motif in Figure 3.33 (b) shows also six intermolecular interactions to build up the hexameric assembly but this structure differes a bit from the triangular motif. As the two green circle indicate, there are two molecules that interact by amines and H-bonds. The other four molecules have interactions between -NH2$\cdots$CH- at the phenyl or tert-butyl group. The parallelogram structure is observed between room temperature and 537 K. The trapezoid motif shows only one amine that has an interaction with another amine group. The other neighbouring molecules have interactions between amine and tert-butyl or phenyl groups. This molecular structure can be observed after all annealing steps.

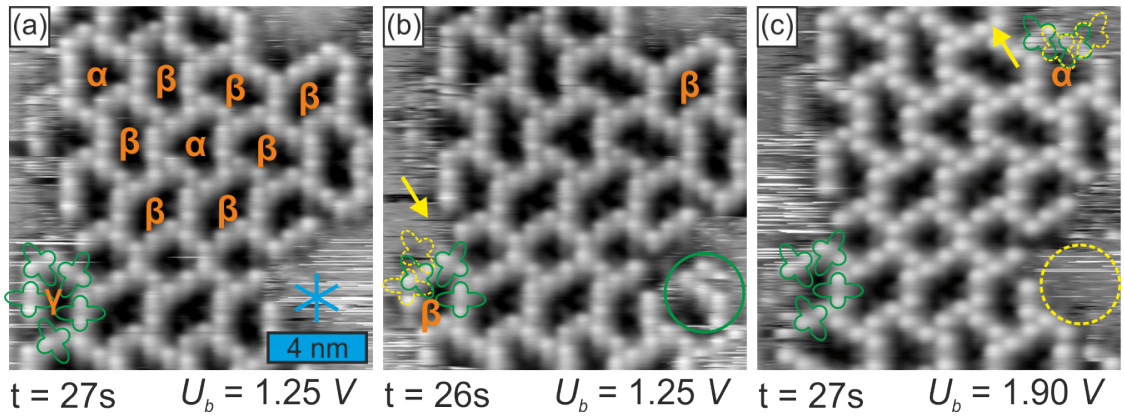

Figure 3.34: Highly regular structures after annealing to 537 K. (a) An α motif is encircled by six β motifs (U_b = 1.25 V, I_t = 0.12 nA). (b) Motif on the left bottom changed from γ to β (U_b = 1.25 V, I_t = 0.11 nA). (c) Motif transition of one β to α motif (U_b = 1.90 V, I_t = 0.12 nA). All images recorded at room temperature. Acquisition time (t) indicated under the images.

Warming up the sample to 537 K, we observed highly ordered self-assembled molecular structures shown in figure 3.34 (a). The **PPD** assembly at the center of the structure represents α motif surrounded by six β motifs. In an subsequent image (Figure 3.34 (b)) we found that one of the bordering γ structure, marked with a yellow arrow, changed to a β structure (see yellow dashed line). Moreover, we observed new molecules appearing at the border of the islands which demonstrates the high mobility of the molecules at room temperature. Thus, motifs at the border of the islands can be reformed and changed.

3.3.3 Intermixed layers on Ag(111)

To explore covalently bonded networks by an amine - ketone reaction, we dosed both molecules together on the surface. First **PT** was dosed for 7 min and subsequently **PPD** for 25 min on Ag(111) at room temperature (shown in Figure 3.35a). The intermixed assembly decorates the step edges, as marked with orange (**PPD**) and blue (**PT**) arrows, respectively. The molecules along the step edge arrange in a regular sequence. Below the step edge the molecules form small islands. After increasing the coverage of both molecules, we observed larger islands as shown in Figure 3.35 (b). The borders of the intermixed molecular islands represent **PPD** molecules as marked with the orange arrows. This is most likely due to a higher molecular coverage of the **PPD** molecules in this preparation.

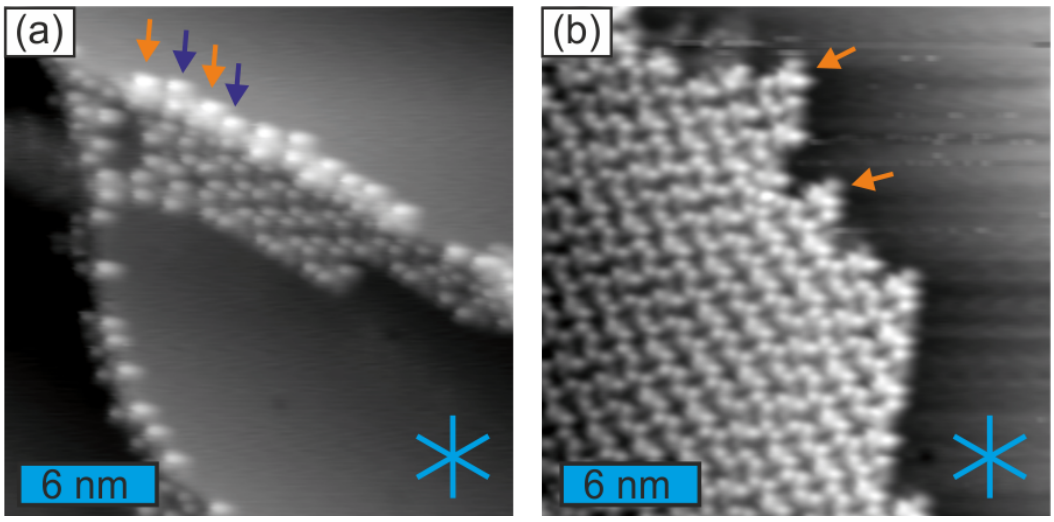

Figure 3.35: Mixture of **PPD** and **PT** molecules on Ag(111). (a) Both molecules deposited at room temperature on Ag(111) surface after first dosage. The orange arrow markes the **PPD** and the blue arrow markes the **PT** molecules. The intermixed molecules attach first to the step edges (U_b = 1.34 V, I_t = 0.06 nA, image recorded at 95 K). (b) Increased coverage after room temperature deposition. The border of an intermixed molecular island (U_b = 1.27 V, I_t = 0.11 nA, image recorded at 143 K).

After annealing the mix of **PPD** and **PT** molecules on Ag(111) to 508 K, we observed stable intermixed molecular structures similar to the one in Figure 3.35 (b). This assembly exhibits a highly regular zigzag pattern shown in Figure 3.36 (a). The bright protrusions in the image are tert-butyl groups and one can distinguish the oval shape of the **PPD** molecule in the structure as mentioned before. The ratio between the molecules is 1 : 2 (**PPD** : **PT**) and the unit cell containing one **PPD** and two **PT** molecules is approximately 2.1 nm and 2.9 nm $\pm$ 0.1 nm with an angle of 66° between a and b. To highlight the molecular interactions, molecular models were superimposed with a detail image shown in Figure 3.36 (b). The central **PPD** molecule has interactions with four

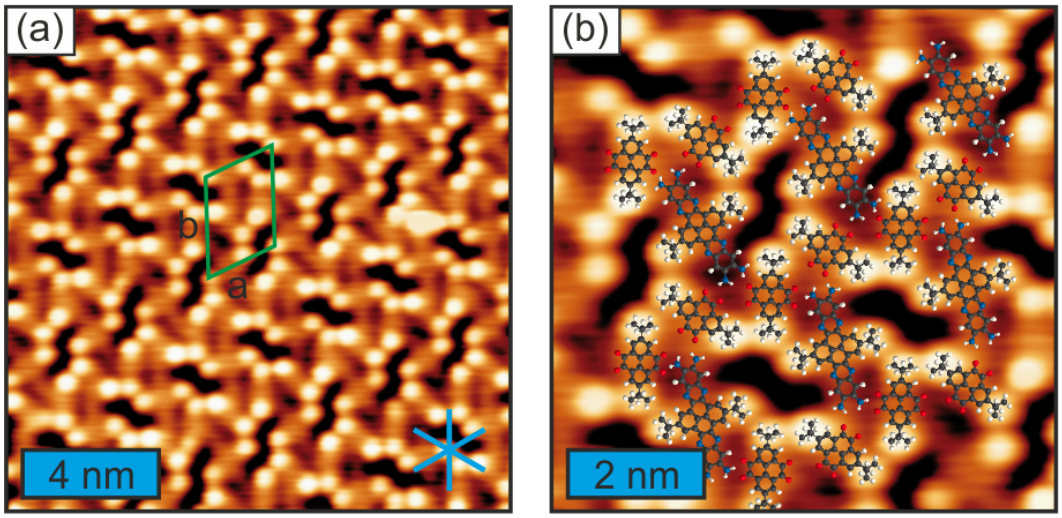

Figure 3.36: Coadsorption of **PT** and **PPD** on Ag(111) after annealing to 508 K. Very ordered two dimensional nanostructures occur between room temperature and 508 K. The unit cell of intermixed molecules is about a = 2.1 nm and b = 2.9 nm, an angle of 66°. (a) U_b = 2.89 V, I_t = 0.12 nA, image recorded at 163 K, (b) molecular models superimposed on detail image.

PT molecules between the amine groups and the diketone. One of the amine groups of the **PPD** is close to the ketone of a **PT** molecule and interacts by H-bonding. On the opposite amine group, the **PPD** interacts similar with the **PT** but the bond length seems to be bigger.

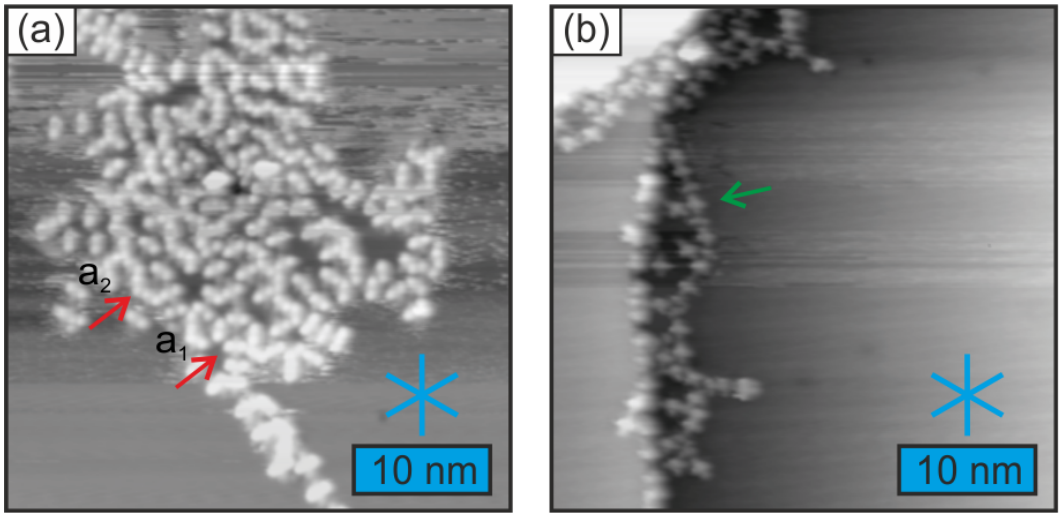

Figure 3.37: Small islands of **PPD** and linear structures close to a step edge after annealing the surface to 528 K. (a) U_b = 1.42 V, I_t = 0.12 nA, image recorded at 195 K. (b) U_b = 1.27 V, I_t = 0.12 nA, image recorded at 103 K.

In order to promote amine - ketone reactions by dehydration, the sample was annealed to 528

K for 15 min and afterwards examined at room temperature. Figure 3.37 (a) shows that the coverage of the molecules is significantly decreased and consists mainly of **PPD** molecules (almost 80%) which are clustered together and feature short linear structures. Most of the shorter **PT** molecules seem to be desorbed. The red arrow a_1 indicates a square structure which consists of four molecules interacting by their amine groups. Another arrow a_2 points to a small trapezoid structure which consists of five molecules and forms the same structure as in Figure 3.32 (d). Figure 3.37 (b) shows a short linear structure of non covalently bonded molecules (green arrow). One can clearly distinguish **PPD** molecules interacting with their amine groups. The **PT** molecule appears only twice between the **PPD** molecules.

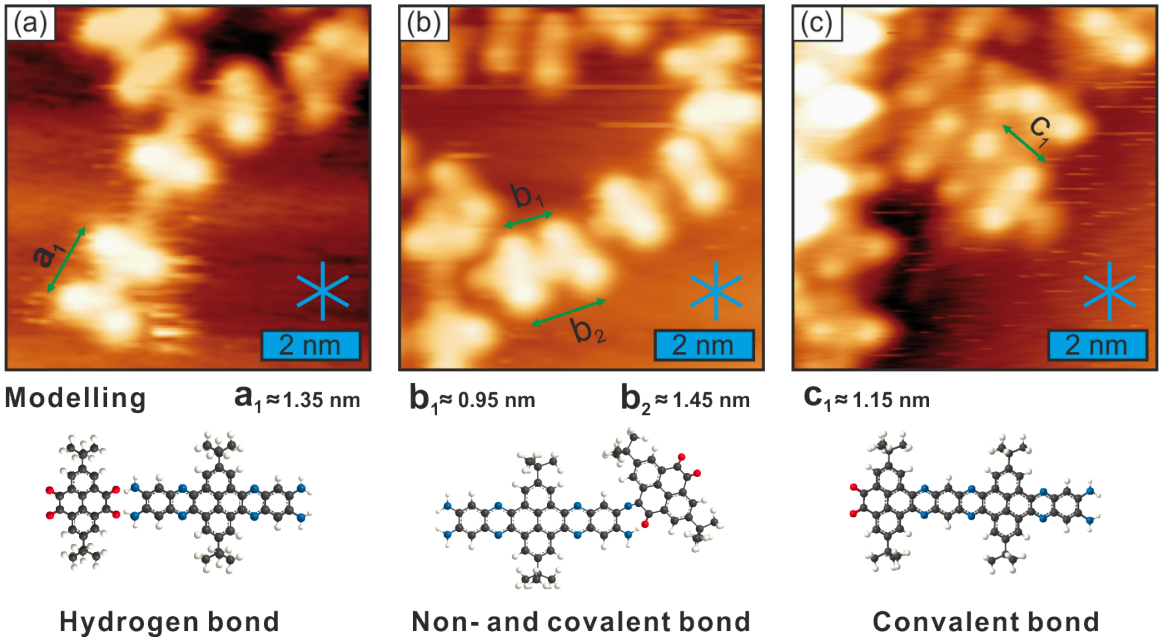

Figure 3.38: Dehydration of molecules after annealing to 523 K. Non covalent and covalent bond formation with molecular modelling. The images (a) and (b) annealed to 543 K for 60 min and (c) annealed to 523 K for 60 min. The Ag(111) high symmetry directions are indicated by blue lines. (a) U_b = 1.25 V, I_t = 0.12 nA, (b) U_b = 1.25 V, I_t = 0.12 nA, (a-b) images recorded at 200 K. (c) U_b = 1.25 V, I_t = 0.12 nA, image recorded at 163 K.

After annealing the sample to even longer and higher temperatures the networks shown in Figure 3.38 emerged ((a) 543 K, (b) 543 K (c) 523 K). At this annealing temperature, most of molecules were desorbed and disappeared from the surface or moved to the step edges. Figure 3.38 (a) shows the non-covalently bonded network of **PPD** and residual **PT** molecules. The non-covalent character of the bond between **PPD** and **PT** can be identified by the distance between the two molecules (approximately 1.35 nm $\pm$ 0.1 nm). As noted above (Figure 3.28) the distance between two covalently bonded molecules should be much shorter. Figure 3.38 (b) shows a bended molecular

assembly where one of the amine groups of the **PPD** seems to have covalently bonded to a **PT** molecule. The intermolecular distances in the structural models below the STM images fit well to the distances measured by STM (about b_1 = 0.95 $\pm$ 0.1 nm and b_2 = 1.45 nm $\pm$ 0.1 nm). After annealing the surface to 523 K for 60 min (Figure 3.38 (c)), single covalently linked **PPD** and **PT** molecules could be observed. The structural model at the bottom of the image exhibits a similar intermolecular distance as in the STM measurement (almost 1.15 nm $\pm$ 0.1 nm) and it seems that two **PPD** molecules have reacted with on **PT** molecule. Thus we can assume, that covalent bonds have formed. However, only few of the molecules have reacted with each other.

3.3.4 Conclusion

In conclusion, we systematically investigated the assembly of the **PPD** and **PT** molecules on Ag(111) in dependence of the annealing temperature. First, we observed stable, hydrogen bonded islands of **PT** molecules. After annealing the sample, the molecular networks can be changed to a more loosely bound assembly. Upon even higher annealing to 573 K, the molecules were aggregated and disordered on surface. The **PPD**'s molecules self-assembled into H-bonded networks which can not be affected by thermal treatment between room temperature and 537 K. Three different kind of substructures (α, β and γ motif) could be observed. After the coadsorbing both molecules on Ag(111) and after annealing above 508 K, no amine - ketone reactions to covalently bonded networks could be observed. At higher annealing temperature, the molecules desorb from the surface. The intermixed molecules reveal a zigzag pattern up to over 523 K. At annealing temperatures over 523 K, most of the **PT** molecules were desorbed leaving an excess of **PPD** molecules on the surface. Nevertheless short ranged covalent network comprising dimers and trimers could be observed.

4 Summary and Conclusions

This thesis comprises three exempla are studies of organic molecules on close packed noble metal surfaces by means of STM supported by X-ray spectroscopy. In the first part we addressed the self-assembly of a single molecule, diethylstilbestrol on the Ag(111) and the Cu(111) surfaces as a function of annealing temperature (Figure 4.1). On Ag(111), we observed three distinct molecular motifs: the windmill, the shingle, and the row motif. The windmill motif exhibits organisational chirality and can appear in either clockwise or counter clockwise orientation. The molecular islands which are built by this motif are enantiopure in the expression of the windmill orintation, i.e. they are composed solely by clockwise (or counter clockwise) windmills and they have been observed after annealing the overlayer structure at the temperature range from room temperature to 350 K. Within the the shingle motif, we were able to identify the orientation of the ethyl groups by obtaining high submolecular resolution STM images. The structures characterised by the shingle motif co-existed with the windmill structures. After annealing the sample to 350 K, most of the DES molecules desorbed from the on Ag(111) surface. The remaining molecules arranged in a different molecular structure with a row motif and nucleated in the vicinity of the atomic step edges. With XPS we observed that the O 1s core level shows a certain degree of deprotonation which is promoted by annealing to temperatures above room temperature. After a close inspection of the surface molecular footprint of DES within the shingle and the windmill motif, we concluded that the DES on Ag(111) adopts a *trans* configuration. On the Cu(111) surface the DES molecules assembled in a star structure and a stripe structure. The star motif dominates the STM images obtained after annealing up to a temperature of 400 K. The intermolecular spacing within the star motif allowed us to propose that the molecule adopts a *cis* configuration on the Cu(111) surface, in contrast to the Ag(111) case. The stripe motif was observed after annealing to 350 K and attributed to a different adsorption. The XPS showed that approximately half of the O 1s signal corresponded to phenolate upon room temperature deposition and it consists solely of phenolate after annealing to 450 K. After annealing to even higher temperatures annealing, the molecules form a chain-like structure. We tentatively associate the formation of these chains with the creation of Cu catalysed covalent bonds.

Figure 4.2 illustrates the second topic of this thesis, which included the STM study of 2H-TPP on Ag(111) undergoing temperature induced intramolecular and intermolecular dehydrogenation reactions enabling the formation of new C-C bonds. 2H-TPP on Ag(111) adopts a saddle-shape deformation of the macrocycle. After annealing the sample to 550 K, the 2H-TPP undergoes four

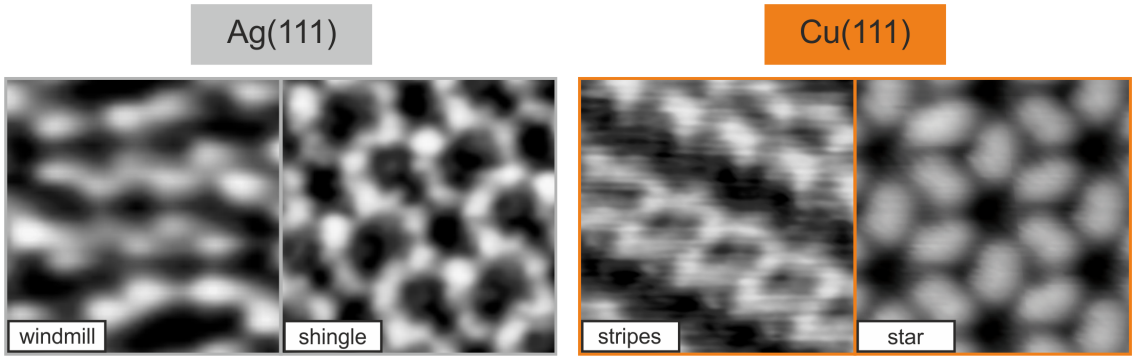

Figure 4.1: Graphical summary of the self-assembled structures formed by DES molecules on Ag(111) and on Cu(111).

intramolecular cyclodehydrogenation reactions providing in four species (**3** to **6**), which we were able to identify by STM. We dosed the $Ru_3(CO)_{12}$ metal precursors on the flat 2H-TPP molecules and post annealed the sample to 550 K. We identified metalation events of the flat 2H-TPP by the appearance of a new protrusion within the centre of the macrocycle. Irrespective of their metalation state, after annealing to temperatures above 673 K, the flat 2H-TPP molecules undergo a homo-coupling reactions, albeit with low selectivity. The homo-coupling products include dimers, trimers, oligomers, and polymers.

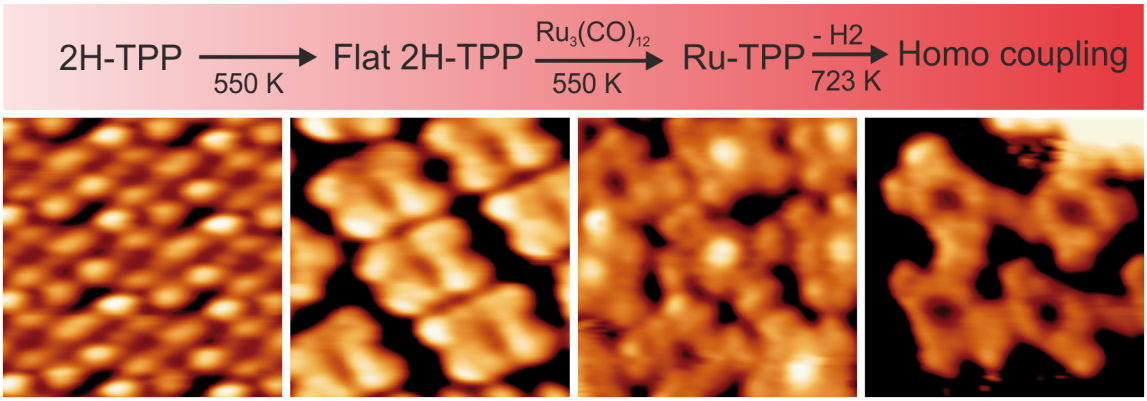

Figure 4.2: Graphical summary of the chemical transformations of the 2H-TPP molecules on Ag(111) as a function of temperature.

Finally, we studied the organizational interaction and reactivity of **PT** and **PPD** on the Ag(111) surface (Figure 4.3). Initially both molecules were investigated individually. The STM imaging characteristics of both were established and it was found that both molecules remain on the surface after a thermal treatment up to 573 K. The **PT** molecules on the Ag(111) surface, form

dense packed islands. With thermal annealing we find that this packing is occasionally interrupted along the side of the ketone moieties, resulting in rows of molecules with greater separations. The frequency of this new type of interaction increases with the annealing temperature. The **PPD** molecules on the Ag(111) surface form islands composed by three molecular domains. After depositing both molecules sequentially on the surface, we observed that they readily form intermixed hydrogen bonded islands with a **PT** : **PPD** stoichiometry of 2 : 1 which can be observed even after heating the sample up to 508 K. Following an annealing of the sample to 523 K, the molecules have reacted and formed polyimine oligomers. The high annealing temperatures required (in comparison with the Schiff base formation under ambient conditions in a three dimensional environment), as well as the limited length of the polymers, indicate that the metal surface and planar reactant configuration does not promote the reaction. Future work would require the fine tuning of the relative height of the reacting ketones and amines from the substrate by introducing different bulky substituents.

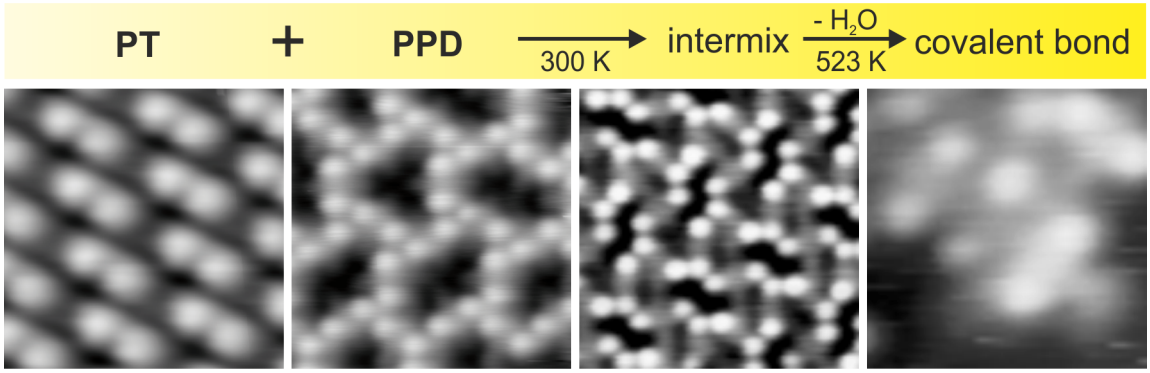

Figure 4.3: Summary of the tetraketone **PT** and the tetramine **PPD** molecules on Ag(111) and their mixture as a function of temperature.

5 Acknowledgments

First of all, I would like to thank Prof. Johannes Barth for giving me the good opportunity to work in the field of surface science. I am devoutly thankful to Dr. Harmut Schlichting for supervision, mentoring and helping whenever I want. Especially, he introduced the electrospray ionization technique to me, which is my first project, and which is very fantastic instrument for the surface science field. Unfortunately, however, this project did not finish during my work. I would greatly like to thank Dr. Joachim Reichert for guidance, supervision and a lot of help, whenever I need. I am extremely thankful to Dr. Anthoula Papageorgiou for introducing me the VT-STM and disabusing me when I was wrong. I would like to thank the Aarhus-STM team, Dr.Özge Sağlam, Dr. Sybille Fischer, Julian Lloyd, Yetik Görsel and Jiang Li for the good atmosphere to work and discussions. Furthermore, I would like to thank the synchrotron team, Dr. Florian Klappenberger, Dr. Francesco Allegretti, Dr. David Duncan and Dr. Katharina Diller for introducing the synchrotron to me at the HE-SGM beamline at BESSY II.

I am very thankful to Kamila Wilson and Viktoria Blaschek for the English proofreading, living support and helping me with the documents. I also want to thank to Max Glanz, Karl Eberle, Karl Kölbl and Reinhold Schneider for the technical support. I am also thankful to the people of my office, Dr. Nenad Kepčia, He, Yuanqin and Paszkiewicz, Mateusz for the great discussions of the economy, science, society and life. I want to thank all members of E20.

I am great thankful to my family. To Suntaek Oh and Sunhyang Jung, my parents, for their endless love and supporting wherever I live. To Sungrok Oh and Sungtae Oh, my brothers, for their praying for me since I have left in Korea. To my wife, Eunjung Kim, for the daily support, patience, encouraging and praying for me. To my lovely sun, Juwon Oh, for the giving me the laugh and hope everyday. I am very thankful to my pastors, Hyunkil Lim, Taeyoung Yoo, Jinyoul Nam and Hyunchul Won, for their praying for me to lead a way of the Lord when I was exhausted. Finally, I am deeply thankful to my Lord, God, who leads me to His way always. He guides me and is still stay on my side. Immanuel.

6 List of Publications

- Steering the conformation of diethylstilbestrol by the metal surface. S. C. Oh, A. C. Papageorgiou, J. A. Lloyd, J. Reichard and J. V. Barth, *In preparation*

- Temperature-dependent templated growth of porphine thin films on the (111) facets of copper and silver. K. Diller, F. Klappenberger, F. Allegretti, A. C. Papageorgiou, S. Fischer, D. A. Duncan, R. Maurer, J. A. Lloyd, S. C. Oh, K. Reuter, and J. V. Barth, *Submitted*

- Unusual deprotonated alkynyl hydrogen bonding induces robust hydrocarbon assembly at a metal interface. Q. Zhang, J. Björk, P. Weber, R. Hellwig, K. Diller, A. C. Papageorgiou, S. C. Oh, S. Fischer, F. Allegretti, S. Klyatskaya, M. Ruben, J. V. Barth and F. Klappenberger, *Submitted*

- Self-assembly and chemical modifications of Bisphenol A on Cu(111): Interplay between ordering and thermally activated stepwise deprotonation. S. Fischer, A. C. Papageorgiou, J. A. Lloyd, S. C. Oh, K. Diller, F. Allegretti, F. Klappenberger, A. P. Seitsonen, J. Reichert and J. V. Barth, *ACS nano*, **2014**, 8, 207-215.

- Self-termination protocol for an interfacial complexation reaction in vacuo by metal-organic chemical vapour deposition. A. C. Papageorgiou, S. Fischer, Seung Cheol Oh, Ö. Saglam, J. Reichert, A. Wiengarten, K. Seufert, S. Vijayaraghavan, D. Écija, W. Auwärter, F. Allegretti, R. G. Acres, K. C. Prince, K. Diller, F. Klappenberger, and J. V. Barth, *ACS nano*, **2013** ,7 4520-4526.

- Role of coverage and vacancy defect in adsorption and desorption of benzene on Si(001)-2xn surface. S. C. Oh, K. W. Kim, A. H. Mamun, H-J. Lee, J. R. Hahn. *Bull. Korean Chem. Soc.* **2010**, 31(1), 162.

- Adsorption structures of small aromatic molecules on Si(5 5 12) - 2x1. S. H. Jang, S. C. Oh, H. Jeong, S. Jeong, J. R. Hahn, *J. Korean Vac. Soc.*, **2006**, 15(1), 50-56.

Bibliography

[1] Richard Feynman. There's plenty of room at the bottom. *Enginnering and Science*, 23:22–26, 1960.

[2] Johannes V. Barth, Giovanni Costantini, and Klaus Kern. Engineering atomic and molecular nanostructures at surfaces. *Nature*, 437:671, 2005.

[3] Muniza Zahid, Byeonghoon Kim, Rafaqat Hussain, Rashid Amin, Sung Ha Park. DNA nanotechnology: a future perspective. *Nanoscale Research Letters*, 8:119, 2013.

[4] Andrew N. Young and Brad A Kairdolf. Nanotechnology in Molecular Diagnostics. In Liang Cheng, David Y. Zhang, and John N. Eble, editors, *Molecular Genetic Pathology*, pages 383–398. Springer New York, 2013.

[5] KK Jain. Nanodiagnostics: application of nanotechnology in molecular diagnostics. *Expert Review of Molecular Diagnostics*, 3(2):153–161, 2003. PMID: 12647993.

[6] Shawn J. Tan, Michael J. Campolongo, Dan Juo and Wenlong Cheng. Building plasmonic nanostructures with DNA. *Nature nanotechnology*, 8:268, 2011.

[7] Seyed-Fakhreddin Torabi and Yi Lu. Small-molecule diagnostics based on functional DNA nanotechnology: a dipstick test for mercury. *Faraday Discuss.*, 149:125–135, 2011.

[8] Jean-Marie Lehn. Supramolecular chemistry-Scope and Perspectives molecules, supramolecules, and molecular devices (Novel Lecture). *Angewandte Chemie, International Edition*, 27:89, 1988.

[9] L. Lafferentz, V. Eberhardt, C. Dri, C. Africh, G. Comelli, F. Esch, S. Hecht, L. Grill. Controlling on-surface polymerization by hierarchical and substrate-directed growth. *Nature chemistry*, 2012.

[10] Gerd Binnig and Heinrich Rohrer. Scanning tunneling microscopy. *Helv. Phys. Acta*, 55(6):726–735, 1982.

[11] Gerd Binnig and Heinrich Rohrer. Scanning tunneling microscopy - from birth to adolescence. *Rev. Mod. Phys.*, 59:615–625, Jul 1987.

[12] A Castellanos-Gomez, N Agrait, and G Rubio-Bollinger. Carbon fibre tips for scanning probe microscopy based on quartz tuning fork force sensors. *Nanotechnology*, 21(14):145702, 2010.

[13] R.J. Colton, S.M. Baker, J.D. Baldeschwieler, and W.J. Kaiser. 'Oxide-free' tip for scanning tunneling microscopy. *Appl. Phys. Lett.*, 51(5):305, 1987.

[14] T. Ohmori, L. A. Nagahara, K. Hashimoto, A. Fujishima. Characterization of carbon material as a scanning tunneling microscopy tip for in situ electrochemical studies. *Rev. Sci. Instrum.*, 65(2):404, 1994.

[15] Cattien V Nguyen, Kuo-Jen Chao, Ramsey M D Stevens, Lance Delzeit, Alan Cassell, Jie Han, and M Meyyappan. Carbon nanotube tip probes: stability and lateral resolution in scanning probe microscopy and application to surface science in semiconductors. *Nanotechnology*, 12(3):363, 2001.

[16] T Arai, S Gritschneder, L Tröger, and M Reichling. Carbon tips as sensitive detectors for nanoscale surface and sub-surface charge. *Nanotechnology*, 15(9):1302, 2004.

[17] T Uchihashi, M Higgins, Y Nakayama, J E Sader and S P Jarvis. Quantitative measurement of solvation shells using frequency modulated atomic force microscopy. *Nanotechnology*, 16(3):S49, 2005.

[18] K S Yeong, C B Boothroyd and J T L Thong. The growth mechanism and field-emission properties of single carbon nanotips. *Nanotechnology*, 17(15):3655, 2006.

[19] H. Konishi, Y. Murata, W. Wongwiriyapan, M. Kishida, K. Tomita, K. Motoyoshi, S. Honda, M. Katayama, S. Yoshimoto, K. Kubo, R. Hobara, I. Matsuda, S. Hasegawa, M. Yoshimura, J.-G. Lee, and H. Mori. High-yield synthesis of conductive carbon nanotube tips for multiprobe scanning tunneling microscope. *Review of Scientific Instruments*, 78(1):–, 2007.

[20] Hui Zhou. *Probing the Properties of the Molecular Adlayers on Metal Substrates: Scanning Tunneling Microscopy Study of Amine Adsorption on Au(111) and Graphene Nanoislands on Co(0001)*. PhD thesis, COLUMBIA UNIVERSITY, 2011.

[21] Lorenz Kampschulte. *Nanoscale Ordering at the Liquid-Solid Interface using Self-Assembly Principles*. PhD thesis, LMU, 2006.

[22] J. Tersoff. Role of tip electronic structure in scanning tunneling microscope images. *Phys. Rev. B*, 41:1235–1238, Jan 1990.

[23] J. Tersoff and D R Hamann. Theory of the scanning tunneling microscope. *Phys. Rev. B*, 31(2):805–813, January 1985.

[24] http://www.ntmdt.com/spm-principles/view/constant-current-mode/.

[25] Sybille Fischer. *Combined STM and X-ray spectroscopy study of surface-confined biologically relevant molecules*. PhD thesis, Techniche Universiatät München, 2013.

[26] E. K. Vestergaard. *Scanning Tunneling Microscopy Studies of Model Systems Relevant to Catalysis*. PhD thesis, University of Aarhus, 2004.

[27] I Horcas, R Fernández, J M Gómez-Rodríguez, J Colchero, J Gómez-Herrero, and A M Baro. WSXM: a software for scanning probe microscopy and a tool for nanotechnology. *Rev. Sci. Instrum.*, 78(1):013705, January 2007.

[28] Anthoula C. Papageorgiou, Sybille Fischer, Seung Cheol Oh, Ö zge Saglam, Joachim Reichert, Alissa Wiengarten, Knud Seufert, Saranyan Vijayaraghavan, David Èeija, Willi Auwärter, Francesco Allegretti, Robert G. Acres, Kevin C. Prince, Katharina Diller, Florian Klappenberger, and Johannes V. Barth. Self-Terminating Protocol for an Interfacial Complexation Reaction *inVacuo* by Metal - Organic Chemical Vapor Deposition. *ACS Nano*, 7(5):4520–4526, 2013.

[29] F. R. Elder, A. M. Gurewitsch, R. V. Langmuir, and H. C. Pollock. Radiation from Electrons in a Synchrotron. *Phys. Rev.*, 71:829–830, Jun 1947.

[30] Hähner, Georg. Near edge X-ray absorption fine structure spectroscopy as a tool to probe electronic and structural properties of thin organic films and liquids. *Chem. Soc. Rev.*, 35(12):1244–1255, December 2006.

[31] EPSIM 3D/JF Santarelli. Synchrotron soleil, 2005.

[32] Stöhr, Joachim. *NEXAFS spectroscopy*. Springer-Verlag, Berlin, Heidelberg, 1992.

[33] Shirley, D. A. High-resolution X-ray photoemission spectrum of the valence bands of gold. *Phys. Rev. B*, 5(12):4709–4714, June 1972.

[34] Exposure in utero to diethylstilbestrol and related synthetic hormones: Association with vaginal and cervical cancers and other abnormalities. *JAMA*, 236(10):1107–1109, 1976.

[35] Arthur L. Herbst, Howard Ulfelder, and David C. Poskanzer. Adenocarcinoma of the Vagina. *New England Journal of Medicine*, 284(16):878–881, 1971. PMID: 5549830.

[36] Julie R. Palmer, Lauren A. Wise, Elizabeth E. Hatch, Rebecca Troisi, Linda Titus-Ernstoff, William Strohsnitter, Raymond Kaufman, Arthur L. Herbst, Kenneth L. Noller, Marianne Hyer, and Robert N. Hoover. Prenatal Diethylstilbestrol Exposure and Risk of Breast Cancer. *Cancer Epidemiology Biomarkers & Prevention*, 15(8):1509–1514, 2006.

[37] Helen Klip, Janneke Verloop, Jan D van Gool, Marlies ETA Koster, Curt W Burger, and Flora E van Leeuwen. Hypospadias in sons of women exposed to diethylstilbestrol in utero: a cohort study . *The Lancet*, 359(9312):1102 – 1107, 2002.

[38] Jean-Francçois Neault and Heidar-Ali Tajmir-Riahi. Diethylstilbestrol-DNA Interaction Studied by Fourier Transform Infrared and Raman Spectroscopy. *The Journal of Biological Chemistry*, 271:8140, 1996.

[39] Hari K. Bhat, Xueliang Han, Alicja Gladek, and Joachim G. Liehr. Regulation of the formation of the major diethylstilbestrol - DNA adduct and some evidence of its structure. *Carcinogenesis*, 15(10):2137–2142, 1994.

[40] Benjamin Hinrichs, Muhammad Zahid, Muhammad Saeed, Mohammed F. Ali, Ercole L. Cavalieri and Eleanor G. Rogan. Formation of diethylstilbestrol DNA adducts in human breast epithelial cells and inhibition by resveratrol. *The Journal of Steroid Biochemistry and Molecular Biology*, 127(35):276 – 281, 2011.

[41] Rami Haddad, Amanda Kasneci, Kathryn Mepham, Igal A. Sebag and Lorraine E. Chalifour. Gestational exposure to diethylstilbestrol alters cardiac structure/function, protein expression and DNA methylation in adult male mice progeny. *Toxicology and Applied Pharmacology*, 266:27, 2013.

[42] Sybille Fischer, Anthoula C. Papageorgiou, Julian A. Lloyd, Seung Cheol Oh, Katharina Diller, Francesco Allegretti, Florian Klappenberger, Ari Paavo Seitsonen, Joachim Reichert, and Johannes V. Barth. Self-Assembly and Chemical Modifications of Bisphenol A on Cu(111): Interplay Between Ordering and Thermally Activated Stepwise Deprotonation. *ACS Nano*, 8(1):207–215, 2014.

[43] Dana C. Dolinoy, Dale Huang, and Randy L. Jirtle. Maternal nutrient supplementation counteracts bisphenol A-induced DNA hypomethylation in early development. *Proceedings of the National Academy of Sciences*, 104(32):13056–13061, 2007.

[44] Jason G. Bromer, Yuping Zhou, Melissa B. Taylor, Leo Doherty, and Hugh S. Taylor. Bisphenol-A exposure in utero leads to epigenetic alterations in the developmental programming of uterine estrogen response. *The FASEB Journal*, 24(7):2273–2280, 2010.

[45] Julian Andreas Lloyd. Biologically active molecules confined in 2D: self-assembly, thermal behavior & chemical transformations. Master's thesis, Technische Universität München, 2013.

[46] Sathish Srinivasan, Jerome C Nwachukwu, Alex A Parent, Valerie Cavett, Jason Nowak, Travis S Hughes, Douglas J Kojetin, John A Katzenellenbogen, Kendall W Nettles. Ligand-binding dynamics rewire cellular signaling via estrogen receptor-a. *Nature Chemical Biology*, 9:326, 2013.

[47] William A. White and Nelson H. Ludwig. Isomerization of .alpha.,.alpha.'-diethylstilbestrol, isolation and characterization of the cis isomer. *Journal of Agricultural and Food Chemistry*, 19(2):388–390, 1971. PMID: 5546172.

[48] Remy Pawlak, Sylvain Clair, Vincent Oison, Mathieu Abel, Oualid Ourdjini, Nikolas A. A. Zwaneveld, Didier Gigmes, Denis Bertin, Laurent Nony, and Louis Porte. Robust Supramolecular Network on Ag(111): Hydrogen-Bond Enhancement through Partial Alcohol Dehydrogenation. *ChemPhysChem*, 10(7):1032–1035, 2009.

[49] M. J. Frisch, G. W. Trucks, H. B. Schlegel, G. E. Scuseria, M. A. Robb, J. R. Cheeseman, G. Scalmani, V. Barone, B. Mennucci, G. A. Petersson, H. Nakatsuji, M. Caricato, X. Li, H. P. Hratchian, A. F. Izmaylov, J. Bloino, G. Zheng, J. L. Sonnenberg, M. Hada, M. Ehara, K. Toyota, R. Fukuda, J. Hasegawa, M. Ishida, T. Nakajima, Y. Honda, O. Kitao, H. Nakai, T. Vreven, J. A. Montgomery, Jr., J. E. Peralta, F. Ogliaro, M. Bearpark, J. J. Heyd, E. Brothers, K. N. Kudin, V. N. Staroverov, R. Kobayashi, J. Normand, K. Raghavachari, A. Rendell, J. C. Burant, S. S. Iyengar, J. Tomasi, M. Cossi, N. Rega, J. M. Millam, M. Klene, J. E. Knox, J. B. Cross, V. Bakken, C. Adamo, J. Jaramillo, R. Gomperts, R. E. Stratmann, O. Yazyev, A. J. Austin, R. Cammi, C. Pomelli, J. W. Ochterski, R. L. Martin, K. Morokuma, V. G. Zakrzewski, G. A. Voth, P. Salvador, J. J. Dannenberg, S. Dapprich, A. D. Daniels, Ö. Farkas, J. B. Foresman, J. V. Ortiz, J. Cioslowski, and D. J. Fox. Gaussian 09 Revision D.01. Gaussian Inc. Wallingford CT 2009.

[50] G. Beamson and D. Briggs. High resolution XPS of organic polymers, the scienta ESCA300 database. *Advanced Materials*, 5(10):778–778, 1993.

[51] Christian Bombis, Sigrid Weigelt, Martin M. Knudsen, Martin Norgaard, Carsten Busse, Erik LAgsgaard, Flemming Besenbacher, Kurt V. Gothelf, and Trolle R. Linderoth. Steering Organizational and Conformational Surface Chirality by Controlling Molecular Chemical Functionality. *ACS Nano*, 4(1):297–311, 2010. PMID: 20000754.

[52] Manfred Parschau, Sara Romer, and Karl-Heinz Ernst. Induction of Homochirality

in Achiral Enantiomorphous Monolayers. *Journal of the American Chemical Society*, 126(47):15398–15399, 2004. PMID: 15563164.

[53] Roman Fasel, Manfred Parschau, and Karl-Heinz Ernst. Amplification of chirality in two-dimensional enantiomorphous lattices. *Nature*, 436:449–452, 2006.

[54] Sebastian Stepanow, Nian Lin, Franck Vidal, Aitor Landa, Mario Ruben, Johannes V. Barth, and Klaus Kern. Programming Supramolecular Assembly and Chirality in Two-Dimensional Dicarboxylate Networks on a Cu(100) Surface. *Nano Letters*, 5(5):901–904, 2005.

[55] J-S. Zhou, J. Chan, and J. B. Goodenough. Copper-Oxygen Bond Length and Self-Doping In R2CuO4 (R = Pr, Nd, Sm, Eu, Gd). *Phys. Rev. B*, 47:5477–5480, Mar 1993.

[56] D. Kreikemeyer-Lorenzo, W. Unterberger, D. A. Duncan, M. K. Bradley, T. J. Lerotholi, J. Robinson, and D. P. Woodruff. Face-Dependent Bond Lengths in Molecular Chemisorption: The Formate Species on Cu(111) and Cu(110). *Phys. Rev. Lett.*, 107:046102, Jul 2011.

[57] L. Scudiero, K. W. Hipps, and Dan E. Barlow. A Self-Organized Two-Dimensional Bimolecular Structure. *J. Phys. Chem. B*, 107:2903, 2003.

[58] G. Polzonetti, C. Battocchio, A. Goldoni, R. Larciprete, V. Carravetta, R. Paolesse, M.V. Russo. Interface formation between C60 and diethynyl-Zn-porphyrinato investigated by SR-induced photoelectron and near-edge X-ray absorption (NEXAFS) spectroscopies. *Chemical Physics*, 297:307, 2004.

[59] W. Auwärter, A. Weber-Bargioni, A. Riemann, A. Schiffrin, O. Gröning, R. Fasel, and J. V. Barth. Self-assembly and conformation of tetrapyridyl-porphyrin molecules on Ag(111). *The Journal of Chemical Physics*, 124(19):–, 2006.

[60] Willi Auwärter, Florian Klappenberger, Alexander Weber-Bargioni, Agustin Schiffrin, Thomas Strunskus, Christof Wöll, Yan Pennec, Andreas Riemann, and Johannes V. Barth. Conformational Adaptation and Selective Adatom Capturing of Tetrapyridyl-porphyrin Molecules on a Copper (111) Surface. *Journal of the American Chemical Society*, 129(36):11279–11285, 2007. PMID: 17705476.

[61] Willi Auwärter, Alexander Weber-Bargioni, Susan Brink, Andreas Riemann, Agustin Schiffrin, Mario Ruben, and Johannes V. Barth. Controlled Metalation of Self-Assembled Porphyrin Nanoarrays in Two Dimensions. *ChemPhysChem*, 8(2):250–254, 2007.

[62] Florian Buchner, Karmen Comanici, Norbert Jux, Hans-Peter Steinruck, Hubertus Marbach. Polymorphism of Porphyrin Molecules on Ag(111) and How to Weave a Rigid Monolayer. *J. Phys. Chem. C*, 111:13531, 2007.

[63] David Écija, Marta Trelka, Christian Urban, Paula de Mendoza, Eva Mateo-Martò, Celia Rogero, José A. Martì-Gago, Antonio M. Echavarren, Roberto Otero, José M. Gallego, and Rodolfo Miranda. Molecular Conformation, Organizational Chirality, and Iron Metalation of meso-Tetramesitylporphyrins on Copper(100). *The Journal of Physical Chemistry C*, 112(24):8988–8994, 2008.

[64] Florian Buchner, Ken Flechtner, Yun Bai, Elisabeth Zillner, Ina Kellner, Hans-Peter Steinrük, Hubertus Marbach, and J. Michael Gottfried. Coordination of Iron Atoms by Tetraphenylporphyrin Monolayers and Multilayers on Ag(111) and Formation of Iron-Tetraphenylporphyrin. *The Journal of Physical Chemistry C*, 112(39):15458–15465, 2008.

[65] M. Eichberger, M. Marschall, J. Reichert, A. Weber-Bargioni, W. Auwärter, R. L. C. Wang, H. J. Kreuzer, Y. Pennec, A. Schiffrin, and J. V. Barth. Dimerization Boosts One-Dimensional Mobility of Conformationally Adapted Porphyrins on a Hexagonal Surface Atomic Lattice. *Nano Letters*, 8(12):4608–4613, 2008.

[66] Stadler Christoph, Hansen Soren, Kroger Ingo, Kumpf Christian, Umbach Eberhard. Tuning intermolecular interaction in long-range-ordered submonolayer organic films. *Nat. Phys.*, 5:153, 2009.

[67] Giovanni Di Santo, Carla Castellarin-Cudia, Mattia Fanetti, Bidini Taleatu, Patrizia Borghetti, Luigi Sangaletti, Luca Floreano, Elena Magnano, Federica Bondino, and Andrea Goldoni. Conformational Adaptation and Electronic Structure of 2H-Tetraphenylporphyrin on Ag(111) during Fe Metalation. *The Journal of Physical Chemistry C*, 115(10):4155–4162, 2011.

[68] Di Santo, Giovanni and Sfiligoj, Cristina and Castellarin-Cudia, Carla and Verdini, Alberto and Cossaro, Albano and Morgante, Alberto and Floreano, Luca and Goldoni, Andrea. Changes of the Molecule-Substrate Interaction upon Metal Inclusion into a Porphyrin. *Chemistry A European Journal*, 18(40):12619–12623, 2012.

[69] J. Michael Gottfried, Ken Flechtner, Andreas Kretschmann, Thomas Lukasczyk, and Hans-Peter Steinrück. Direct Synthesis of a Metalloporphyrin Complex on a Surface. *Journal of the American Chemical Society*, 128(17):5644–5645, 2006.

[70] Tatyana E. Shubina, Hubertus Marbach, Ken Flechtner, Andreas Kretschmann, Norbert Jux, Florian Buchner, Hans-Peter Steinrück, Timothy Clark, and J. Michael Gottfried. Principle

and Mechanism of Direct Porphyrin Metalation: Joint Experimental and Theoretical Investigation. *Journal of the American Chemical Society*, 129(30):9476–9483, 2007. PMID: 17625856.

[71] Min Chen, Xuefei Feng, Liang Zhang, Huanxin Ju, Qian Xu, Junfa Zhu, J. Michael Gottfried, Kurash Ibrahim, Haijie Qian, and Jiaou Wang. Direct Synthesis of Nickel(II) Tetraphenylporphyrin and Its Interaction with a Au(111) Surface: A Comprehensive Study. *The Journal of Physical Chemistry C*, 114(21):9908–9916, 2010.

[72] Alexander Weber-Bargioni, Willi Auwärter, Florian Klappenberger, Joachim Reichert, Simon Lefrancois, Thomas Strunskus, Christof Wöll, Agustin Schiffrin, Yan Pennec, and Johannes V. Barth. Visualizing the Frontier Orbitals of a Conformationally Adapted Metalloporphyrin. *ChemPhysChem*, 9(1):89–94, 2008.

[73] Yang Li, Jie Xiao, Tatyana E. Shubina, Min Chen, Ziliang Shi, Martin Schmid, Hans-Peter Steinrück, J. Michael Gottfried, and Nian Lin. Coordination and Metalation Bifunctionality of Cu with 5,10,15,20-Tetra(4-pyridyl)porphyrin: Toward a Mixed-Valence Two-Dimensional Coordination Network. *Journal of the American Chemical Society*, 134(14):6401–6408, 2012.

[74] David Écija, Willi Auwärter, Saranyan Vijayaraghavan, Knud Seufert, Felix Bischoff, Kentaro Tashiro, and Johannes V. Barth. Assembly and Manipulation of Rotatable Cerium Porphyrinato Sandwich Complexes on a Surface. *Angewandte Chemie International Edition*, 50(17):3872–3877, 2011.

[75] Florian Buchner, Karl-Georg Warnick, Thorsten Wölfle, Andreas Görling, Hans-Peter Steinrück, Wolfgang Hieringer, Hubertus Marbach. Chemical Fingerprints of Large Organic Molecules in Scanning Tunneling Microscopy: Imaging Adsorbate-Substrate Coupling of Metalloporphyrins. *J. Phys. Chem. C*, 113:16450, 2009.

[76] Knud Seufert, Willi Auwärter, and Johannes V. Barth. Discriminative Response of Surface-Confined Metalloporphyrin Molecules to Carbon and Nitrogen Monoxide. *Journal of the American Chemical Society*, 132(51):18141–18146, 2010.

[77] Stefanie Ditze, Michael Röckert, Florian Buchner, Elisabeth Zillner, Michael Stark, Hans-Peter Steinrück, and Hubertus Marbach. Towards the engineering of molecular nanostructures: local anchoring and functionalization of porphyrins on model-templates. *Nanotechnology*, 24(11):115305, 2013.

[78] Rubénl González-Moreno, Carlos Sánchez-Sánchez, Marta Trelka, Roberto Otero, Albano Cossaro, Alberto Verdini, Luca Floreano, Marta Ruiz-Bermejo, Aran García-Lekue,

Joseí Angel Martín-Gago, and Celia Rogero. Following the Metalation Process of Protoporphyrin IX with Metal Substrate Atoms at Room Temperature. *The Journal of Physical Chemistry C*, 115(14):6849–6854, 2011.

[79] K. Diller, F. Klappenberger, M. Marschall, K. Hermann, A. Nefedov, Ch. Wöll, J. V. Barth. Self-metalation of 2H-tetraphenylporphyrin on Cu(111): An x-ray spectroscopy study. *J. Chem. Phys.*, 136:014705, 2012.

[80] Jan Nowakowski, Christian Wackerlin, Jan Girovsky, Dorota Siewert, Thomas A. Jung, and Nirmalya Ballav. Porphyrin metalation providing an example of a redox reaction facilitated by a surface reconstruction. *Chem. Commun.*, 49:2347–2349, 2013.

[81] K. Diller, F. Klappenberger, F. Allegretti, A. C. Papageorgiou, S. Fischer, A. Wiengarten, S. Joshi, K. Seufert, D. Ecija, W. Auwärter, and J. V. Barth. Investigating the molecule-substrate interaction of prototypic tetrapyrrole compounds: Adsorption and self-metalation of porphine on Cu(111). *The Journal of Chemical Physics*, 138(15):–, 2013.

[82] Andrea Goldoni, Carlo A. Pignedoli, Giovanni Di Santo, Carla Castellarin-Cudia, Elena Magnano, Federica Bondino, Alberto Verdini, and Daniele Passerone. Room Temperature Metalation of 2H-TPP Monolayer on Iron and Nickel Surfaces by Picking up Substrate Metal Atoms. *ACS Nano*, 6(12):10800–10807, 2012.

[83] Felix Bischoff, Knud Seufert, Willi Auwärter, Sushobhan Joshi, Saranyan Vijayaraghavan, David Ecija, Katharina Diller, Anthoula C. Papageorgiou, Sybille Fischer, Francesco Allegretti, David A. Duncan, Florian Klappenberger, Florian Blobner, Runyuan Han, and Johannes V. Barth. How Surface Bonding and Repulsive Interactions Cause Phase Transformations: Ordering of a Prototype Macrocyclic Compound on Ag(111). *ACS Nano*, 7(4):3139–3149, 2013.

[84] Knud Johannes Seufert. *Surface anchored porphyrins - investigations of assembly, reactivity, manipulation and in-situ synthesis*. PhD thesis, Technische Universität München, 2012.

[85] Giovanni Di Santo, Stephan Blankenburg, Carla Castellarin-Cudia, Mattia Fanetti, Patrizia Borghetti, Luigi Sangaletti, Luca Floreano, Alberto Verdini, Elena Magnano, Federica Bondino, Carlo A. Pignedoli, Manh-Thuong Nguyen, Roberto Gaspari, Daniele Passerone, Andrea Goldoni. Supramolecular Engineering through Temperature-Induced Chemical Modification of 2H-Tetraphenylporphyrin on AgACHTUNGTRENUNG(111): Flat Phenyl Conformation and Possible Dehydrogenation Reactions. *Chem. Eur. J.*, 17:14354, 2011.

[86] Florian Buchner, Ina Kellner, Wolfgang Hieringer, Andreas Gorling, Hans-Peter Steinruck, and Hubertus Marbach. Ordering aspects and intramolecular conformation of tetraphenylporphyrins on Ag(111). *Phys. Chem. Chem. Phys.*, 12:13082–13090, 2010.

[87] Knud Seufert, Marie-Laure Bocquet, Willi Auwärter, Alexander Weber-Bargioni, Joachim Reichert, Nicolas Lorente, Johannes V. Barth. Cis-dicarbonyl binding at cobalt and iron porphyrins with saddle-shape conformation. *Nature chemistry*, 3:114, 2011.

[88] Willi Auwärter, Knud Seufert, Felix Bischoff, David Ecija, Saranyan Vijayaraghavan, Sushobhan Joshi, Florian Klappenberger, Niveditha Samudrala and Johannes V. Barth. A surface-anchored molecular four-level conductance switch based on single proton transfer. *Nature nanotechnology*, 7:41, 2011.

[89] Giovanni Di Santo, Stephan Blankenburg, Carla Castellarin-Cudia, Mattia Fanetti, Patrizia Borghetti, Luigi Sangaletti, Luca Floreano, Alberto Verdini, Elena Magnano, Federica Bondino, Carlo A. Pignedoli, Manh-Thuong Nguyen, Roberto Gaspari, Daniele Passerone, and Andrea Goldoni. Supramolecular Engineering through Temperature-Induced Chemical Modification of 2H-Tetraphenylporphyrin on AgACHTUNGTRENUNG(111): Flat Phenyl Conformation and Possible Dehydrogenation Reactions. *Chem. Eur. J.*, 17:14354, 2011.

[90] F. Klappenberger, A. Weber-Bargioni, W. Auwärter, M. Marschall, A. Schiffrin, and J. V. Barth. Temperature dependence of conformation, chemical state, and metal-directed assembly of tetrapyridyl-porphyrin on Cu(111). *The Journal of Chemical Physics*, 129(21):–, 2008.

[91] Geoffrey Rojas, Xumin Chen, Donna Kunkel, Matthias Bode, Axel Enders. Temperature Dependence of Metal-Organic Heteroepitaxy. *Langmuir*, 27:17267, 2011.

[92] Yi-Qi Zhang, Nenad Kepčija, Martin Kleinschrodt, Katharina Diller, Sybille Fischer, Anthoula C Papageorgiou, Francesco Allegretti, Jonas Björk, Svetlana Klyatskaya, Florian Klappenberger, Mario Ruben, and Johannes V Barth. Homo-coupling of terminal alkynes on a noble metal surface. *Nat. Commun.*, 3:1286–1293, January 2012.

[93] Xuemei Zhang, Qingdao Zeng, and Chen Wang. On-surface single molecule synthesis chemistry: a promising bottom-up approach towards functional surfaces. *Nanoscale*, 5:8269–8287, 2013.

[94] Yue Bing Zheng, Brian Kiraly, Sarawut Cheunkar, Tony Jun Huang, and Paul S. Weiss. Incident-Angle-Modulated Molecular Plasmonic Switches: A Case of Weak Exciton-plasmon Coupling. *Nano Letters*, 11(5):2061–2065, 2011.

[95] Theobald, James A. Oxtoby, Neil S. Phillips, Michael A. Champness, Neil R. Beton, Peter H. Controlling molecular deposition and layer structure with supramolecular surface assemblies. *Nature*, 424:6952, 2003.

[96] Johannes V. Barth, Jens Weckesser, Chengzhi Cai, Peter Günter, Lukas Bürgi, Olivier Jeandupeux, and Klaus Kern. Building Supramolecular Nanostructures at Surfaces by Hydrogen Bonding. *Angewandte Chemie International Edition*, 39(7):1230–1234, 2000.

[97] Meike Shör, Markus Wahl, Christian H. Galka, Till Riehm, Thomas A. Jung, and Lutz H. Gade. Controlling Molecular Assembly in Two Dimensions: The Concentration Dependence of Thermally Induced 2D Aggregation of Molecules on a Metal Surface. *Angewandte Chemie*, 117(45):7560–7564, 2005.

[98] Johannes V Barth, Jens Weckesser, Giancarlo Trimarchi, Masha Vladimirova, Alessandro De Vita, Chengzhi Cai, Harald Brune, Peter Günter, and Klaus Kern. Stereochemical effects in supramolecular self-assembly at surfaces: 1-D versus 2-D enantiomorphic ordering for PVBA and PEBA on Ag(111). *J. Am. Chem. Soc.*, 124(27):7991–8000, July 2002.

[99] D. L. Keeling, N. S. Oxtoby, C. Wilson, M. J. Humphry, N. R. Champness, and P. H. Beton. Assembly and Processing of Hydrogen Bond Induced Supramolecular Nanostructures. *Nano Letters*, 3(1):9–12, 2003.

[100] Richard van Hameren, Peter Schön, Arend M. van Buul, Johan Hoogboom, Sergiy V. Lazarenko, Jan W. Gerritsen, Hans Engelkamp, Peter C. M. Christianen, Hans A. Heus, Jan C. Maan, Theo Rasing, Sylvia Speller, Alan E. Rowan, Johannes A. A. W. Elemans, and Roeland J. M. Nolte. Macroscopic Hierarchical Surface Patterning of Porphyrin Trimers via Self-Assembly and Dewetting. *Science*, 314(5804):1433–1436, 2006.

[101] Nian Lin, Alexandre Dmitriev, Jens Weckesser, Johannes V. Barth, and Klaus Kern. Real-Time Single-molecule Imaging of the formation and dynamics of coordination compounds. *Angew. Chem. Int. Ed.*, 2002.

[102] K. Morgenstern, E. Laegsgaard, I. Stensgaard, F. Besenbacher, M. Böhringer, W.-D. Schneider, R. Berndt, F. Mauri, A. De Vita, and R. Car. Stability of two-dimensional nanostructures. *Applied Physics A*, 69(5):559–569, 1999.

[103] Steven De Feyter, Andre Gesquiere, Mohamed M. Abdel-Mottaleb, Petrus C. M. Grim, Frans C. De Schryver, Christian Meiners, Michel Sieffert, Suresh Valiyaveettil, and Klaus Müllen. Scanning Tunneling Microscopy: A Unique Tool in the Study of Chirality, Dynamics, and Reactivity in Physisorbed Organic Monolayers. *Accounts of Chemical Research*, 33(8):520–531, 2000. PMID: 10955982.

[104] T. Yokoyama, S. Yokoyama, T. Kamikado, Y. Okuno, S. Mashiko. Selective assembly on a surface of supramolecular aggregates with controlled size and shape. *Nature*, 413:619, 2001.

[105] B. Grzybowski G.M. Whitesides. Self-assembly at all scales. *Science*, 295:2418, 2002.

[106] L. Grill, M. Dyer, L. Lafferentz, M. Persson, M.V. Peters. Nano-architectures by covalent assembly of molecular building blocks. *Nature*, 2:687, 2007.

[107] Catherine M. Doyle, Sergey A. Krasnikov, Natalia N. Sergeeva, Alexei B. Preobrajenski, Nikolay A. Vinogradov, Yulia N. Sergeeva, Mathias O. Senge, and Attilio A. Cafolla. Evidence for the formation of an intermediate complex in the direct metalation of tetra(4-bromophenyl)-porphyrin on the Cu(111) surface. *Chem. Commun.*, 47:12134–12136, 2011.

[108] Matthew O. Blunt, James C. Russell, Neil R. Champness, and Peter H. Beton. Templating molecular adsorption using a covalent organic framework. *Chem. Commun.*, 46:7157–7159, 2010.

[109] Rico Gutzler, Hermann Walch, Georg Eder, Stephan Kloft, Wolfgang M. Heckl, and Markus Lackinger. Surface mediated synthesis of 2D covalent organic frameworks: 1,3,5-tris(4-bromophenyl)benzene on graphite(001), Cu(111), and Ag(110). *Chem. Commun.*, pages 4456–4458, 2009.

[110] Nikolas A. A. Zwaneveld, Remy Pawlak, Mathieu Abel, Daniel Catalin, Didier Gigmes, Denis Bertin, and Louis Porte. Organized Formation of 2D Extended Covalent Organic Frameworks at Surfaces. *Journal of the American Chemical Society*, 130(21):6678–6679, 2008. PMID: 18444643.

[111] Roland Coratger, Bastien Calmettes, Mathieu Abel, and Louis Porte. {STM} observations of the first polymerization steps between hexahydroxy-tri-phenylene and benzene-diboronic acid molecules . *Surface Science*, 605(7):831 – 837, 2011.

[112] Oualid Ourdjini, Rémy Pawlak, Mathieu Abel, Sylvain Clair, Liang Chen, Nathalie Bergeon, Michel Sassi, Vincent Oison, Jean-Marc Debierre, Roland Coratger, and Louis Porte. Substrate-mediated ordering and defect analysis of a surface covalent organic framework. *Phys. Rev. B*, 84:125421, Sep 2011.

[113] Matthias Treier, Roman Fasel, Neil R. Champness, Stephen Argent, and Neville V. Richardson. Molecular imaging of polyimide formation. *Phys. Chem. Chem. Phys.*, 11:1209–1214, 2009.

[114] Matthias Treier, Neville V. Richardson, and Roman Fasel. Fabrication of Surface-Supported Low-Dimensional Polyimide Networks. *Journal of the American Chemical Society*, 130(43):14054–14055, 2008. PMID: 18826313.

[115] Diaz Arado, Oscar and Mönig, Harry and Wagner, Hendrik and Franke, Jörn-Holger and Langewisch, Gernot and Held, Philipp Alexander and Studer, Armido and Fuchs, Harald. On-Surface Azide-Alkyne Cycloaddition on Au(111). *ACS Nano*, 7(10):8509–8515, 2013.

[116] Fabian Bebensee, Christian Bombis, Sundar-Raja Vadapoo, Jacob R. Cramer, Flemming Besenbacher, Kurt V. Gothelf, and Trolle R. Linderoth. On-Surface Azide-Alkyne Cycloaddition on Cu(111): Does It "Click" in Ultrahigh Vacuum? *Journal of the American Chemical Society*, 135(6):2136–2139, 2013.

[117] Gregory Franc and Andre Gourdon. Covalent networks through on-surface chemistry in ultra-high vacuum: state-of-the-art and recent developments. *Phys. Chem. Chem. Phys.*, 13:14283–14292, 2011.

[118] Jonas Björk and Felix Hanke. Towards Design Rules for Covalent Nanostructures on Metal Surfaces. *Chemistry A European Journal*, 20(4):928–934, 2014.

[119] Abraham Nitzan and Mark A. Ratner. Electron transport in molecular wire junctions. *Science*, 300(5624):1384–1389, May 2003.

[120] K. S. Novoselov. Nobel Lecture: Graphene: Materials in the Flatland. *Rev. Mod. Phys.*, 83:837–849, Aug 2011.

[121] Andre K. Geim. Nobel Lecture: Random walk to graphene. *Rev. Mod. Phys.*, 83:851–862, Aug 2011.

[122] Dmitrii F. Perepichka and Federico Rosei. Extending Polymer Conjugation into the Second Dimension. *Science*, 323(5911):216–217, 2009.

[123] M. Hasegawa and K. Horie. Photophysics, photochemistry, and optical properties of polyimides . *Progress in Polymer Science*, 26(2):259 – 335, 2001.

[124] Jia Guo, Yanhong Xu, Shangbin Jin, Long Chen, Toshihiko Kaji, Yoshihito Honsho, Matthew A. Addicoat, Jangbae Kim, Akinori Saeki, Hyotcherl Ihee, Shu Seki, Stephan Irle, Masahiro Hiramoto, Jia Gao, Donglin Jiang. Conjugated organic framework with three-dimensionally ordered stable structure and delocalized π clouds. *Nature Communication*, 4, 2013.

[125] Jie Hu, Dong Zhang, and Frank W. Harris. Ruthenium(III) Chloride Catalyzed Oxidation of Pyrene and 2,7-Disubstitued Pyrenes: An Efficient, One-Step Synthesis of Pyrene-4,5-diones and Pyrene-4,5,9,10-tetraones. *The Journal of Organic Chemistry*, 70(2):707–708, 2005. PMID: 15651825.

[126] Niksa Kulisic, Sandeep More, and Aurelio Mateo-Alonso. A tetraalkylated pyrene building block for the synthesis of pyrene-fused azaacenes with enhanced solubility. *Chem. Commun.*, 47:514–516, 2011.

[127] M. Froimowitz. HyperChem: a software package for computational chemistry and molecular modeling. *BioTechniques*, 14(6):1010–1013, June 1993.

[128] A. Hauschild, K. Karki, B. C. C. Cowie, M. Rohlfing, F. S. Tautz, and M. Sokolowski. Molecular Distortions and Chemical Bonding of a Large π-Conjugated Molecule on a Metal Surface. *Phys. Rev. Lett.*, 94:036106, Jan 2005.

[129] M. Eremtchenko, J. A. Schaefer and F. S. Tautz. Understanding and tuning the epitaxy of large aromatic adsorbates by molecular design. *Nature*, 425:602, 2003.